Development and Application of Polarization Sensitive Optical Coherence Tomography

Peijun Tang

A dissertation
submitted in partial fulfillment of the
requirements for the degree of

Doctor of Philosophy

University of Washington

2021

Reading Committee:

Ruikang K. Wang

Ivan M. Pelivanov

Andy Shih

Program Authorized to Offer Degree:

Department of Bioengineering

University of Washington

Abstract

Development and Application of Polarization Sensitive Optical Coherence Tomography

Peijun Tang

Chair of the Supervisory Committee:
Ruikang K. Wang
Department of Bioengineering

Optical coherence tomography (OCT), a three-dimensional optical imaging technique based on low coherence interferometry, can be extended to measure the functional property of the biological sample. As a functional extension of OCT, polarization sensitive optical coherence tomography (PSOCT) enables 3D imaging of the anisotropic biological samples, such as scar, tendon, muscle, collagen, and nerve fiber bundles. This thesis focuses on the development and application of PSOCT. This goal includes four specific aims. The first aim is to develop a single input PSOCT imaging system with an improved image contrast. To achieve this aim, the polarization state is utilized as the imaging parameter and visualized using the Stokes parameters-based color-encoded algorithm. The second aim is to develop an algorithm that can derive depth-resolved polarization parameters with the single input PSOCT system. Towards this aim, a PSOCT-based polarization state transmission model is proposed. Based on this model, a novel method that utilizes discrete differential geometry (DDG) combined with a series of 3D rotations is developed to derive the local axis orientation and phase retardation. The third aim is to use the developed DDG-based PST method to extract the collagen organization embedded within the soft biological tissues. To achieve this aim, the proposed method is utilized to image the local axis orientation of the collagen fibers of the rodent heart and human facial skin. The fourth aim is to use the multiparameter provided by the PSOCT to detect and characterize the white spot lesions in the enamel of the tooth. Towards this aim, multiple parameters in the PSOCT: scattering, attenuation, degree of polarization (DOP), local axis orientation and local phase retardation of the sample are provided simultaneously for the comprehensive investigation of the location, depth, and severity of the white spot lesions.

TABLE OF CONTENTS

LIST OF FIGURES

ACKNOWLEDGEMENTS

Foremost, I would like to express my sincere gratitude to my advisor Prof. Ruikang Wang for the continuous support of my Ph.D. study and research, for his foresight, motivation, enthusiasm and immense knowledge. His guidance helped me in all the time of research and writing of this thesis. This work would not have been done without his tremendous support and guidance. Thank you for giving me this fantastic opportunity to learn about and investigate the OCT techniques. Thank you for trusting my potentials, guiding me with directions, and training me to be a scholar. Thank you for providing me with the best resources to explore and develop my research. Thank you for your patience and professional skill to revise my paper. I could not have imagined having a better advisor and mentor for my study. It's a great honor to be a member of this lab!

I would like to thank my Ph.D. dissertation committee members, Prof. Ivan Pelivanov, Prof. Andy Shih, who have spent their valuable time to review my work and give me suggestions, and Prof. Dan Fu (Graduate School Representative), for making room in his busy schedule to attend my final defense.

My sincere thanks also go to Prof. Ying Zheng and Prof. Nina Lu, for helping me to finish my project and revise my paper.

I would also like to give special thanks to all lab members in the Biophotonics and Imaging Laboratory (BAIL). Special thanks to Dr. Yuandong Li (Jenny), who has mentored and taught me rodent surgeries in my early research; Dr. Shaozhen Song, Nhan Le, Jingjiang Xu and Wei wei who gave me a lot of technical supports; Dr. Mitchell Kirby helping me to revise the paperwork. Great thanks to Dr. Qingqing Zhang and who gave me helpful and useful suggestions during the research. I would also like to thank Dr. Hao Zhou, Dr. Zhongdi Chu, Dr. Yiming Lu, Dr. Jie Lu. Dr. Qinghua He, Dr. Yuxuan Cheng, Dr. Teng Liu and Xiao Zhou, who have provided me with friendship and encouragement.

I am extremely grateful to my parents, Dr. Zhilie Tang and Ms. Hong Sun, and my grandparents for their endless love, prayers, caring and support. They give me encouragement to overcome difficulties. My pets, two lovely hamsters, who accompanied me during this journey hav given me a lot of fun.

Chapter 1. INTRODUCTION

1.1 SIGNIFICANCE AND RESEARCH MOTIVATION

Functional imaging has been gaining attention in areas ranging from basic research to clinical applications because it enables the measurement and visualization of the physiological activities besides the anatomical structure of the biological sample, bringing insights into how living things work. Optical anisotropy, which is ubiquitous in biological structures, is a unique property of the tissues that is related to specific mechanical properties (e.g., skin stiffness and elasticity) and physiological functions (e.g., cancer fibrosis and wound healing) [1-5]. Because the optical anisotropy can cause changes in the polarization state of the light, polarization-related imaging techniques are utilized to measure and characterize the optical anisotropic property of the sample. Many polarization-based optical anisotropy imaging techniques have been developed, such as fluorescence polarization microscopy (FPM) [6, 7], co- and cross-polarized-based imaging [5, 8], Mueller matrix imaging [9, 10], and polarization Raman spectroscopy [4, 11]. However, these polarization-based imaging techniques can only provide two-dimensional images. Hence, destructive procedures are required to section the samples for the investigation at the deep tissue level. To obtain the anisotropic information embedded within the tissues non-invasively, polarization imaging is integrated into three-dimensional (3D) optical imaging techniques such as second harmonic generation microscopy (SHG) [12, 13] and confocal microscopy [14] but the imaging depth of these imaging techniques is limited to only a few hundred microns.

Optical coherence tomography (OCT) is an optical imaging modality that can generate cross-sectional images of biological tissues *in vivo*, enabling the visualization of 3D microanatomical information with a wide field of view (FOV) (from a few to tens of square centimeters), high resolution (1–20 um) and relatively deep imaging depth (up to ~2 mm) [15]. As a functional extension of OCT, polarization sensitive optical coherence tomography (PSOCT) is an ideal imaging tool to image the 3D optical anisotropic property of the biological sample at tissue level [16] in vivo.

Currently, PSOCT can be divided into two types: the bench top PSOCT and the fiber-based PSOCT. Bench top PSOCT is implemented in free space. Since the bulk air-spaced optical components permit precise control over the polarization state of light in the sample and reference arms, the system effect on the measurement of the output polarization state is relatively small. Hence, the bench top PSOCT utilizes a single input polarization state to derive the depth-resolved birefringent information within the sample by ignoring the system effect. This type of system guarantees simple system setup but cannot provide the system correction to improve the imaging quality [17, 18]. Compared with the free-space setup, fiber-based PSOCT, the second type of PSOCT, offer distinct advantages in terms of system alignment and handling. However, because the optical fiber can introduce complex changes in the polarization state of the light, system correction is required to provide sufficient imaging quality. To correct the system effect, two or more input polarization states are needed to solve the unknown parameter induced by the system. With the system correction, the fiber-based PSOCT setups can provide high quality imaging performance but suffer from sophisticated setups, complex algorithms, and multiple measurements [19-22] due to the requirement of multiple input polarization states. The computation methods of these two types of PSOCT are based on Jones matrix calculus, which currently cannot provide the depth-resolved birefringent information of the sample using a single input polarization state when consider the sample effect.

In this work, I developed novel methods based on the Stokes parameters calculus rather than Jones matrix calculus to implement the depth-resolved PSOCT measurement using a single input polarization state. Based on this method, the system effect can be considered and corrected without the complicated system setup. That is, the system setup can not only retain the neatness of the imaging system but also provide a sufficient performance for the anisotropic imaging of the biological samples. The benefits of the methods based on the Stokes-parameters calculus are depicted in Figure 1.1. Herein, I will introduce the novel methods and demonstrate their applications on the biological tissues.

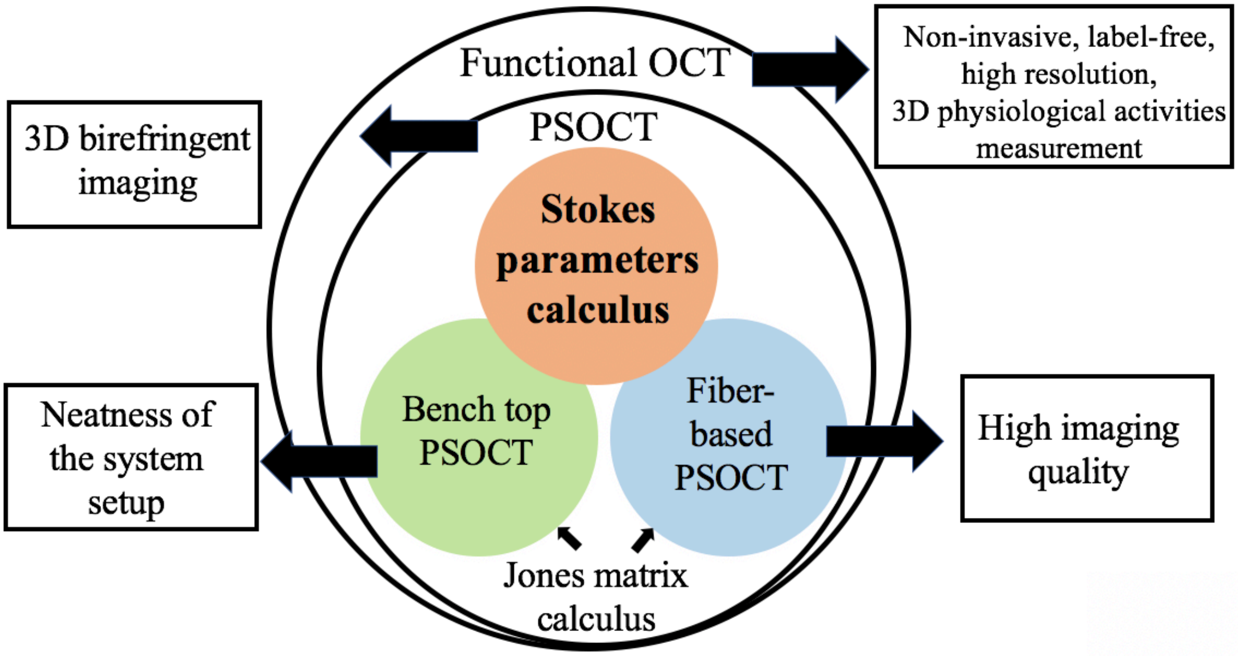

Figure 1.1. Advantage of using Stokes parameters-based calculus in PSOCT. PSOCT that utilized stokes parameters-based calculus can retain the neatness of the system setup by using a single input polarization state and can provide sufficient imaging quality.

1.2 TECHNICAL BACKGROUND: OPTICAL COHERENCE TOMOGRAPHY

1.2.1 Principle of OCT

OCT is being rapidly developed and gaining attention in areas ranging from basic research to clinical applications because it is an optical imaging modality that falls in the gap between traditional microscopy and other tissue-level imaging techniques [15]. The principle of OCT is based on the low coherence interferometry which is implemented by a broadband light source and an optical interferometry. That is, the depth resolving ability of OCT comes from the optical coherence gating mechanism of the optical low coherence interferometry. In summary, OCT is a technique based on Michelson interferometer or its variants, which analyzes the interference signals between a split and later re-combined broadband optical field. There are two main types of OCT that have been developed, including time domain and Fourier domain OCT.

Time domain (TD) OCT is the early type of OCT [15, 23], which is implemented by an axially scanning mirror in the reference arm and detects all wavelengths simultaneously in a single photodetector. This system setup utilizes the property of low coherence interferometry: interference fringes are only observed when the optic path length difference is within the coherence length of the light source. The optical setup for a TD-OCT system consists of a low coherence source and a Michelson interferometer as illustrated in Fig. 1.2.

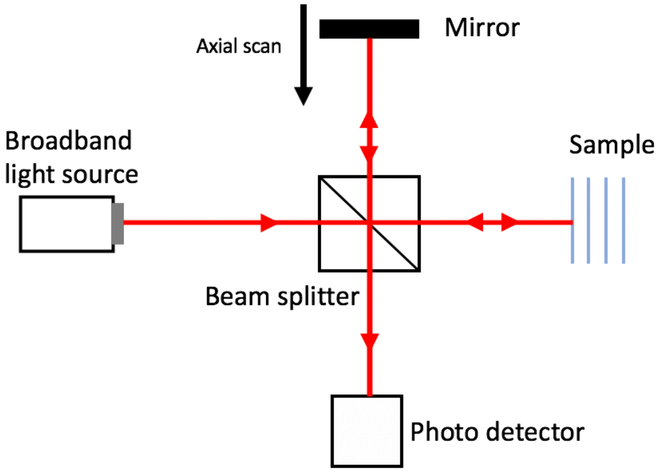

Figure 1.2. Schematic diagram of the time domain optical coherence tomography.

The light sent from a broadband light source passes through a beam splitter and is split into two beams, where one travels in a reference path to a reference mirror, and the other goes into the biological samples. The backscattered signals from the reference mirror and the sample are recombined and detected by a single photodetector, generating interference signals. The interference of the two light beams can be expressed as

$$I_D = [R_s + R_r] + S(\Delta z)[2\sqrt{R_s R_r}\cos(2\Delta z k_0) \quad (1.1)$$

where I_D is the power received at the detector; R_s and R_r are the power of the light scattered back from the sample and reference arm respectively; $S(\Delta z)$ is the envelope function of the coherent light source; Δz is the optical path length difference between reference and sample arm; k_0 is the wavenumber of the center frequency of the broadband light source. When a low coherent light source (i.e., the broadband light source) is used, the interference fringes can be observed only when the reference and sample optical path lengths were matched to within the coherence length of the light source. Hence, by scanning the reference mirror, depth-resolved tissue reflectivity can be reconstructed from the interference pattern, which is recorded as a one-dimensional intensity profile along the axial direction (A-line). The coherence length, $l_c = \frac{2ln2\lambda^2}{\pi\Delta\lambda}$, which is inversely proportional to the bandwidth of the light source, determines the axial resolution. However, the mechanical scanning of the reference mirror limits the scanning rate of the TD-OCT, which is achieved at a maximum of ~8 kHz per A-line (one depth scan).

1.2.2 Fourier-domain OCT

A new type of OCT: Fourier domain or spectral domain OCT (SD-OCT) [15, 24] has been developed. This kind of OCT system has attracted a huge increase in attention because it has the advantage that no moving parts are required to obtain axial scans, which is a significant benefit for actual biomedical applications. The reference path length is fixed during imaging and the detection signals are replace with the broadband interference spectra, which are detected by using a spectrometer, or by sweeping light frequency of a swept source while detecting interference using a single detector. The spectral interferogram can be represented as

$$I(k) = [R_s + R_r] + S(k)[2\sqrt{R_s R_r}\cos(2k\Delta z) \tag{1.2}$$

where S(k) is the power spectrum of the light source, k is the wavenumber. This equation shows that the period of the spectral oscillation of the acquired signal in k space is proportional to the path length difference Δz. The shorter path length difference produces spectral oscillation with a lower frequency and vice versa. Hence, a Fourier transform of the spectral fringes will result in a depth profile. Since frequency information from all depths of one A-line in tissue is acquired in parallel from the captured spectra, the imaging speed of the Fourier domain OCT can be improved dramatically, to between 25,000–50,000 A-scans/s [25]. Moreover, a higher signal-to-noise ratio (SNR) is achieved because spectrally dispersing each wavelength to a separate detector eliminates the cross shot-noise term in the Fourier-domain OCT systems.

Spectral domain OCT (SDOCT)

The Fourier domain OCT can be implemented by two different configurations. The first one is the spectral domain (SD) OCT that utilizes a broadband light source and a spectrometer as shown in Fig. 1.3. Based on Eq. 1.2, the information of the full depth scan can be obtained within a single exposure. However, using a spectrometer to detect the interference signals can generate several issues: 1) Due to the finite resolution of the spectrometer, SD-OCT suffers from a depth-dependent sensitivity decay: signals from the deeper layer decrease quickly and the corresponding image quality will be degraded. This property of SD-OCT limits its application when imaging tissues at a deeper depth. 2) The setup and the calibration process of the spectrometer are relatively complicated. When two or more channel measurements are required (e.g., PSOCT), the system arrangement would be redundant and expensive.

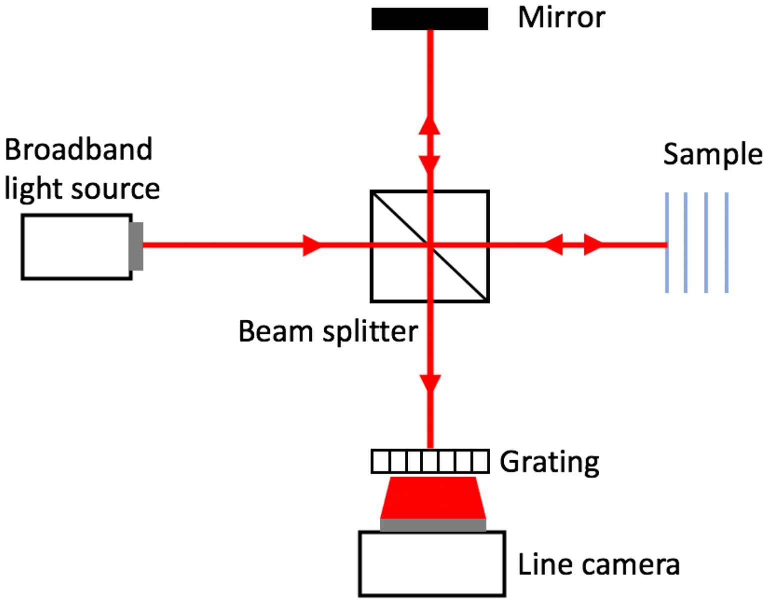

Figure 1.3. Schematic diagram of the spectral domain optical coherence tomography (SD-OCT).

Swept source OCT (SS-OCT)

Swept source OCT (SS-OCT) is the second type of Fourier domain OCT, where the hardware differs from SD-OCT in several ways, including the light source, bulk optics components, and photodetection device as shown in Fig. 1.4. A tunable swept laser is utilized as the light source of the SS-OCT, which emits a wavelength with a very narrow bandwidth at any instant in time and sweeps across a broad range of the wavelengths as a function of time. Since the linewidth of each wavelength is much narrower than that captured by the spectrometer, the sensitivity roll-off performance using the SS-OCT is significantly improved over the SD-OCT. Moreover, because there is no need to use the spectrometer to divide the wavelength of the light source, a single photodetector can be used to detect the spectral interferogram in the SS-OCT system, much simplifying the system setup. The imaging speed of the swept-source OCT is between 50,000–400,000 A-scans/s, even faster than the SDOCT system. Because PSOCT requires two detection modules, the configuration based on the SS-OCT is the ideal scheme for the implementation of the PSOCT measurement.

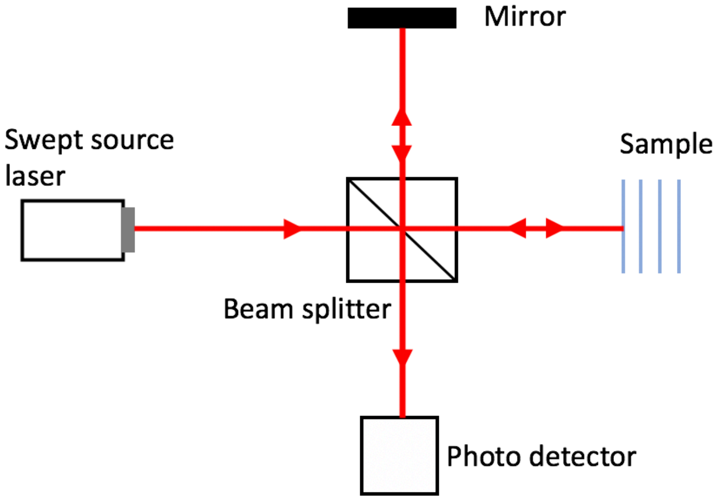

Figure 1.4. Schematic diagram of the swept source optical coherence tomography (SS-OCT).

1.3 FUNCTIONAL EXTENSIONS OF OCT

Several functional extensions have been applied to enable the acquisition of additional physiological information from OCT. Phase-sensitive OCT [26-28], which is highly sensitive to small motion and vibration (smaller than 1 nm), is utilized to measure the cellular motion within the organ of Corti [27], the neural activity in the nerve preparations [29-31] and the tissue dynamic of the barrel cortex during whisker stimulation [32]. Spectroscopic OCT [33] is used to measure wavelength-dependent absorption of light in biological tissue, which is related to functional information of the tissue, such as blood oxygen saturation [34] and lipid in atherosclerotic plaques [35]. Optical coherence elastography (OCE) [36, 37] adds an externally induced mechanical stimulus alongside OCT to obtain the mechanical properties of the tissue. The change in the elastic properties of the tissue is related to some pathological conditions, such as edema, fibrosis, calcification, and tumors. Optical coherence angiography (OCTA) [38-40] and optical doppler tomography (ODT) [41, 42] utilize the phase shift induced by the red blood cells to map and extract 3D vascular information in the mouse brain, human eye, and skin. By separating the moving and static scattering elements within the tissue, high-resolution images of blood flow can be obtained by this technique. OCT-based angiography enables studies of a tumor microvasculature [43, 44] and neurovascular research [45, 46].

Polarization sensitive optical coherence tomography (PSOCT), another emerging functional extension of OCT, enables the cross-sectional imaging of the anisotropic (birefringent) biological samples, such as tendon, muscle, collagen, enamel of teeth, and nerve fiber bundles [16]. PSOCT has been used to study collagen orientation in artificial cartilage [47], collagen content in the aortic plaques [48], and birefringent properties in the burned skin [49]. Since PSOCT is the emerging technique that leaves many search and application spaces to be investigated, I will focus on PSOCT in the following section. Taking advantage of the high resolution, wide FOV, fast imaging speed and relatively deep imaging depth (up to ~2 mm) in tissue compared with the second harmonic generation microscopy techniques (up to ~200 µm), functional extensions of OCT would have useful and practical applications in the studies of the biological tissues both pre-clinically and clinically.

1.4 POLARIZATION SENSITIVE OPTICAL COHERENCE TOMOGRAPHY (PSOCT)

PSOCT is an emerging functional extension of OCT that can measure the polarization-affecting properties of the biological sample by introducing special optical elements to detect the change of the polarization state of the incident light. Hence, not only structure signals, but also the polarization-related parameters: birefringence, diattenuation and optic axis orientation information of the sample can be obtained simultaneously in PSOCT [38].

Based on the polarization detection scheme, PSOCT is particularly useful in biological tissues with highly optical anisotropy (i.e., birefringence), such as highly organized fibrous architecture. When the incident light passes through such a sample with optical anisotropy, the light can be split into two orthogonal polarization states with different propagation velocities. When the light comes out from this sample, these two orthogonal polarization states are recombined together and form a new polarization state. This output polarization hence carries the optical anisotropic information of the sample. To detect such output polarization state, PSOCT is equipped with a PS detection scheme that splits the probing light into two orthogonal polarization components and measures their intensities and the phase difference between them. Based on these three parameters, polarization-related parameters: birefringence, optic axis orientation degree of polarization uniformity, and diattenuation of the sample can be derived. This is the basic concept of the PSOCT system.

Computation methods of polarization-related parameters can be divided into two broad categories based on formalism used to describe the polarization states of the light and the sample: Jones formalism and the Stokes formalism based on the Poincare sphere.

1.4.1 Jones calculus in PSOCT

In the PSOCT detection, Jones calculus is first utilized to compute the phase retardation and axis orientation in the sample. First, we introduce the Jones matrix formalism of the polarization state of light, the sample and the optical elements in the system.

In the Jones calculus, the polarization state of light can be described as the Jones vector:

$$\vec{E} = \begin{bmatrix} E_H e^{i\phi_x} \\ E_V e^{i\phi_y} \end{bmatrix}, \tag{1.3}$$

where E_x and E_y represent the amplitudes of the horizontal and vertical components of the light respectively, ϕ_x and ϕ_y represent the phases of the horizontal and vertical components of the light respectively. Due to the round-trip nature of OCT, the sample can be modeled as a series of linear retarders, which can be described by a 2 X 2 Jones matrix:

$$\boldsymbol{J_L}(\delta, \theta) = \boldsymbol{R}(-\theta)\boldsymbol{P}(\delta)\boldsymbol{R}(\theta) = \begin{bmatrix} sin(\theta) & -sin(\theta) \\ sin(\theta) & cos(\theta) \end{bmatrix} \begin{bmatrix} e^{i\delta} & 0 \\ 0 & 1 \end{bmatrix} \begin{bmatrix} cos(\theta) & sin(\theta) \\ -sin(\theta) & cos(\theta) \end{bmatrix}$$

$$= \begin{bmatrix} e^{i\delta} cos^2\theta + sin^2\theta & (e^{i\delta} - 1)\, sin(\theta)\, cos(\theta) \\ (e^{i\delta} - 1)\, sin(\theta)\, cos(\theta) & e^{i\delta} sin^2\theta + cos^2\theta \end{bmatrix} \tag{1.4}$$

where δ is the phase retardation of the retarder and θ is the orientation of the fast optic axis with respect to x-axis. The quarter-wave plate (QWP) used in the PSOCT system is linear, sharing the same Jones matrix formalism as Eq. 1.4.

When light passes through a train of linear retarders with Jones matrix $\boldsymbol{J_1}, \boldsymbol{J_2}, \ldots, \boldsymbol{J_n}$, the output polarization state of the light can be described as

$$\overrightarrow{E_{out}} = \boldsymbol{J_n} \cdots \boldsymbol{J_2}\boldsymbol{J_1}\overrightarrow{E_{in}}. \tag{1.5}$$

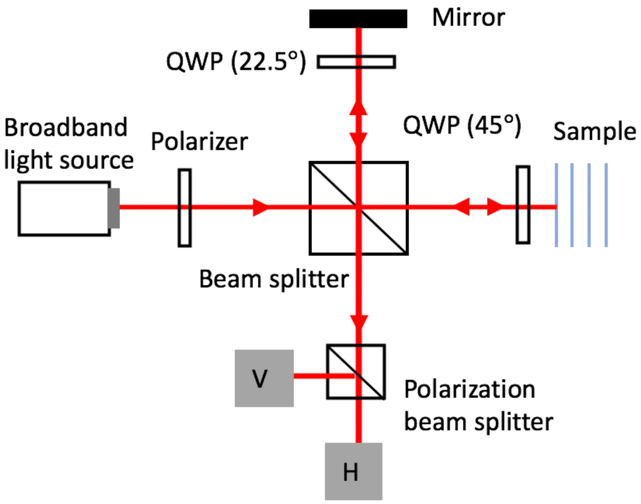

Figure 1.5. Schematic diagram of a generalized PSOCT system. QWP: quarter wave plate.

Based on these basic concepts of Jones matrix formalism, we next discuss how to use this formalism to derive the phase retardation and axis orientation in PSOCT. A generalized PSOCT imaging scheme (Fig. 1.5) is utilized to illustrate this computation. The output of the broadband light source is sent through a linear polarizer, becomes linearly polarized and is then split into two arms of the PSOCT system by a 50/50 beam splitter (BS).

Hence, the input optical fields of each arm are the same and can be expressed by Jones formulism as:

$$\overrightarrow{E_{rin}(k,z)} = \overrightarrow{E_{sin}(k,z)} = \frac{E(k)e^{ikz}}{\sqrt{2}}\begin{bmatrix}1\\0\end{bmatrix}, \tag{1.6}$$

where $E(k)e^{ikz}$ is the complex amplitude of the optical field of the output of the linear polarizer. The reference arm is installed with a QWP with the axis aligned at 22.5° with the input polarization state, ensuring that the reflected light couples equally in the vertical and horizontal channels. Hence, the optical field of the light reflected back from the reference arm can be expressed as

$$\overrightarrow{E_r(k,2z_r)} = \frac{\sqrt{R_r}}{\sqrt{2}}\boldsymbol{J}_{\boldsymbol{Q}}^{\boldsymbol{T}}\left(\frac{\pi}{2}, 22.5^\circ\right)\boldsymbol{J}_{\boldsymbol{Q}}\left(\frac{\pi}{2}, 22.5^\circ\right)\overrightarrow{E_{rin}(k,2z_r)}$$

$$= \frac{\sqrt{R_r}E(k)e^{i2kz}}{2}\left(\frac{-1}{\sqrt{2}}\right)\begin{bmatrix}1\\1\end{bmatrix} \tag{1.7}$$

where $\boldsymbol{J}_{\boldsymbol{Q}}$ is the Jones matrix of a QWP oriented at 22.5°.

The sample arm is equipped with a quarter-wave plate (QWP) aligned at 45° with the input polarization state which makes the linearly polarized light to become a circular polarized light before illuminating the sample. The Jones vector of the light reflected from the sample arm is:

$$\overrightarrow{E_s(k, z_s + z)} = \frac{\sqrt{R_s}}{\sqrt{2}} \boldsymbol{J}_{\boldsymbol{Q}}^{\boldsymbol{T}}\left(\frac{\pi}{2}, 45^\circ\right) \boldsymbol{J}_{\boldsymbol{s}}^{\boldsymbol{T}}(z) \boldsymbol{J}_{\boldsymbol{s}}(z) \boldsymbol{J}_{\boldsymbol{Q}}\left(\frac{\pi}{2}, 45^\circ\right) \overrightarrow{E_{s\imath n}(k, 2z_s)}$$

$$= \frac{\sqrt{R_s} E(k) e^{i2k(z_s+\bar{n}z)}}{2} \left(-e^{ikz\Delta n}\right) \begin{bmatrix} e^{i2\theta} sin\,(kz\Delta n) \\ cos\,(kz\Delta n) \end{bmatrix} \tag{1.8}$$

where $J_s(z)$ is the Jones matrix of the sample with a depth at z, $\bar{n} = (n_s + n_f)/2$ is the average refractive index along the fast n_f and slow n_s optic axes and $\Delta n = n_s - n_f$ represent the difference between them. The signals coming back from both reference and sample arms are recombined and sent to two polarization beam splitters (PBS1 and PBS2), respectively, where the interference light is split into horizontal and vertical components. Balanced detection with signal amplification is achieved for both vertical and horizontal channels by collecting the interference patterns returning from different light paths. The corresponding interference signals, recorded by the photodetectors, can be written as:

$$A_x(z) = \frac{S(k)}{2\sqrt{2}} \sqrt{R_r R_s} sin(kz\Delta n)\, cos\left[2k\left(z_R - (z_s + \bar{n}z)\right) - kz\Delta n - 2\theta\right].$$

$$A_y(z) = \frac{S(k)}{2\sqrt{2}} \sqrt{R_r R_s} cos(kz\Delta n)\, cos\left[2k\left(z_R - (z_s + \bar{n}z)\right) - kz\Delta n\right] \tag{1.9}$$

The phase retardation $\delta(z)$ and axis orientation θ can be obtained as []:

$$\delta(z) = kz\Delta n = tan^{-1}\left[\frac{A_x(z)}{A_y(z)}\right], \tag{1.10}$$

$$\theta = \frac{\Delta\phi}{2} = \frac{\angle A_x(z) - \angle A_y(z)}{2}. \tag{1.11}$$

1.4.2 Stokes calculus in PSOCT

Poincare sphere analysis

Another formalism called Stokes parameters can be used to represent the polarization state of the light. The change in the polarization state of the light induced by the optical elements can be described by the geometrical rotation in the Poincare sphere.

The Stokes parameters are a set of four intensity signals: I, Q, U and V that describe the polarization state of light. On a fixed basis defined by the two orthogonal polarized channels in the PSOCT system, the polarization state of the light can be expressed as

$$S = \begin{bmatrix} I \\ Q \\ U \\ V \end{bmatrix} = \begin{bmatrix} A_x^2 + A_y^2 \\ A_x^2 - A_y^2 \\ 2A_xA_y cos\,(\phi_x - \phi_y) \\ 2A_xA_y sin\,(\phi_x - \phi_y) \end{bmatrix} \tag{1.12}$$

where $A_{x,y}$ and $\phi_{x,y}$ are the amplitudes and phases of the optical field in the two orthogonal polarized channels.

Unlike the Jones vector which can only describe the light with a pure polarization state, Stokes parameters can also describe the partially polarized and unpolarized lights. Hence, in this formalism, the degree of polarization (DOP) of light beam can also be provided by the PSOCT as:

$$DOP = \frac{\sqrt{Q^2+U^2+V^2}}{I}. \tag{1.13}$$

DOP value ranges from 0 (completely unpolarized light) to 1 (pure polarized light). This parameter can be used to describe the depolarization of the light, which is related to many pathological activities, such as the carious in the enamel [50] and choroid melanin loss [51].

Another advantage of using Stokes parameters to describe the polarization state is that each polarization state can be visualized intuitively on the Poincare sphere in the 3D Stokes space, where the Q, U and V forms the Cartesian coordinates. The change in the polarization states induced by the birefringent sample can be visualized and represented as geometrical transformation. For example, the change in the polarization state of a light beam that passes through a birefringent sample can be modeled as a 3D rotation, where the rotation axis represents the optic axis, and the amount of rotation is the degree of phase retardation as shown in Fig. 1.6.

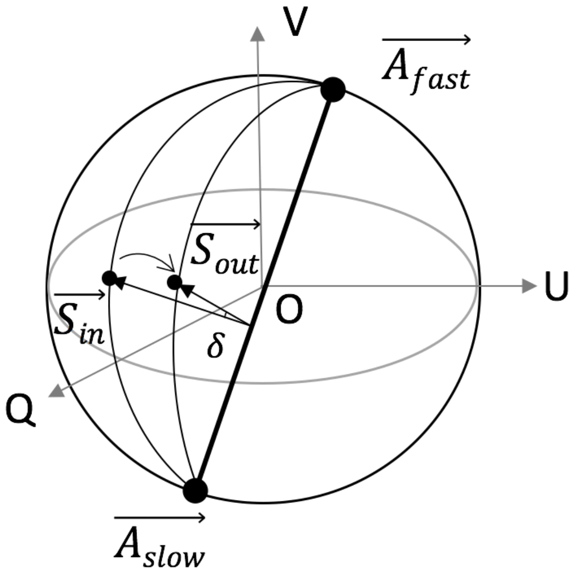

Figure 1.6. Schematic diagram of the effect of an elliptical retarder on elliptically polarized light.

By normalizing the Stokes parameters of the input/out polarization state into 1 (i.e., regardless of the depolarization effect), the amount of phase retardation and the optic axis orientation can be obtained using a geometrical analysis. Based on the model mentioned above, the optic axis is orthogonal to the vector difference between the input $\overrightarrow{S_{in}}$ and output polarization states $\overrightarrow{S_{out}}$: $\overrightarrow{S_{in}S_{out}}$. However, with only a pair of input and output polarization states, all the vectors within the plane that are orthogonal to the vector $\overrightarrow{S_{in}S_{out}}$ are the possible optic axes. By using two pairs of input/out polarization states, the exact optic axis A can be obtained as the line of the intersection of the two planes determined by each pair of input/output polarization state. The amount of rotation can be computed as:

$$\delta_p = cos^{-1}\left(\frac{[\overrightarrow{S_{in,p}}\times\vec{A}]\cdot[\overrightarrow{S_{out,p}}\times\vec{A}]}{|\overrightarrow{S_{in,p}}\times\vec{A}||\overrightarrow{S_{out,p}}\times\vec{A}|}\right) \tag{1.14}$$

The overall retardation δ can be obtained as the average of δ_1 and δ_2.

Except for the geometrical representation, the evolution of Stokes vectors can also be analyzed by the Mueller matrix. Changes in the polarization state induced by the birefringent sample can be described by a 4 X 4 Mueller matrix. Measurement of the full Mueller matrix of the sample using PSOCT has been discussed [52]. The Mueller matrix calculus is relatively complex and abstract, hence the interpretation of the results obtained from the Mueller matrix is still challenging.

Depth-resolved PSOCT

Due to the round-trip measurement of PSOCT, the phase retardation and axis orientation computed by the methods mentioned above are the cumulative results, leading to a difficulty to interpret the birefringent property of the sample at deeper layers. To interpret the local birefringent information correctly within the sample at depth, there is a need to develop further computations to derive the local (i.e., depth-resolved) phase retardation and local axis orientation of the sample. Currently, Jones matrix calculus is the major method to resolve the local birefringent information at each depth layer by layer from the surface.

For the PSOCT system with a single input polarization state, an algorithm based on Jones matrix calculus was developed to map local phase retardation and local axis orientation, where local axis orientation is considered as a scalar constrained within QU-plane [18]. This method successfully derived the local axis orientation and local phase retardation of the chicken muscle [17][18]. However, the asymmetry in the imaging system (i.e., the optical path in the system is not round-trip) can cause an overall rotation of the optic axes away from the QU-plane. That is, the local axis orientation to be measured becomes a 3D vector in Stokes space. As such, the algorithm would result in inaccurate determination of the local axis orientation and local phase retardation over depth.

By using two input polarization states, Makita et al [20] proposed an approach that can measure the generalized Jones matrix of the sample to obtain the local phase retardation. However, the local optical axis cannot be obtained by using this method. Martin Villiger et al [19, 53] proposed a method that can compute the local optic axis and the local phase retardation in the 3D Stokes space, enabling high-performance imaging in the fiber-based PSOCT system [21]. Two distinct incident polarization states in the measurements, which can practically be realized by additional hardware modules that however reduce the imaging range by half, or are expensive, and require additional hardware control which can complicate the imaging system setup. Multiple measurements can also be used to provide two input polarization states. However, this method is sensitive to motion artifacts.

1.5 SCOPE OF THE THESIS

The objective of this thesis is to develop techniques to obtain the depth-resolved birefringent information within the sample in a PSOCT system with neat system setup and sufficient imaging quality. To achieve so, firstly, a single input PSOCT imaging system with an improved image contrast is developed and will be discussed in Chapter 2. In the chapter, a novel algorithm where the polarization state is visualized by the Stokes parameters-based color-encoded method is developed to provide high contrast imaging for birefringent samples. Chapter 3 and 4 will present novel algorithms based on the Stokes parameters calculus on the Poincare sphere that can derive depth-resolved polarization parameters in the single input PSOCT system with sufficient imaging quality. Following in Chapter 4, the developed DDG-based PST method will be utilized to extract the collagen organization embedded within soft biological tissues such as myocardial fibers and human facial skin. In Chapter 5, the DDG-based PST method will be applied for the detection of the white spot lesions in enamel. The last chapter of the thesis will summarize and make a conclusion of the research, and propose future directions.

Chapter 2. IMAGING AND VISUALIZATION OF THE POLARIZATION STATE OF THE PROBING BEAM IN POLARIZATION-SENSITIVE OPTICAL COHERENCE TOMOGRAPHY

2.1 BACKGROUND AND MOTIVATION

Optical coherence tomography (OCT) is a non-invasive optical imaging technique that can generate cross-sectional images of highly scattering samples, enabling the visualization of 3D microanatomical information with high resolution (1-20 μm) [15]. To provide additional contrast when imaging birefringent samples, polarization-sensitive optical coherence tomography (PSOCT) has been developed to characterize anisotropic biological structures, such as tendon, muscle, collagen and nerve fiber bundles [18, 19, 21, 22, 54-57]. In this development in order to fully describe the birefringent property of the biological sample, it typically requires to derive three polarization-related parameters, e.g., phase retardation, optic axis orientation, and degree of polarization (DoP), from the PSOCT measurements, simply because one parameter alone is only useful to give partial birefringent information [18, 19, 21, 22, 54-57]. When dealing with highly absorbing tissue, the measurement of diattenuation is also required [16]. Due to unilateral and limited information that can be provided by each parameter, the contrast and information content are often relatively low.

The phase retardation and axis orientation of the birefringent tissue, either individually or combined, would change the polarization state of the probing beam. Then, one may think just to use the polarization state as the PSOCT imaging parameter to present or visualize the birefringent tissue sample. The reasoning of such treatment may be justified by a Poincaré sphere whose surface represents all possible polarization states of the light. In the Poincaré sphere, the polarization state can be expressed as a Stokes vector whose terminal point is on the sphere. When a polarized probing light travels through a birefringent sample and emerges at the tissue surface, its polarization state (Stokes vector) S_{out} can be obtained by rotating the input polarization state S_{in} about an axis $\vec{\omega}$ by an amount δ, where $\vec{\omega}$ represents the optic axis of the sample and the rotation amount δ represents the phase retardation [19]. The process that birefringent material changes the polarization state of the probing light can be expressed by using the quaternion method [58]:

$$S_{out} = q \cdot S_{in} \cdot \bar{q}, \tag{2.1}$$

where $q = (q_0, \vec{q}) = (cos\frac{\delta}{2}, sin\frac{\delta}{2}\vec{\omega})$ is a rotation operator that consists of phase retardation δ and orientation axis $\vec{\omega}$. That is to say, the change of the polarization state can be used to fully describe the integrated birefringent properties of a sample. Therefore, when the input polarization state is known, the output polarization state can be used to contrast the birefringent properties of the tissue sample.

However, challenge appears when imaging the polarization state because at least three parameters are needed to describe one polarization state. There are a number of techniques that can be used to measure/determine the polarization state, however, most of the prior studies fail to present the complete polarization information of probing light (i.e. polarization state) in the resultant image. Instead, studies [59-61] opted for using specific parameters that only contain partial polarization information to present the polarization properties of the probing light when traveling through tissue sample, for example, phase retardation, axis orientation, DoP [51], degree of linear polarization [61]and degree of circular polarization [61].

To overcome the difficulty of using multiple parameters separately to characterize birefringent tissue, here we propose a simple and efficient approach that is designed to utilize the multidimensional color space where each color is encoded with one specific measurement so that the complementary information from each measurement is integrated into one resultant map which is then displayed for visualizing the birefringent property of the tissue sample. In particular, we propose to encode Stokes parameters in the color space to visualize the polarization state of the probing light. In this way, the polarization state is determined and expressed in Stokes domain. The primary colors of red, green and blue are used to encode each Stokes parameter of Q, U and V, respectively. Because Q, U and V together determine unique a polarization state, combining them in one color domain can represent and visualize that polarization state. Thus, the proposed strategy for PSOCT imaging is to use the polarization state as the imaging parameter to represent the comprehensive birefringent property of the tissue sample in one resultant true-color image.

2.2 MATERIAL AND METHODS

2.2.1 System setup and color-encoded Stokes parameters method

A swept source PSOCT system (Fig. 2.1A) was used in this study to demonstrate the proposed method and strategy. The light source was an akinetic swept source based on Vernier-tuned distributed Bragg reflector (Insight Photonic Solutions, Inc.), which operates at 1,310 nm central wavelength with a sweeping rate of 150 kHz. The output of the swept source was sent to a polarization controller and became linearly polarized and was then split into two arms of the PSOCT system. The sample arm was equipped with a quarter-wave plate (QWP) aligned at 45° with the input polarization state which makes the linearly polarized light become a circularly polarized light before illuminating the sample. The reference arm was installed with a QWP with axis aligned at 22.5° with the input polarization state, ensuring that the reflected light couples equally in the vertical and horizontal channels. The lights coming back from both reference and sample arms were recombined and sent to two polarization beam splitters (PBS1 and PBS2), respectively, where the interference light is split into horizontal and vertical components. Balanced detection with signal amplification was achieved for both vertical and horizontal channels by collecting the interference patterns returning from different light paths. The corresponding interference signals, recorded by the photodetectors, can be written as:

$$\boldsymbol{A_1(z)} = \frac{\sqrt{\boldsymbol{R_1(z)}}}{\boldsymbol{2\sqrt{2}}}\boldsymbol{cos[\phi_1(z)]}, \qquad A_2(z) = \frac{\sqrt{R_2(z)}}{2\sqrt{2}}cos[\phi_2(z)] \tag{2.2}$$

For the two polarization channels, the magnitudes (A_1 and A_2) and phases (ϕ_1 and ϕ_2) of the complex profiles are calculated. Stokes parameters (I, Q, U and V) expressed in the variables describing the electric field components can be calculated as:

$$\begin{aligned} I &= < {A_1}^2 > + < {A_2}^2 >, \\ Q &= < {A_1}^2 > - < {A_2}^2 >, \\ U &= 2 < A_1 A_2 cos\,(\phi_2 - \phi_1) >, \\ V &= 2 < A_1 A_2 sin\,(\phi_2 - \phi_1) >. \end{aligned} \tag{2.3}$$

The transverse and axial resolution of the system were about 7.5 μm and 15 μm in air, respectively. The incident power at the sample was 3.5 mW. The sensitivity of the system is 105 dB. The primary colors of red, green and blue are used to code each Stokes parameter of Q, U and V, respectively, to result in one final image for visualizing the polarization state, representing the birefringent property of the probed sample. A Poincaré sphere whose surface represents all the polarization state is color-encoded by this method as shown in Fig. 2.1B, where each polarization state is represented and visualized by a unique color.

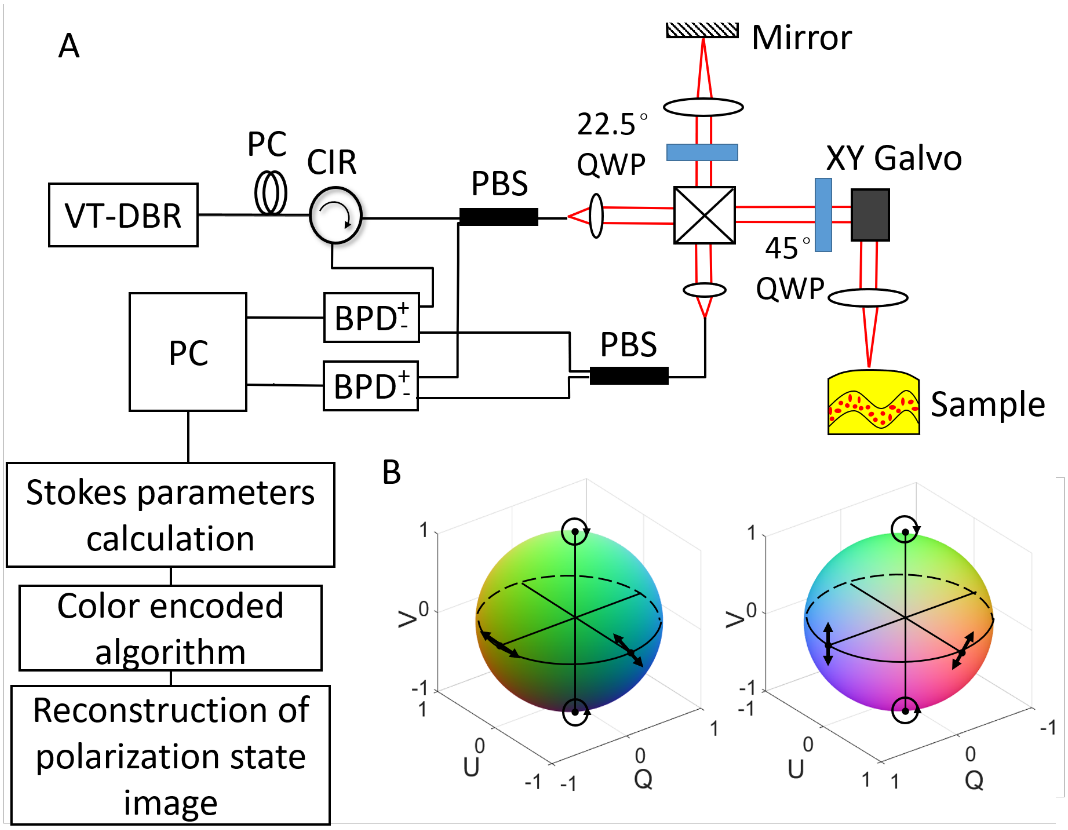

Figure 2.1. Schematic diagram of the swept source PSOCT system. A) Schematic layout of the swept source PSOCT system used in this study. VD-DBR: Vernier-tuned distributed Bragg reflector; PC: polarization controller; CIR: polarization maintaining circulator; PBS: polarization beam splitter; QWP: quarter wave plate; BPD: balanced photodetector; B) The front side and back side of the color-encoded Poincaré sphere. Each color on the surface of the sphere represents a unique polarization state.

2.3 RESULTS

2.3.1 Experimental demonstration of polarization state (Stokes parameters) measurement and visualization

To demonstrate that our proposed color-encoding method of Stokes parameters can visualize the polarization state, we first used the above PSOCT system to detect/image linearly polarized light with various polarization directions that were purposely generated. The equator of the color-encoded Poincaré sphere which represents all the linearly polarized light was used to validate the resultant polarization state images of known linearly polarized lights. In this experiment, a linearly polarized light with Stokes parameters of (Q: 0.9986, U: 0.0314, V: -0.0376) was spilt into the sample arm and passed through a quarter-wave plate to illuminate the sample. A reflecting mirror was used as the sample to reflect the probing light without changing the polarization state. Because OCT detection is a round trip, which enforces the input linearly polarized light pass through the quarter-wave plate twice, the detected light is also a linearly polarized light but with altered polarization direction as shown in Fig. 2.2A. Its direction depends on the orientation of the QWP. The rotation angle of the detected linearly polarized light is twice the angle between the axis orientation of QWP and input light. By rotating the QWP from 0° to 90°, linearly polarized light whose direction ranges from 0° to 180° were generated and detected by the PSOCT system. Stokes parameters of the detected light were evaluated by Eq. (2.1) and compared with the theoretical values. The results are shown in Fig. 2.2C where the measured Stokes parameters match very well the theoretical values, indicating that the detected light is linearly polarized. Polarization state images of these linearly polarized light signals were obtained by the color-encoding algorithm (Fig. 2.2C). As the angle of the linearly polarized light increased from 0° to 180°, the color of the polarization state changes from purple, pink, yellow, green, blue and purple again, which is consistent with the equator of the color-encoded Poincaré sphere (Fig. 2.2B). These results experimentally demonstrate that the proposed method based on color-encoded Stokes parameters is practically useful to image the polarization state of the probing light.

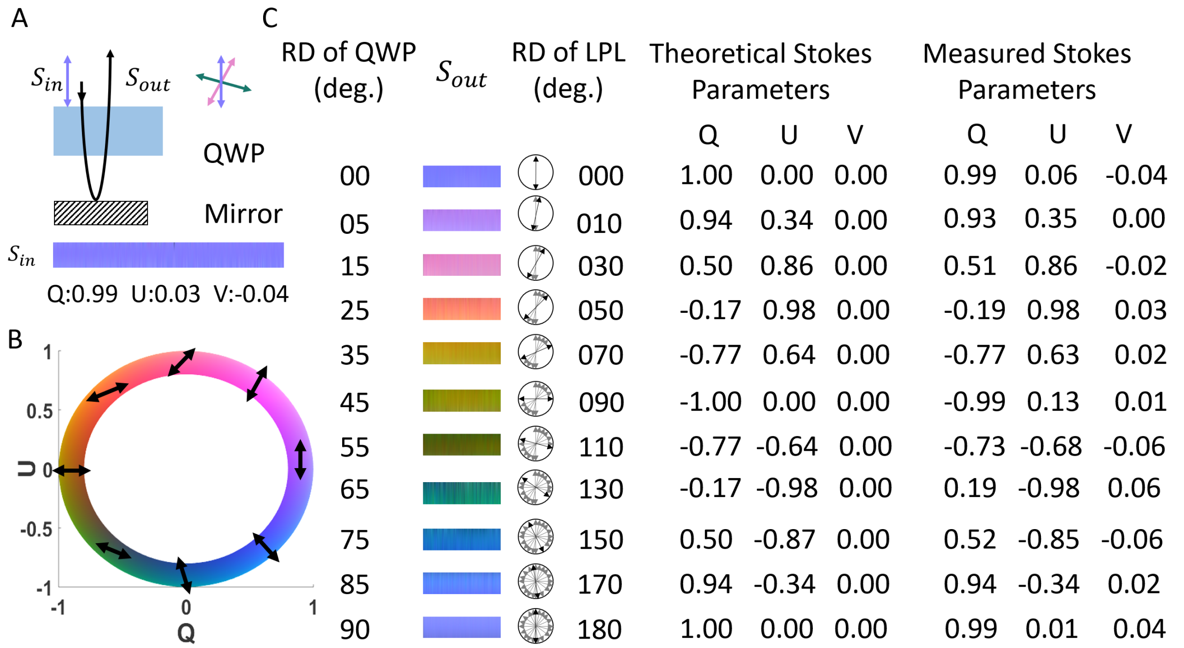

RD of QWP (deg.)	S_{out}	RD of LPL (deg.)	Theoretical Stokes Parameters Q	U	V	Measured Stokes Parameters Q	U	V
00	▨	000	1.00	0.00	0.00	0.99	0.06	-0.04
05	▨	010	0.94	0.34	0.00	0.93	0.35	0.00
15	▨	030	0.50	0.86	0.00	0.51	0.86	-0.02
25	▨	050	-0.17	0.98	0.00	-0.19	0.98	0.03
35	▨	070	-0.77	0.64	0.00	-0.77	0.63	0.02
45	▨	090	-1.00	0.00	0.00	-0.99	0.13	0.01
55	▨	110	-0.77	-0.64	0.00	-0.73	-0.68	-0.06
65	▨	130	-0.17	-0.98	0.00	0.19	-0.98	0.06
75	▨	150	0.50	-0.87	0.00	0.52	-0.85	-0.06
85	▨	170	0.94	-0.34	0.00	0.94	-0.34	0.02
90	▨	180	1.00	0.00	0.00	0.99	0.01	0.04

Figure 2.2. Experimental demonstration of polarization state (Stokes parameters) measurement and visualization. A) Schematic diagram of the round-trip optical path of the probing light in the sample arm. When a linearly polarized light passes through a quarter-wave plate twice, the output light is also linearly polarized but with its orientation dependent on the axis orientation of the quarter-wave plate; B) Equator of the color-encoded Poincaré sphere,

representing all possible linearly polarized light; C) Measurement and visualization of the polarization state (Stokes parameters) of linearly polarized lights that were generated by rotating the quarter-wave plate. Sin/Sout: polarization state of the input light and output light, respectively; RD: rotating degree; QWP: quarter-wave plate; LPL: linearly polarized light.

2.3.2 PSOCT images of the birefringent components within the mouse tail

The imaging performance of the PSOCT system that utilizes the polarization state as the imaging parameter with a color-encoded algorithm was then demonstrated by imaging a mouse tail tissue with a purpose to differentiate its birefringent tissue components, for example, nerve bundle and muscle groups. Fig. 2.3 shows the reflectivity, phase retardation, relative axis orientation and polarization state images of the mouse tail, respectively. The upper row is the images generated by top-viewing the volumetric rendered corresponding 3D datasets. The bottom row is the cross-sectional images whose locations are indicated by the white line in the corresponding top-row images. The reflectivity image (Fig. 2.3A) is relatively uniform across the tissue, giving useful microanatomical information but not the birefringent. Two muscle groups (labeled as 1 and 2) can be roughly identified. Since muscles, vessel walls of artery and veins, and nerve bundles are highly birefringent, they are better identified and visualized in the polarization images. In the phase retardation image (Fig. 2.3B), although the nerve bundle (labeled by 3) and the vascular walls (pointed by 4) can be visualized, their contrasts are relatively low. Moreover, muscles with different orientations are difficult to be differentiated in both 3D and cross-sectional images by using phase retardation as the imaging parameter. This is because the phase retardation image does not contain the orientation information. In the orientation image (Fig. 2.3C), both nerve and vascular walls can be visualized. Muscles with different orientations can also be differentiated by colors. But still, the contrast and signal-to-noise ratio (SNR) of this image are low (where the nerve bundle is hardly differentiated from the background) because phase retardation information was lost in this image. In the polarization-state image obtained using our proposed strategy (Fig. 2.3D), all the birefringent tissue components (pointed by 1-4） can be contrasted with higher resolution and SNR, when compared with Figs. 2.3A – 2.3C. In the cross-sectional image, two muscle groups can be differentiated with higher contrast by using polarization state as the imaging parameter. For example, a sharp change from green to orange is found in Fig. D, differentiating two different muscle groups with different axis orientations. Moreover, the nerve bundle and vascular walls can also be extracted with higher resolution and SNR in the cross-sectional polarization state image as shown in the zoomed view of the regions marked by the white box. Overall, using polarization state as the imaging parameter can provide a higher quality of images for better visualization and differentiation of the birefringent tissue components. This is largely attributed to that both phase retardation and orientation information are organically integrated into a single polarization state image. These results sufficiently demonstrate the practical usefulness of the proposed strategy of using polarization state as the imaging parameter in the PSOCT imaging of biological samples, indicating potential applications in both pre-clinical and clinical environments where accurate identification of birefringent tissue components is important, for example, the nerve identification in the delicate surgical remove of the diseased tissue mass in surgery.

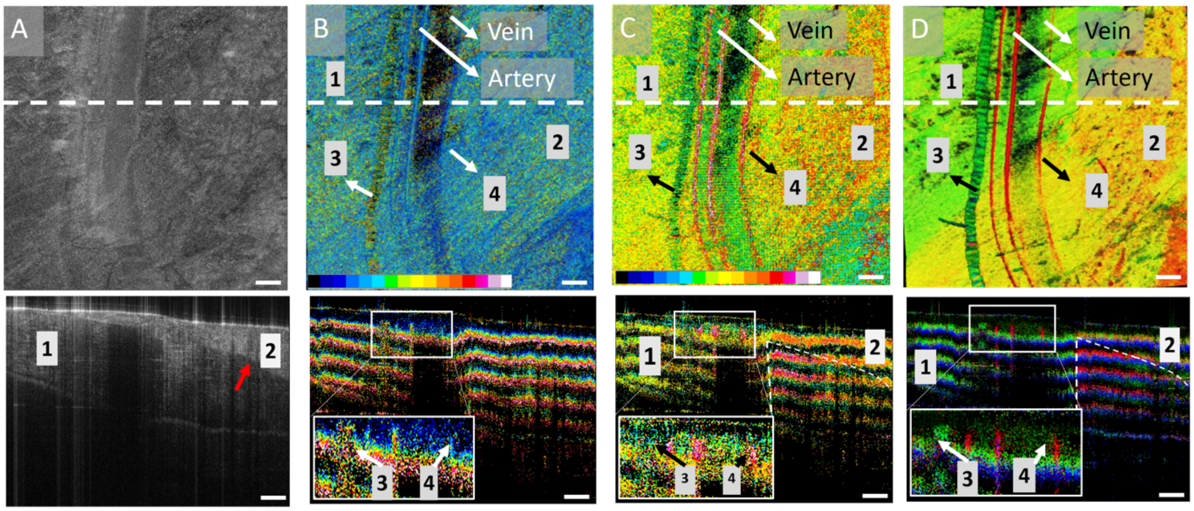

Figure 2.3. PSOCT images of the mouse tail provides ability to differentiate the birefringent tissue components from background tissue. A) Results using OCT reflectivity (intensity) as the imaging parameter; B) results using phase retardation as the imaging parameter (color bar: 0° to 90°); C) results using axis orientation as the imaging parameter (color bar: −90° to 90°); D) results using the proposed polarization state of the probing beam as the imaging parameter (color bar: color-encoded Poincaré sphere shown in Fig. 1B). 1-2: muscles; 3: nerve bundle; 4: vascular walls of artery and veins; The scale bars represent 300 µm.

2.3.3 Volumetric polarization state images of mouse brain tissue ex vivo

To demonstrate, we imaged a mouse brain ex vivo. A fresh brain was extracted from a euthanized mouse within 1 hour and placed under the PSOCT system in a prone position for imaging. The imaging protocol was the same as the previous experiment, but with a field of view of 12 mm x 12 mm to have a full coverage of the brain tissue. The total acquisition time is 13.2 s. The 3D results are given in Fig. 2.4 showing (A) the reflectivity, (B) axis orientation, (C) polarization state image and (D) polarization state images with automatic segmentation of the nerve bundles, respectively. Again, the images at the top row are the top-views of 3D rendered datasets, and those at the bottom are the representative cross-sectional images at the position marked as the white line at the top. The reflectivity image (Fig. 2.4A) does not provide the ability to visualize the nerve bundles. Although the nerve bundles can be seen in the 3D axis orientation image (Fig. 2.4B) and polarization state image (Fig. 2.4C), the contrasts are too low because the signals that represent nerve bundles are almost totally embedded within a high background signal that is generated by the non-birefringent tissue of gray and white matters (see the cross-sectional images shown in the bottom row). Particularly when evaluating the axis orientation maps, since optic axes do not exist in the non-birefringent tissue, the Jones Matrix algorithm would not work properly, leading to a high background random noise (Fig. 2.4B) that would make it extremely difficult to segment the birefringent nerve bundles. Different from the orientation image, the colors of the non-birefringent tissue of the brain appear uniform in the polarization state image (Fig. 2.4C). A color filter whose RGB parameters were the same as the incident light was then applied to Fig. 2.4C for automatic nerve bundle segmentation. The result is shown in Fig. 2.4D, where the 3D nerve bundles within the scanned tissue volume including optic tract, olfactory tract and corpus callosum tract, etc. are extracted clearly with high contrast and high SNR, indicating that the non-birefringent tissue background can be easily removed by the color-based segmentation and the specific birefringent sample can be extracted and presented with high SNR. In addition, the olfactory nerves (appearing purple in color) that are indicated in the zoomed view of the regions marked by the red box cannot be visualized in the orientation image (Fig. 2.4B). This is because the axis orientation of the purple bundle is not in the QU plane while the Jones Matrix-based algorithm that is used to calculate the orientation is based on the assumption that the axis orientation of the plane is in the QU plane. Thus, the vertical component of the axis orientation in the Stokes space is lost. This is why some of the birefringent sample (especially those samples which are inclined at a large angle) lost their contrast in the orientation image. In the Poincaré sphere (i.e. Stokes domain), the output polarization state can be obtained by rotating the input polarization state about the 3D axis orientation of the sample by an amount of δ. That is, the 3D axis orientation information is retained in the polarization state of the probing light. Therefore, when the output polarization state is used as the imaging parameter, 3D information of the axis orientation in the Stokes space can be retained, which makes the proposed method to have improved visualization of the nerve fibers.

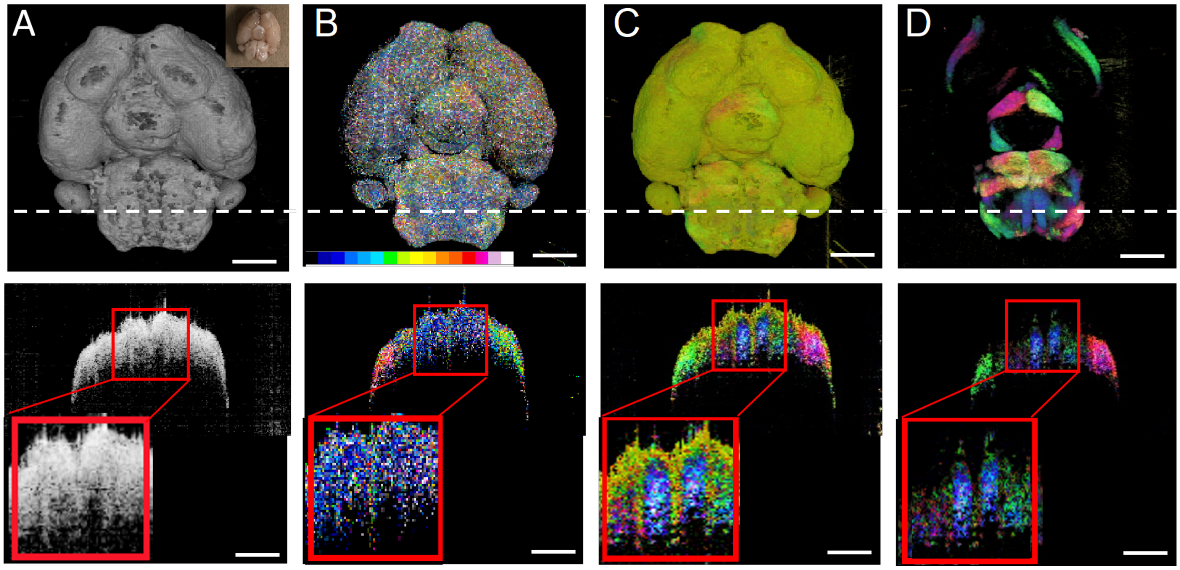

Figure 2.4. Volumetric polarization state images of mouse brain tissue ex vivo. A) Images resulted from using reflectivity as the imaging parameter; B) Results using optic axis as the imaging parameter; C) Results using the polarization sate as the imaging parameter, and D) the same as in (C) but after the automatic color filter segmentation, showing high contrast of nerve bundles. (color bar: color-encoded Poincaré sphere). The images in the top row are the top views of corresponding 3D datasets, and those at the bottom are the representative cross-sectional images at the positions marked as white lines in the top. [Color bars: B] −90° – 90°; C] and D] color-encoded Poincaré sphere shown in Fig. 2.1B]. The scale bars represent 3 mm.

2.4 DISCUSSION AND CONCLUSION

While we have demonstrated the usefulness of the proposed color-encoding Stokes parameters to visualize the birefringent components within scanned tissue volume, further improvement is required to decouple the phase accumulation effect over depth so that localized birefringent information can be unambiguously revealed, which will be discussed in the next chapter. One another improvement that requires the attention is on the system development to minimize the system phase noise and avoid the polarization mode dispersion because both of them can add bias to the evaluation of phase retardation, leading to inaccurate derivation of the localized parameters discussed above [19].

In conclusion, we have demonstrated a method based on color-encoded Stokes parameters to visualize the polarization state in the PSOCT characterization of birefringent tissue samples. We have shown that this method can provide complete polarization information of the probing light, rather than individual polarized components, which has never been demonstrated before. We have also demonstrated a useful yet simple automatic segmentation scheme that uses a color filter to efficiently isolate specific birefringent tissue components embedded within a high non-birefringent tissue background. With this method, we have shown its ability to provide the network of the nerve bundles of the mouse brain noninvasively. It is hoped that the proposed polarization state imaging and the segmentation scheme have useful and practical applications in the investigations of birefringent samples both pre-clinically and clinically.

Chapter 3. POLARIZATION STATE TRACING METHOD TO MAP LOCAL BIREFRINGENT PROPERTY IN SAMPLE USING POLARIZATION SENSITIVE OPTICAL COHERENCE TOMOGRAPHY

3.1 BACKGROUND AND MOTIVATION

In biomedical imaging to determine birefringent properties of a tissue sample, the parameters such as orientation, phase retardation, degree of polarization uniformity and diattenuation are important determinants. These parameters may also be utilized, either alone or combined, to reveal several important physiological processes such as the dynamics of the myocardial fibers [57, 62], skin lines of the human body [55] and wound healing process [63].

As mentioned above, polarization-sensitive optical coherence tomography (PSOCT), an extension of conventional optical coherence tomography (OCT), characterizes cross-sectional anisotropic biological structures, such as tendon, muscle, collagen and nerve fiber bundles non-invasively [54]. This polarization-based three-dimensional (3D) imaging technique has potential applications in ophthalmology, dermatology, and other areas. Due to the round-trip measurement, traditional PSOCT only provides the accumulated polarization results along with depth, leading to a difficulty to determine local birefringent information at depth (e.g. orientation of the optic axis and phase retardation).

An elegant Jones matrix-based algorithm was developed to map local axis orientation using a single incident polarization state [18], in which local axis orientation is considered as a scalar constrained within QU-plane. However, the asymmetry in the imaging system (i.e., the optical path in the system is not round-trip) can cause an overall rotation of the optic axes away from the QU-plane [21, 64-66]. That is, the local axis orientation to be measured becomes a 3D vector in Stokes space. As such, the algorithm would result in inaccurate determination of the local optic axis orientation and local phase retardation over depth.

The 3D local axis orientation in Stokes space can also be achieved by using two distinct incident polarization states in the measurements [19, 21, 22], which can practically be realized by additional hardware modules that however reduce the imaging range by half [67, 68], or are expensive, and require additional hardware control which can complicate the imaging system setup [19, 69, 70].

Here we propose a Stokes parameter-based polarization state tracing (PST) method to find the exact optic axes of interest in the 3D space in the Poincaré sphere. Different from the previous method that depends on the Jones matrix calculus, the method we propose here utilizes the geometrical trajectory of the output polarization states on the Poincaré sphere to derive the local birefringent information. The apparent axis and the local phase retardation are first obtained by fitting a plane to the adjacent output polarization states along with depth in the Poincare sphere. Then a sequence of 3D rotation operation is applied to the apparent axis to finally determine the local optic axis. This method requires only one input polarization state, which relaxes the PSOCT system setup. In this paper, theoretical derivation to obtain local optic axis and phase retardation is presented, and then demonstrated by imaging the mouse thigh tissue in vitro.

3.2 MATERIAL AND METHODS

3.2.1 Derivation of the local optic axis

In a Poincaré sphere representation, linear polarization can be modeled as a rotation about its optic axis. The amount of rotation is the degree of phase retardation [65]. That is when a polarized light propagates through a multi-layered material with a constant optic axis, the trajectory of the output polarization states of the light beam on the Poincaré sphere are constrained within a plane whose normal vector defines the optic axis. Based on this model, the local optic axis and phase retardation of a multi-layered tissue sample can be obtained by fitting a plane to the output polarization states along the depth represented at the Poincare sphere. Here, the output polarization states are directly given by the Stokes parameters determined by the measured quantities of the PSOCT system [71, 72].

To illustrate, Fig. 3.1 shows a schematic diagram of the polarization states of the light beams traveling through a simulated birefringent sample with a depth-varying optic axis. To simplify, we model the sample to consist of two groups of birefringent material with their optic axes represented by $\overrightarrow{A_1}$ and $\overrightarrow{A_2}$, respectively (Fig. 3.1A). The first group is made up of two retarder layers (gray layer) sharing the optic axis of $\overrightarrow{A_1}$, whereas the 2nd group is also of two retarder layers (yellowish layer) but sharing the optic axis of $\overrightarrow{A_2}$. With this arrangement when the light beam propagates within this sample, there will be five interfaces that would back-scatter the incoming light to the PSOCT detector. For the light beams scattered back from the sample surface and the first two gray layers, the output polarization states P_1, P_2 and P_3 are represented by the black points on the Poincaré sphere as shown in Fig. 3.1B. As the first two layers share the same optic axis $\overrightarrow{A_1}$, P_1, P_2

and P_3 must be in the same plane whose normal vector is $\overrightarrow{A_1}$ based on the model mentioned above. Hence, by fitting a plane to the output polarization states P_1, P_2 and P_3 on the Poincaré sphere, the local optic axis of the gray layers can be obtained that equals to the normal vector of that fitted plane.

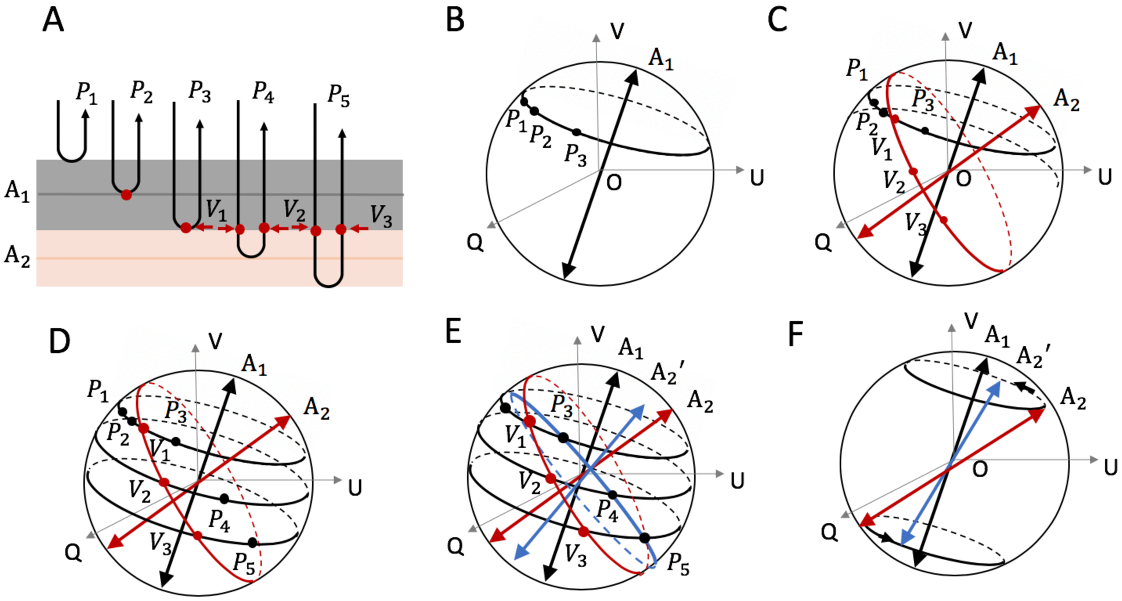

Figure 3.1. Schematic diagram of the polarization states of the light beams traveling through a simulated birefringent sample with depth-varying optic axis and eventually forming the output polarization states, P1, P2, …, P5, that are detected by the PSOCT system. A) A depth scan of a simulated birefringent sample with depth-varying optics axis, where 4 birefringent layers are simulated with the first 2 layers sharing the same optic axis A_1, and the last two layers sharing A_2. B) The trajectory of the output polarization states P_1, P_2 and P_3 on the Poincaré sphere, which forms a plane with a normal vector of A_1. C) The trajectory of the intermediate polarization states V_1, V_2 and V_3 on the Poincaré sphere, which also form a plane with a normal vector of A_2. D) The trajectory of the output polarization states P_3, P_4 and P_5 on the Poincaré sphere, which forms a plane with a normal vector of $A_2{}'$. E-F) The geometric relation between the upper optic axes, A_1, the axis of the local fitted plane $A_2{}'$ and the local optic axis A_2.

For the light scattered back from the deeper layers with a differed optic axis of $\overrightarrow{A_2}$, the resultant output polarization states would be determined by both the layer of interest and all the layers that are on top of that layer due to the round-trip measurement. Here, we discuss in detail the intrinsic geometric relationship among the upper optic axes, the axis of the local fitted plane at the Poincare sphere and the local optic axis of interest, and the use of which to derive the local optic axis in the deeper layers. Figs. 3.1C-F illustrates the geometric relationship by presenting the transmission process of the light polarization states in the sample. In these figures, P_3, P_4 and P_5 indicated by the black points on the Poincaré sphere are the output polarization states scattered back from the interface between the gray and yellowish layers, and the last two yellowish layers as shown in Fig.

3.1A. These polarization states are directly represented by the measurements of the PSOCT system. V_1, V_2 and V_3 indicated by the red points on the Poincaré sphere (Figs. 3.1C-E) represent the intermediate polarization states of the light beams when they pass through the interface between the yellowish and gray layers as shown in Fig. 3.1A. Because the change in the polarization states from V_1 to V_2 or V_1 to V_3 is only introduced by the yellowish layers, V_1, V_2 and V_3 should be in the same plane at the Poincaré sphere. And its normal vector (determined by V_1, V_2 and V_3) represents the local optic axis $\overrightarrow{A_2}$ of the yellowish layers as shown in Fig. 3.1C. However, due to the round-trip nature of the OCT measurement, V_1, V_2 and V_3 are the intermediate states of the light beams and are not measured directly. Hence, the local optic axis in the deeper layer cannot be directly obtained.

Since all of the light beams scattered back from the yellowish layers have to propagate through the same group of the upper gray layers again to reach the PSOCT system for detection, the intermediate states V_1, V_2 and V_3 would each experience the same change due to the upper gray layers to form the resultant output polarization states, P_3, P_4 and P_5 for detection as shown in Fig. 3.1A. In the Poincaré sphere representation, this change (due to the gray layers) can be viewed as an overall rotation operation that rotates the points V_1, V_2 and V_3 about the axis $\overrightarrow{A_1}$ by an angle δ to P_3, P_4 and P_5 respectively as shown in Fig. 3.1D. The angle $\delta = \delta_1 + \delta_2$ is determined by the local phase retardations of the first two gray layers. In other words, the output polarization states P_3, P_4 and P_5 would form a plane (with a normal vector of $\overrightarrow{A_2{}'}$) in the Poincaré sphere. This plane can be obtained by rotating the plane determined by V_1, V_2 and V_3 about axis $\overrightarrow{A_1}$ by an angle -δ as shown in Fig. 3.1E. To summarize, to obtain the local axis $\overrightarrow{A_2}$, it just needs to rotate $\overrightarrow{A_2{}'}$ about $\overrightarrow{A_1}$ by -δ as shown in Fig. 3.1F. This geometric relationship can be expressed as a matrix rotation in the calculation:

$$\overrightarrow{A_2} = \boldsymbol{R_1}(-\delta; \overrightarrow{A_1})\overrightarrow{A_2{}'} \tag{3.1}$$

where $\overrightarrow{A_1}$, $\overrightarrow{A_2}$ and $\overrightarrow{A_2{}'}$ are the 1x3 matrices represented by the corresponding Q, U and V values; $\boldsymbol{R_1}(-\delta; \overrightarrow{A_1})$ is the 3D rotation matrix determined by $\overrightarrow{A_1}$ and $-\delta$.

This derivation process can be generalized to the sample with varied optic axes along depth. As the orientation within the biological sample is continuous, we can assume that at least three adjacent OCT pixels in the depth direction of the sample share the same local optic axis, which can compose a plane at the Poincaré sphere. Generally, each of the layers above the layer of interest can rotate the local optic axis to form the final normal vector of the local fitted plane. Each rotation is determined by the local optic axis and phase retardation of the certain layer. Hence, to obtain the local optic axis $\overrightarrow{A_n}$, a series of rotations are applied:

$$\overrightarrow{A_n} = \boldsymbol{R_{n-1}}(-\delta_{n-1};\overrightarrow{A_{n-1}}) \dots \boldsymbol{R_2}\big(-\delta_2;\overrightarrow{A_2}\big)\boldsymbol{R_1}(-\delta_1;\overrightarrow{A_1})\overrightarrow{A'_n}, \tag{3.2}$$

where δ_n is the local phase retardation of the n-th layer, $\overrightarrow{A'_n}$ is the normal vector of the local fitted plane, $R_n(-\delta_n;\overrightarrow{A_n})$ is the 3D rotation matrix determined by δ_n and $\overrightarrow{A_n}$.

3.2.2 Derivation of the local phase retardation

The local phase retardation can also be evaluated and calculated with the use of the Poincaré sphere. In doing so, one straightforward approach is to calculate the local phase retardation progressively through depth (i.e., layer by layer). Based on the geometric model as discussed above, assuming that the sample has the *n* homogeneous birefringent layers with each layer having known local input/output polarization states $\overrightarrow{S_{in}^n}/\overrightarrow{S_{out}^n}$ and its local optic axis A_n, the local phase retardation δ_n for the n^{th} layer can then be obtained by

$$\delta_n = \frac{1}{2} arccos \frac{[\overrightarrow{S_{in}^n}\times\overrightarrow{A_n}]\cdot[\overrightarrow{S_{out}^n}\times\overrightarrow{A_n}]}{\left|\overrightarrow{S_{in}^n}\times\overrightarrow{A_n}\right|\left|\overrightarrow{S_{out}^n}\times\overrightarrow{A_n}\right|} \tag{3.3}$$

The input/output polarization state $\overrightarrow{S_{in,out}^n}$ at the local layer *n* can be derived from a series of rotations:

$$\overrightarrow{S_{in}^n} = \overrightarrow{S_{in}}\boldsymbol{R_1}(\delta_1;\overrightarrow{A_1})\boldsymbol{R_2}(\delta_2;\overrightarrow{A_2}) \dots \boldsymbol{R_{n-1}}(\delta_{n-1};\overrightarrow{A_{n-1}}),$$

$$\overrightarrow{S_{out}^n} = \overrightarrow{S_{out}}\boldsymbol{R_1}(-\delta_1;\overrightarrow{A_1})\boldsymbol{R_2}(-\delta_2;\overrightarrow{A_2}) \dots \boldsymbol{R_{n-1}}(-\delta_{n-1};\overrightarrow{A_{n-1}}). \tag{3.4}$$

From this treatment, it is trivial to appreciate that the value of the local phase retardation is dependent on the calculated local values of all the layers that are above the layer of interest, which are not from the direct measurements. That is, the errors in the calculation can be propagated and accumulated along the depth. On the other hand, there is also possible errors in the each of the multiple steps in the calculation. Such treatment is clearly not optimal.

To mitigate this issue, here we propose a strategy that calculates the local phase retardation by using two adjacent output polarization states along the depth (that are detected by the PSOCT system), where the phase retardation of each layer can be simply obtained by:

$$\delta_n = \frac{1}{2} arccos \frac{\overrightarrow{[P_{n-1} \times A_n{}']} \cdot \overrightarrow{[P_n \times A_n{}']}}{\left|\overrightarrow{P_{n-1} \times A_n{}'}\right| \left|\overrightarrow{P_n \times A_n{}'}\right|}\ , \tag{3.5}$$

where $\overrightarrow{P_n}$ is the output polarization state scattered back from the *n*-th layer, $\overrightarrow{A_n{}'}$ is the normal vector of the local fitted plane as discussed in the last section.

Below, we first prove that this formulation is suitable to the sample with a constant optic axis $\vec{A}$ as shown in Fig. 3.2A, i.e. a homogenous birefringent sample. In this case, all the output polarization states that are detected by the PSOCT system are constrained within a defined plane (Fig. 3.2B) and its normal vector of $\overrightarrow{A'}$ equals to the optic axis $\vec{A}$ in the Poincaré sphere representation. Consider the *n*-th layer in Fig. 3.2A, the local phase retardation δ_n is half the angle that rotates the local input polarization state $\overrightarrow{S_{in}^n}$ about $\vec{A}$to the local output polarization state $\overrightarrow{S_{out}^n}$ as shown in Fig. 3.2B, that is, $\delta_n = \frac{1}{2}\angle S_{in}^n O' S_{out}^n$. Note that $\varphi_{n-1} = \angle P_1 O' S_{in}^n = \angle S_{out}^n O' P_n = \angle S_{in}^n O' P_{n-1}$, where $\varphi_{n-1} = \sum_{i=1}^{i=n-1} \delta_i$ is the sum of the phase retardation of all the upper layers. The local phase retardation δ_n can be expressed as $\delta_n = \frac{1}{2}\angle S_{in}^n O' S_{out}^n = \frac{1}{2}\angle P_{n-1} O' P_n$, meaning δ_n can be calculated using Eq. (3.5) under this circumstance.

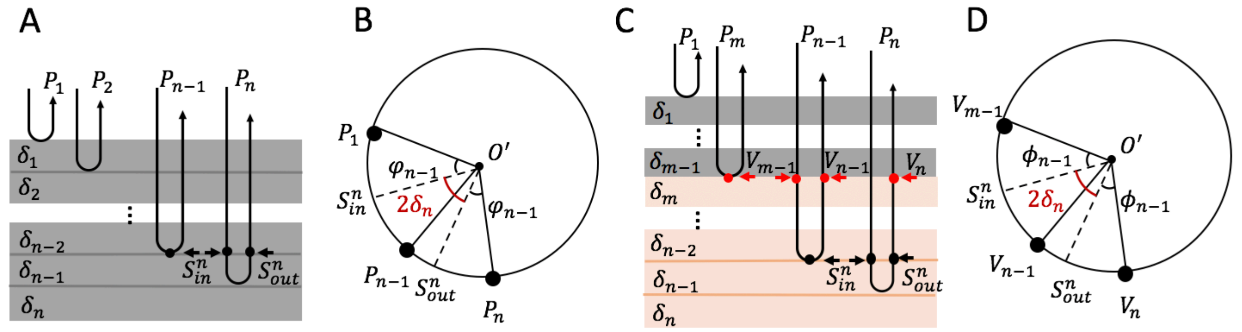

Figure 3.2. Local phase retardation measurement: schematic diagram illustrating the relationship between the output polarization states (which are detected by the PSOCT) and the local phase retardations within a simulated birefringent sample with n layers. A) A depth-scan of a sample with n discrete layers but with constant optic axis throughout. B)

The plane composed by the output polarization states P_1 to P_n within the Poincaré sphere. C) A depth scan of a simulated birefringent sample with depth-varying optic axis. D) The plane composed by the V_1 to V_n within the Poincaré sphere. δ_n is the local phase retardation, $\varphi_{n-1} = \sum_{i=1}^{i=n-1} \delta_i$ is the sum of the phase retardation of all the upper layers, $\overrightarrow{S_{in}^{n}}/\overrightarrow{S_{out}^{n}}$ are the local input/output polarization state.

For the sample with varied optic axes along the depth (Fig. 3.2C), we consider the plane that is determined by the intermediate polarization states $V_{m-1,..,n-1.n}$ experienced by those layers that share the same optic axis and are located below the upper layers as shown in Fig. 3.2C and Fig. 3.2D. In this plane, the local phase retardation of the n-th layer δ_n can be expressed as $\frac{1}{2}\angle S_{in}^{n}O'S_{out}^{n}$. Consider the round-trip measurement, the angle $\varphi_{n-1} = \sum_{i=m}^{i=n-1} \delta_i = \angle V_{m-1}O'S_{in}^{n} = \angle S_{out}^{n}O'V_n = \angle S_{in}^{n}O'V_{n-1}$, and therefore $\delta_n = \frac{1}{2}\angle S_{in}^{n}O'S_{out}^{n} = \frac{1}{2}\angle V_{n-1}O'V_n$. As discussed in the last section, all the intermediate polarization states $V_{m-1,..,n-1,n}$ would travel back through the same groups of the upper layers again, the same rotation operation should apply to these intermediate polarization states to form the final output polarization states $P_{m-1,..,n-1,n}$. That is, the plane composed by $P_{m-1,..,n-1,n}$ is the plane determined by $V_{m-1,..,n-1,n}$ after a rigid rotation. Hence, there is a point to point rotational relation between these two planes and their geometric relation within the plane in the Poincare sphere would keep constant before and after rotation. As a consequence, we arrive at $\delta_n = \frac{1}{2}\angle V_{n-1}O'V_n = \frac{1}{2}\angle P_{n-1}O''P_n$, where O'' is the center of the plane composed by $P_{m-1,..,n-1,n}$ in the Poincaré sphere whose normal vector is $\overrightarrow{A_n}'$. That is, the half-angle that rotates P_{n-1} about $\overrightarrow{A_n}'$ to P_n is equal to the local phase retardation δ_n, meaning that Eq. (3.5) is still valid under this circumstance, and can be generalized to the case with varied optic axis along the depth.

3.3 RESULTS

The proposed PST method was tested on the muscle tissue of a mouse thigh by using the single input PSOCT system. The mouse thigh was selected for demonstration because it anatomically consists of multiple muscle groups arranged with different orientations in the shallow depth that are reachable by the OCT imaging. For imaging, we dissected the thigh tissue from a freshly dead mouse that was disposed from another planned project in our lab. Immediately after dissection, the sample was rinsed with PBS saline solution to keep it from dehydration and then placed under the PSOCT probe for imaging. One B-scan image of the mouse thigh was achieved with 500 A-lines.

Figure 3.3A shows a representative OCT cross-sectional image, where the anatomical information of the thigh tissue sample is delineated up to an imaging depth of ~1.5 mm. Notably, there are three different muscle groups (marked as M_1, M_2 and M_3) that can be approximately appreciated. Within this B-scan, there are dark vertical strips that were caused by the probe beam attenuation due to the coagulated blood within the blood vessels situated in the superficial layer. Due to this effect, these dark strips partitioned the appearance of the muscle groups M_1 and M_3 within this B-scan, where $M_1{}'$ should be part of the muscle group M_1 that stretched under the muscle group M_2, and $M_3{}'$ be part of M_3 group. Such partitions of the muscle groups in the appearance of the OCT scan provide an excellent opportunity to test the proposed algorithm.

Figures 3.3B – 3.3F show the corresponding cross-sectional images of cumulative axis orientation, cumulative phase retardation, axis of the local fitted plane, local axis orientation and local phase retardation images, respectively. From the structural image (Fig. 3.3A), birefringent information of the regions $M_1{}'$ should be the same as that of the region M_1 since they are from the same muscle group. And it is also true for the regions of $M_3{}'$ and M_3. As expected, because of the phase accumulation effect, the conventional PSOCT optic axis map (Fig. 3.3B) and phase retardation map (Fig. 3.3C) are difficult to appreciate the concrete birefringent information of this tissue sample. Fig 3.3D shows the optic axis of the plane directly fitted to the output polarization states (but without applying Eq. 3.2). The banded patterns due to the phase accumulation in Fig. 3.3B are removed successfully, however, the identification of the three muscle groups is ambiguous because the color of the same muscle group appears quite different. For example, the muscle regions M_1 and $M_1{}'$ should have the same optic axis, therefore the same color in this map. However, the color of $M_1{}'$, which is under M_2 appears vastly different from M_1 group and varies laterally towards the right as the thickness of the M_2 is increased. This is because the direction of the axis of the local fitted plane at the $M_1{}'$ region is rotated off the direction of the true local axis of the layer of interest due to the upper layers of M_2 muscle group. As discussed in the last section, for the muscle $M_1{}'$, as the thickness of upper muscle M_2 increases, the rotation matrix applied to the local optic axis rotates more and therefore the axis of that local fitted plane of the muscle $M_1{}'$ is off more, leading to the changes in color representation in the Poincare sphere representation.

Figure 3.3E is the corresponding local optic axis map after applying the proposed PST method. The local optic axes of the sample are recovered, and the three groups of the muscle are differentiated without ambiguity. Each color represents an orientation as shown in the colormap in Fig. 3.3J. The corresponding map of local phase retardation in Fig. 3.3F appears relatively homogeneous, suggesting a uniform distribution of optical retardance in the sample. These results demonstrate the capability of the PST method to derive correctly the local birefringent information. Note that the local phase retardation in some regions indicated by the white box in Fig. 3.3F exhibits a weak periodic variation. This artifact may be caused by the polarization mode dispersion of the optical components used in the system setup [9,18,19].

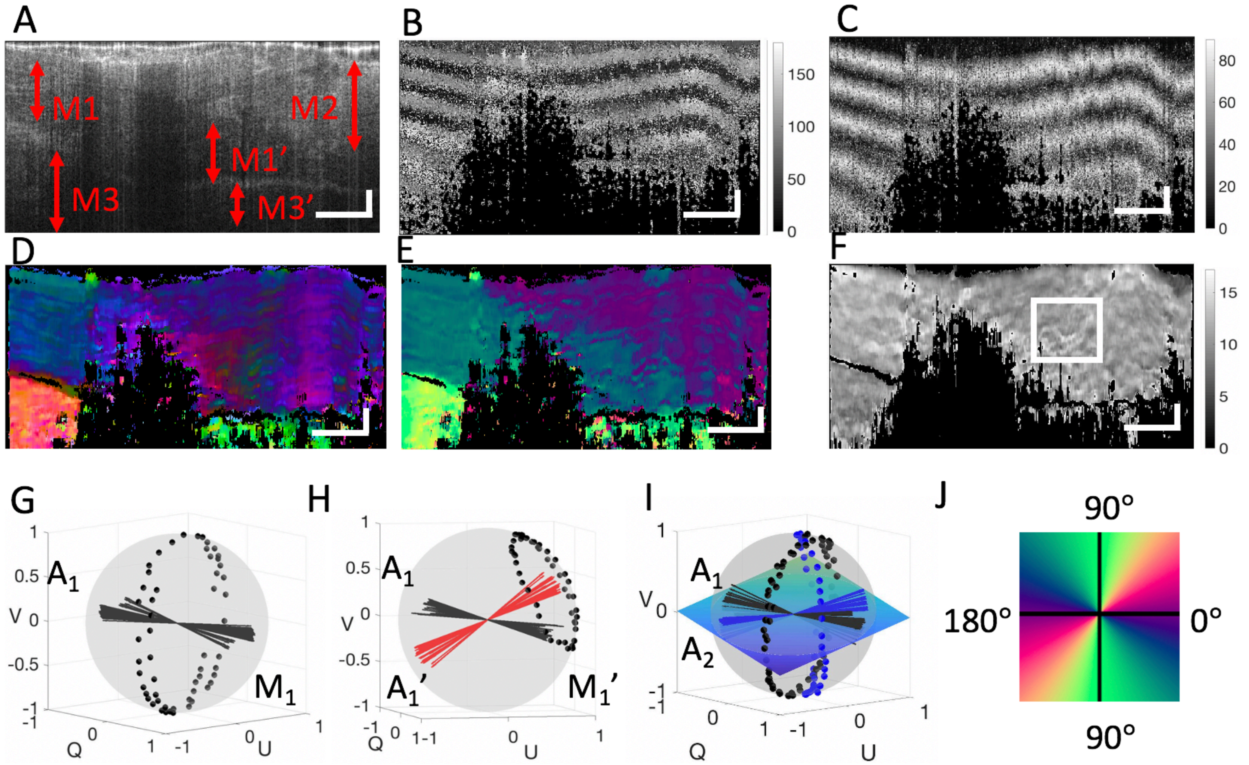

Figure 3.3 PSOCT imaging of the mouse thigh tissue sample that anatomically consists of multiple muscle groups arranged with different orientation. A) Representative cross-sectional B-scan structural image of the sample where three groups of muscle organizations $M_1, M_2, and\ M_3$ can be appreciated. The two vertical dark bands are caused by the light attenuation due to the highly absorbing blood clots within vessels situated at the superficial layer. The vertical dark bands partitioned the muscle group M_1 and M_3 into segments. Segment M_1' should belong to M_1, and M_2' to M_2. B) and C) Corresponding cross-sectional B-scan cumulative optic axis and phase retardation maps where it is difficult to appreciate three muscle groups. D) Corresponding cross-sectional B-scan map of the optic axis of the local fitted plane, where muscle groups can be appreciated but ambiguous. E) and F) Corresponding cross-sectional B-scan maps of the local optic axis and local phase retardation resulted from the proposed PST method, where the three muscle groups are delineated unambiguously. G) The trajectory of the output polarization states scattered back from the depth extent marked by the two-way red arrow left of label M_1 on the Poincaré sphere and the corresponding optic axis A_1 determined by plane fitting. H) The trajectory of the output polarization states scattered back from the depth extent marked by the two-way red arrow left of label M_1' on the Poincaré sphere and the corresponding apparent axis A_1' and the true optic axis A_1. I) The trajectories of the output polarization states on the Poincaré sphere that were scattered back from the depth extent marked by the two-way arrows left to the label M_1 and right to the label M_2, respectively,

where the blue plane is the plane of intermediate optic axes which is fitted by local optic axis A_1 and A_2. J) The colormap used to color-code the maps of the local optic axis. The white lateral and axial scale bars are 1 mm and 0.2 mm, respectively. The units of all the color bars are degrees.

To visually show the behavior of the output polarization states backscattered from different muscle groups at localized depth positions, we illustrate their trajectories on the Poincare sphere. The output polarization states scattered back from muscle group M_1 (at the depth segment indicated by the two-way red arrow in Fig. 3.3A) are shown in Fig. 3.3G where the trajectory of the output polarization states is constrained within a plane determined by the optic axis A_1 as expected. By using a sliding window with 5 adjacent output polarization states to do the plane fitting, the axes of the fitted plane are obtained as indicated by the black axes. These normal vectors represent the axes A_1 of the muscle M_1. The slight deviation of the optic axes is the result of the slight local heterogeneous property as expected from the tissue sample. Note also that these optic axes lie in the 3D space at the Poincaré sphere, demonstrating that the vertical component is retained.

Figure 3.3H shows the output polarization states scattered back from muscle group $M_1{}'$ (at the depth segment indicated by the red arrow in Fig. 3.3A). Affected by the upper muscle M_2, the normal vector $A_1{}'$ (indicated by the red axes in Fig. 3.3H) deviates from the true local axis A_1. By applying Eq. 3.2 to $A_1{}'$, the true local optic axes of $M_1{}'$ are obtained as shown in the black axes in Fig. 3.3H, which are consistent with the local axes of M_1 in Fig. 3.3G. In Fig. 3.3I, the trajectory of the output polarization states and the local axes of M_1 (black points and black axes) and M_2 (blue points and blue axes) at the depth segments indicated by red arrows in Fig. 4A are presented together. The blue flat plane is the fitted plane of the intermediate optic axes, showing that it is rotated off the QU-plane due to the use of the fiber-based PSOCT system.

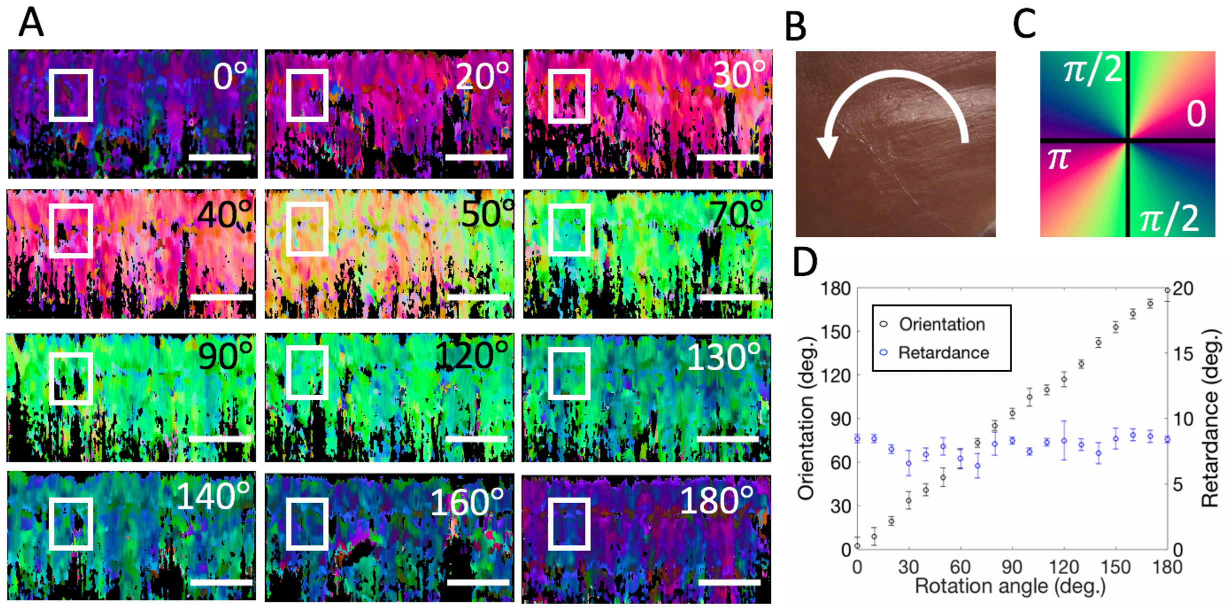

Figure 3.4 PSOCT imaging of a muscle with a homogenous optic axis rotated from 0 to 180 deg. A) Local orientation images of the same mouse muscle tissue rotated from 0° to 180° with the rotating angle as shown. B) The photography of the sample and an illustration of the sample rotation. C) Colormap used to color-code the orientation image. D) The scatter plots of the local phase retardation and local axis as a function of the rotation angle (from 0° to 180° with a step of 10°). The mean and standard deviation are shown calculated from the region of interest (ROI) marked in the white box in A. The white scale bar is 1 mm.

To demonstrate that PST method can extract the relative orientation of the sample, another tissue sample with relatively homogeneous birefringent property was used. The sample was consecutively imaged by the PSOCT system while it was mechanically rotated from 0° to 180° with an increment of ~10° step. The results are shown in Fig. 3.4 with photography of the sample shown together in Fig. 3.4B. The 0 deg was defined as the position when muscle orientation was in parallel to the B-scan direction. Fig. 3.4A shows the representative cross-sectional local optic axis maps of the tissue sample acquired at different angles as shown, where the images of the local axis are relatively uniform at each rotation angle but appear in different colors. Note that vertical structures are presented as artifacts in the cross-sectional images. These artifacts are introduced when computing the local axis orientation layer by layer, which means that the bias of axis orientation of the surface layer can propagate and accumulate over depth. The changing trend of the color when the sample was rotated from 0° to 180° is consistent with the colormap in Fig. 3.4C, demonstrating that the calculated local axis can retrieve the relative sample orientation. The mean and standard deviation values of the local phase retardation and optic axis in the region enclosed by the white box in Fig. 3.4A were calculated and the curves of these values as a function of the rotation degree are plotted in Fig. 3.4D. In Fig. 3.4D, the mean local phase retardation values keep relatively constant at different rotation angles, whereas the orientation value increases linearly as the rotation angle increases, showing that the calculated local axis provides correctly the relative orientation of the sample.

3.4 DISCUSSION

While we have demonstrated that the PST method can be used to extract the local optic axis and local phase retardance, there are some limitations of this geometric-based method. First of all, at least three depth measurements are required in the algorithm to fit a plane at the Poincare sphere. This requirement translates to a limitation of minimal mapping resolution of the local optic axis and phase retardance, which equals to a thickness of three-sampling pixels in the OCT depth imaging. For example, if the OCT axial pixel-resolution is 5 μm, then the minimal resolution of local birefringent mapping for our proposed method is 15 μm. Therefore, one way to improve the resolution of the proposed method is to increase the OCT imaging resolution, which is feasible in the current OCT development, but at the expense of cost.

The 2nd issue is when dealing with the transition from one layer to another layer with a distinct difference in optic axis. Under this circumstance, the fitted plane of this interface region would bear larger errors since the output polarization states at the interface regions would not be constrained to one plane at the Poincare sphere. This results in an error in the determination of the local optic axis and phase retardance at the boundaries of the components within the sample. Again, the improvement of the OCT axial resolution capability may mitigate this issue somehow. Or a new solution to this issue needs to be sought if the birefringent information at the close vicinity of optical interfaces within sample is critical for the study.

Finally, the proposed method is time-consuming since a sliding window is needed to do the local plane fitting progressively along with the depth. That is, the local apparent axis and the local phase retardation at each depth are computed discretely using a loop rather than be computed simultaneously along with a whole depth. In the next chapter, a novel method utilizing discrete differential geometry (DDG) will be presented to mitigate this issue.

3.5 CONCLUSION

We have proposed and experimentally demonstrated a PST method that utilizes the trajectory of the polarization states on the Poincaré sphere to derive the local birefringent information by using PSOCT. This method is compatible with the fiber-based PSOCT system with a single incident polarization state. We have described the theoretical framework to derive the local optic axis and phase retardation and experimentally demonstrated the proposed method by imaging a mouse thigh tissue sample in vitro.

Chapter 4. POLARIZATION SENSITIVE OPTICAL COHERENCE TOMOGRAPHY WITH SINGLE INPUT FOR IMAGING DEPTH-RESOLVED COLLAGEN ORGANIZATIONS

4.1 BACKGROUND AND MOTIVATION

Collagen, often organized in the form of fibers, is a structural protein widely distributed in biological tissue [73]. Its organization plays an important role in biomechanical structure and function. For example, the alignment of dermal collagen contributes to anisotropic tensile strength in human skin tissue (related to Relaxed Skin Tension Lines (RSTLs)) which provides both protection and tailored flexibility [74, 75]. Collagen organization also reveals important physiologic functions in tissue such as the heart, where its organization contributes to unique contractile muscular behavior [76, 77]. In cases where collagen networks have been disrupted, such as after myocardial infarction, the subsequent functional decline has been documented [76, 77]. Such examples suggest that insights into biological and pathological structure-function relationships may be elucidated, and even used to drive clinical intervention, based on depth-resolved identification of collagen fiber organization.

While techniques, such as polarized light microscopy, have been utilized to image collagen fibers in an ex vivo setting, many require tissue sectioning procedures [78, 79]. To achieve in vivo collagen imaging, techniques such as second harmonic generation (SHG) confocal-type microscopy have been developed to visualize and analyze depth-resolved collagen organization [80-82]. However, the field of view (FOV) (up to ~500×500 μm^2) and imaging depth (up to ~200 μm) are often too limited to reconstruct macroscopic collagen organizations that reveal the functional architecture of the tissue. Clearly, a technique capable of wide-field three-dimensional (3D) imaging of collagen structures in living tissue would provide rich information on how collagen organization relates to physiologic function.

As mentioned above, PSOCT [21, 67, 83-86] is a promising technique that enables the non-invasive 3D mapping of birefringent material. Since fibrous collagen is highly birefringent, PSOCT can contrast collagen structure with a wide FOV (from a few to tens of square centimeters), relatively deep imaging depth (up to ~2 mm) and fast imaging speed (seconds per 3D scan) [22, 55, 57, 68]. However, traditional PSOCT provides only accumulated polarization information along with depth due to back-scattered light which must pass through tissue twice before detection. Such accumulation can make it difficult to interpret the birefringent properties of the sample.

As mentioned in Chapter 3, Jones matrix calculus requires two distinct input polarization states to derive the depth-resolved axis orientation in 3D Stokes space. However, this requirement significantly complexes the system setup. For depth-resolved birefringent imaging, we proposed a method based on plane fitting to compute the 3D local axis orientation and local phase retardation of the sample with a single input polarization state in Chapter 3. However, the proposed method is time-consuming since a sliding window is needed to do the local plane fitting progressively along with the depth. That is, the local apparent axis and the local phase retardation at each depth are computed discretely. Moreover, because a plane has a pair of normal vectors that correspond to the direction of the fast and slow axes (right-hand rule determine the fast axis while left-hand rule determine the slow axis), an additional step to uniform the optic axis during computation is needed. Discrete differential geometry (DDG), a mathematical discipline that studies the geometry of spatial curves, can find the local apparent axis as the binormal vector and the local phase retardation at each depth along an A-scan simultaneously. Moreover, because the DDG calculus follows the right-handed rule, there is no need to apply an additional step to uniform the fast/slow optic axis during the computation process.

In this chapter, we utilize the DDG method to describe the PSOCT-based polarization state transmission model that leverages the Poincare sphere to describe the evolving polarization state of an incident beam as it travels through a birefringent sample with depth-varying optic axes and phase retardation in a round-trip measurement. Based on this transmission model, we describe a novel method where the 3D local axis orientation in the Stokes space can be obtained with only one single input polarization state, giving depth-resolved collagen imaging with sufficient imaging quality. The technical challenges of resolving birefringent information (i.e., local phase retardation and 3D local axis orientation in the Stokes space) along with the depth with a single input polarization are addressed using a discrete differential geometry (DDG) based polarization state tracing (PST) method combined with a series of 3D rotation operations in the transmission model. Without the requirement of multiple input polarization states, this method can simplify the imaging system setup, being aimed for clinical translation.

Using this method, we demonstrate depth-resolved mapping of the birefringent properties (largely determined by collagen organization) in ex vivo rodent hearts and in healthy human skin, in vivo. For the ex vivo study, fiber disorganization is detected within an infarct rodent heart using the proposed depth-resolved collagen organization imaging method. For the in vivo study, we demonstrate depth-resolved collagen organization imaging in healthy human skin to reveal the facial skin tension lines.

4.2 MATERIAL AND METHODS

4.2.1 DDG-based PST method

In Stokes space, a linear polarization can be modeled as a 3D rotation, where the rotation axis represents the optic axis, and the amount of rotation is the degree of phase retardation [65]. That is, when a polarized light propagates through a multi-layered material with a constant optic axis (i.e. material with a constant optic axis but experiencing phase retardation), the evolutional trajectory of the polarization state of the light beam must form a spatial circular curve on the Poincaré sphere. The osculating plane of this circular curve is the rotation plane of the linear polarization. Once this osculating plane is determined, the rotation information, i.e., both the rotation axis representing the optic axis and the rotation angle representing the phase retardation, can be determined. Hence, determining the osculating plane of the curve formed by the evolutional trajectory of the polarization state is the key to derive the local optic axis and phase retardation of a multi-layered material.

One such method to determine the osculating plane is based on discrete-differential geometry (DDG). The DDG analysis computes a set of 'TNB' orthonormal bases in 3D space where T is the tangent vector, N is the normal vector and B is the binormal vector of the spatial curve which are then used to determine the osculating plane (i.e., the plane that T and N vectors lie) at each point of the curve [87]. Since PSOCT is based on a round-trip measurement, the measured osculating plane is the apparent plane defined by the accumulated polarization rather than the actual osculating plane.

To retrieve local birefringent information using DDG analysis, a PSOCT-based polarization state transmission model that describes the polarization state evolution in a round-trip measurement is proposed and described herein. This model reveals the relation between local birefringent parameters and the evolution behaviors of the output polarization state in PSOCT. Based on this relationship, the DDG-based PST method is combined with a set of 3D rotation operations to derive the local optic axis and phase retardation from the measurements.

In what follows, we show how the TNB vectors are determined using the DDG method on the trajectory of the output polarization states. Then, we show how we utilize the TNB vectors to derive the local optic axis and local phase retardation in the PSOCT-based polarization state transmission model, which reveals the relation between local birefringent parameters and the evolution behavior of the output polarization states in the PSOCT system.

In Poincare representation, the trajectory of the output polarization state can be considered as a discrete spatial curve by connecting a sequence of measured data points: $P_n(n = 1,2,3 \ldots)$, where P_n represents the vector of output polarization state as a function of discrete pixel locations, n , along with the depth. We refer to this discrete spatial curve as the polarization state curve. Hence, a sequence of the right-handed discrete frenet-frames can be defined and computed by the DDG method as [87]

$$K_n = \left(\overrightarrow{T_n}, \overrightarrow{N_n}, \overrightarrow{B_n}\right)\ k = 1,2,3 \ldots \tag{4.1}$$

where

$$\begin{aligned} \overrightarrow{T_n} &= \frac{\overrightarrow{P_{n+1}} - \overrightarrow{P_n}}{\left|\overrightarrow{P_{n+1}} - \overrightarrow{P_n}\right|}, \\ \overrightarrow{B_n} &= \frac{\overrightarrow{T_{n-1}} \times \overrightarrow{T_n}}{\left|\overrightarrow{T_{n-1}} \times \overrightarrow{T_n}\right|}, \\ \overrightarrow{N_n} &= \overrightarrow{B_n} \times \overrightarrow{T_n}, \end{aligned} \tag{4.2}$$

$\overrightarrow{T_n}$, $\overrightarrow{N_n}$ and $\overrightarrow{B_n}$ are the unit tangent, normal and binormal vectors, respectively. The osculating plane at each point is spanned by the corresponding T and N vectors. Since $\overrightarrow{B_n}$ is the cross-product between $\overrightarrow{T_n}$ and $\overrightarrow{N_n}$ (follows the right-hand rule), it is orthogonal to the osculating plane and thus includes information related to the optic axis [88]. Note that the osculating plane directly provided by the TNB vectors is the apparent osculating plane that not only carries information of the localized tissue but also includes the accumulated information of all layers on top of it.

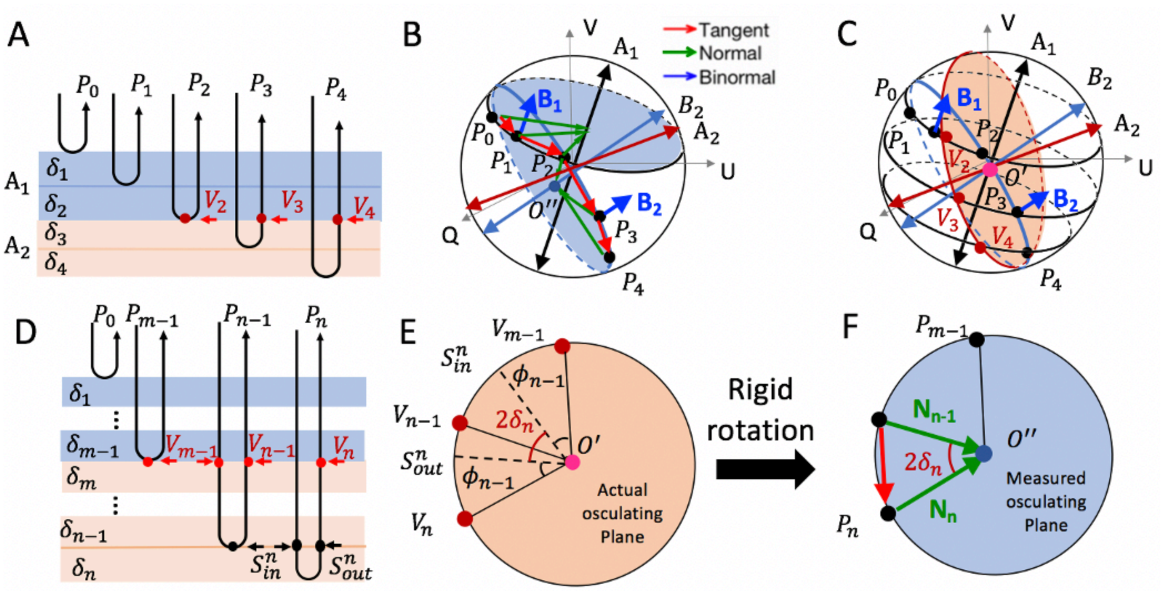

Figure 4.1 Schematic diagram of the PSOCT-based polarization state transmission model in a simulated birefringent sample with depth-varying optic axis, representing a A-scan in the imaging. P_0, P_1, P_2, P_3 and P_4, are the output polarization states that are detected by the PSOCT system. A) A depth scan of a simulated birefringent sample with depth-varying optics axis, where 4 birefringent layers are simulated with the first 2 layers sharing the same optic axis $\overrightarrow{A_1}$, and the last two layers sharing $\overrightarrow{A_2}$. V_2, V_3 and V_4 are the intermediate polarization state that are only influenced by the local birefringence. B) The trajectory curve of the output polarization states P_0, P_1, P_2, P_3 and P_4 on the Poincaré sphere with the corresponding TNB vectors. The measured osculating planes spanned by the T and N vectors are colored by blue. C) The geometric relation between the upper optic axes, $\overrightarrow{A_1}(i.e., \overrightarrow{B_1})$, the axis of the measured osculating plane $\overrightarrow{B_2}$ and the local optic axis $\overrightarrow{A_2}$. The actual osculating plane is colored by red. D) A depth scan of a simulated birefringent sample with depth-varying optic axis. E) The actual osculating plane composed by the V_{m-1} to V_n. F) The measured osculating plane composed by P_{m-1} to P_n. O' (pink points) and O'' (blue points) are the center of the actual and measured osculating planes, respectively. Red, green and blue arrows represent the tangent (T), normal (N) and binormal (B) vectors, respectively.

Next, we describe the PSOCT-based polarization state transmission model, with which the TNB vectors are combined with a set of 3D rotation operations to derive the local optic axis of a multi-layered sample with depth-varying optic axes. To illustrate this model, the polarization states of a light beam traveling through a representative birefringent sample is schematically shown in Fig. 4.1. To simplify, a simulated sample is used with two groups of birefringent material with different optic axes ($\overrightarrow{A_1}$ and $\overrightarrow{A_2}$), respectively (Fig. 4.1A). The first group consists of two retarder layers (blue layer) sharing the optic axis of $\overrightarrow{A_1}$, whereas the 2nd group also consists of two retarder layers (yellow layer) sharing the optic axis of $\overrightarrow{A_2}$. When the light beam propagates within this sample, each of the five interfaces back-scatter the incoming light toward the PSOCT detector to form an A-scan and the corresponding output polarization states are P_0, P_1, P_2, P_3 and P_4, respectively. The trace of the output polarization state from P_0 to P_4 forms a discrete curve on the Poincare sphere surface. DDG computation is then applied to this polarization state curve to determine the

TNB vectors (red, green and blue vectors represent T, N and B vectors respectively), as shown in Fig. 1B.

Specifically, for light beams scattered back from the sample surface and the first two blue layers, the output polarization states P_0, P_1 and P_2 are represented by the black points on the Poincaré sphere (Fig. 4.1B). Since the first two layers share the same optic axis $\overrightarrow{A_1}$, the polarization state curve of P_0, P_1 and P_2 on the Poincare sphere must follow a circular curve whose osculating plane is the rotation plane. For these two surface layers, the binormal vector $\overrightarrow{B_1}$ (which is orthogonal to the osculation plane) is equal to the optic axis $\overrightarrow{A_1}$ based on the linear polarization rotation model mentioned above:

$$\overrightarrow{A_1} = \overrightarrow{B_1} \tag{4.3}$$

For output polarization states scattered back from deeper layers with a different optic axis, the corresponding binormal vectors no longer represent the local optic axes. Instead, there is a 3D rotation between the binormal vectors and the exact optic axes in the specific layer of interest. This is why the differential geometry method alone can only determine the optic axis in a homogeneous sample rather than an inhomogeneous sample with varying optic axes (such as the mesh-like collagen fibers in the dermis and the myocardial collagen fibers) [89, 90].

Here, we discuss in detail the 3D rotation relationship among the optic axes, the binormal vectors of the polarization state curve, and the local optic axis of interest, which is required to derive the local optic axis progressively from superficial to deep tissue locations. Figure 4.1C illustrates the geometric relationship among the upper optic axes by highlighting the transmission process of the polarization states in the sample. On the Poincare sphere, the black points represent measured output polarization states P_0, P_1, P_2, P_3 and P_4 while the red points V_2, V_3 and V_4 represent the intermediate polarization states of light when they pass through the interfaces (Fig. 4.1A). These intermediate states are chosen to be shown because the change in the polarization state from V_2 to V_3 and V_2 to V_4 is only determined by the yellow layers (Fig. 4.1A), representing the information of the region of interest (ROI) in the tissue without accumulation effect. Hence, the trajectory of these three points must follow along another circular curve on the Poincare sphere, whose binormal vector is equal to the optic axis $\overrightarrow{A_2}$ of the yellow layers. We call the osculating plane of this curve (determined by V_2, V_3 and V_4) the actual osculating plane. Although the trajectory of V_2, V_3 and V_4 includes pure information of the local axis of ROI, they are the intermediate states which cannot be detected directly due to the round-trip measurement of PSOCT. Instead, they are each modified when light passes through the upper blue layers again to form the resultant output polarization states P_2, P_3 and P_4.

These modifications induced by the double-passage of the backscattered light are the same for all intermediate polarization states (i.e., V_2 to P_2, V_3 to P_3, V_4 to P_4) and can be viewed as a 3D rotation in the Poincare representation because they pass through the same upper blue layers as shown in Fig. 4.1A. That is, the actual osculating plane of V_2, V_3 and V_4 experiences a 3D rigid rotation about the axis of the upper layers A_1 (by an angle $\delta = \delta_1 + \delta_2$, where δ_1 and δ_2 are the local phase retardation of the first two layers) to form the measured osculating plane of P_2, P_3 and P_4, whose binormal vector $\overrightarrow{B_2}$ can be directly obtained using the DDG method as shown in Fig. 4.1B. Hence, the local optic axis $\overrightarrow{A_2}$ of the yellow layers can be obtained by rotating the binormal vector $\overrightarrow{B_2}$ about $\overrightarrow{B_1}$ by -δ as shown in Fig. 4.1C. This geometric relationship can be expressed as a matrix rotation:

$$\overrightarrow{A_2} = \boldsymbol{R_1}(-\delta;\ \overrightarrow{A_1})\vec{B}_2 \qquad (4.4)$$

where $\overrightarrow{A_1}$, $\overrightarrow{A_2}$ and $\overrightarrow{B_2}$ are the 1×3 matrices represented by the corresponding Q, U and V values; $\boldsymbol{R_1}(-\delta;\ \overrightarrow{A_1})$ is the 3D rotation matrix determined by $\overrightarrow{A_1}$ and $-\delta$.

Equation 4.4 can be generalized for the sample with multiple varied optic axes along depth. The actual osculating plane in the layer of interest would experience a set of 3D rotations when the light beam passes through all upper layers again (due to double-passage). Each upper layer would rotate the actual osculating plane once with the rotation matrix determined by the corresponding layer's local optic axis and local phase retardation. Since the normal vector of the actual osculating plane is the local optic axis of the layer of interest, it also experiences the same set of rotation to form the binormal vector $\overrightarrow{B_n}$, which is orthogonal to the measured osculating plane and can be computed by the DDG method directly. Hence, the final local optic axis $\overrightarrow{A_n}$ can be obtained by applying a set of 3D rotation operations to the binormal vector $\overrightarrow{B_n}$:

$$\overrightarrow{A_n} = \boldsymbol{R}_{\mathbf{n-1}}\left(-\delta_{n-1};\ \overrightarrow{A_{n-1}}\right)\boldsymbol{R}_{\mathbf{n-2}}\left(-\delta_{n-2};\ \overrightarrow{A_{n-2}}\right) \ldots \boldsymbol{R}_{\mathbf{1}}\left(-\delta_1;\ \overrightarrow{A_1}\right)\vec{B}_n. \tag{4.5}$$

From this equation, the local optic axis can be derived layer by layer using the TNB vectors of the polarization state curve and the 3D rotation matrix of each upper layer.

Finally, we describe how to use the TNB vectors to compute the local phase retardation. Fig. 4.1E shows the actual osculating plane of the n-th layer in Fig. 4.1D. In this plane, the local phase retardation δ_n is half the angle that rotates the local input polarization state S_n^{in} about the local optic axis to the local output polarization S_n^{out}. That is, $\delta_n = \frac{1}{2}\angle S_n^{in} O' S_n^{out}$. Consider the round-trip measurement, $\phi_{n-1} = \sum_{i=m}^{i=n-1} \delta_i = \angle V_{m-1} O' S_n^{in} = \angle S_n^{in} O' V_{n-1} = \angle S_n^{out} O' V_n$, hence, $\delta_n = \frac{1}{2}\angle S_n^{in} O' S_n^{out} = \frac{1}{2}\angle V_{n-1} O' V_n$. As mentioned above, there is a rigid rotation of the actual osculating plane to form the measured osculating plane ($P_{m-1} \ldots P_{n-1} P_n$) when the light passes through all the upper layers once again. Then we can get $\delta_n = \frac{1}{2}\angle V_{n-1} O' V_n = \frac{1}{2}\angle P_{n-1} O'' P_n$, which is half the angle between the adjacent T vectors as shown in Fig. 4.1F. Thus, the local phase retardation can be expressed as

$$\delta_n = \frac{1}{2} arccos \frac{\overrightarrow{N_{n-1}} \cdot \overrightarrow{N_n}}{|\overrightarrow{N_{n-1}}||\overrightarrow{N_n}|}. \tag{4.6}$$

Equations 4.5 and 4.6 show that based on the PSOCT-based polarization state transmission model, the local axis orientation and local phase retardation can be derived using a DDG-based PST method combined with a set of 3D rotation using only one single polarization state.

4.2.2 Generalized single input PSOCT system and signal processing

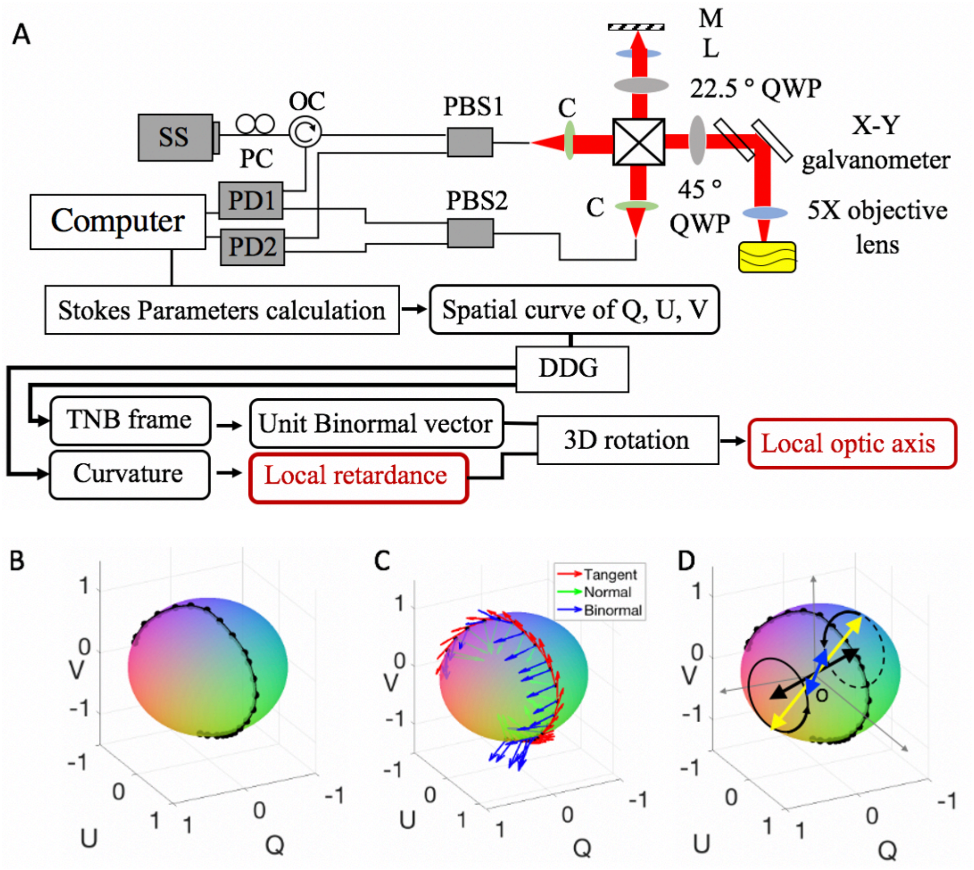

Figure 4.2 Schematic of the PSOCT system. A. PSOCT system setup. SS: swept source; PC: polarization controller; OC: single mode optical circulator; PBS: polarization beam splitter; QWP: quarter wave plate; PD: photo detector. Below the system schematic is a data processing flow chart of the DDG-based PST method; B. Spatial curve of the output polarization states in a PSOCT A-scan captured from the birefringence phantoms; C. The moving frenet-frame (TNB-frame) of the spatial curve by using the DDG analysis; D. 3D rotation to obtain the depth-resolved optic axis.

A schematic of the generalized single input PSOCT system is shown in Fig. 4.2. The system used a 100-kHz MEMS-VCSEL swept laser source (SL1310V1-20048, Thorlabs), providing an output power of 25 mW with a central wavelength of 1310 nm and a spectral tuning range of 100 nm. The output of the light source was sent to a polarization controller and became linearly polarized through a polarization beam splitter (PBS 1), and then split into the reference and sample arms through a beam splitter at a split-ratio of 50:50. The reference arm was installed with a quarter-wave plate (QWP) with its axis aligned at 22.5° with reference to the input polarization state, ensuring that the reflected light was coupled equally into the vertical and horizontal channels. The sample arm was equipped with a QWP aligned at 45° with respect to the input polarization state, resulting in a circularly polarized light incident at the sample surface. The light coming back from both the reference and sample arms were recombined and sent to PBS1 and PBS2, respectively, where the interference light was split into horizontal (Channel 1: PD1) and vertical (Channel 2: PD2) components. Balanced detection was used for both vertical and horizontal channels to collect the interference signals, upon which PSOCT images are reconstructed. The PSOCT system was controlled using a home-developed LabView (National Instruments) platform which provided flexibility to control scanning patterns based on the application (see Supplementary Section S2-5). The axial resolution was approximately 7.5 μm, in air.

The flow chart below the system schematic in Fig.4.2A illustrates the processing procedures of the DDG-based PST method to derive local phase retardation and optic axis from the PSOCT measurements. The output polarization states represented by Q, U and V were reconstructed by the Stokes parameters calculation [83]. Note that the magnitude of the output polarization state can be decreased by the depolarization [91], making the output polarization states no longer lie at the surface of the Poincare sphere in the Stokes space. To ignore the effect of the depolarization, all the Stokes vectors of the output polarization states were normalized to 1 before calculating the local phase retardation and local axis orientation. The trajectory of the output polarization states in an A-scan at the Poincare sphere is considered as a spatial curve as shown in Fig. 4.2B. DDG is applied to this curve to provide the TNB frame of the curve in an A-scan as shown in Fig. 4.2C. In Fig. 4.2C, a set of unit tangent vectors $T(n)$, unit normal vectors $N(n)$ and unit binormal vectors $B(n)$ of the curve are presented with red, green and blue arrows respectively. Figure 4.2D show the 3D geometric relation between the upper optic axes (black arrow), the axis of the measured osculating plane (blue arrow) and the local optic axis (yellow). By using a 3D rotation operation, then the local phase retardations and local axis orientation can be obtained by Eq. 4.5 and Eq. 4.6, respectively. To reduce noise, spatial averaging filter (4 × 4 pixels, x × y) was applied to the en-face and the cross-sectional (x × z) optic axis orientation images.

Because the asymmetry of the optical path in the PSOCT system can cause an overall rotation of the plane that contains all possible optic axes, the vector *An* is a vector in 3D space [3]. After the 3D vector *An* is computed, the effect of the asymmetry of the system can be identified as the V-components of all the 3D vectors *An*. Since the vertical (along z, or equivalently V on the Poincare sphere) component of the vector *An* is introduced by the imaging system and not sensitive to tissue structures, it should be removed. As such, the direction of the vector projected onto the QU-plane represents the relative axis orientation of the sample. To obtain the absolute axis orientation of the sample, we calibrate the system by using a phantom with a known optic axis, and then define this axis as the reference direction (0°). RGB colors are utilized to code the local axis orientation for display. The projected vector is normalized to a unit vector. Red and green are utilized to code the x and y components of the unit vector that represent the optic axis. Because the V-component of An is introduced by the system, the color blue (representing the z component of the vectors) is manually set to 0.

4.2.3 Mouse heart imaging

The myocardial fibers of the whole heart are organized in a helical-like structure to enable its blood pumping capability [3]. Visualizing this exquisite helical-like myocardial architecture of the whole heart is a basic step to investigate the biomechanical dynamic process of the heart beating, which is one of the key parts to elucidate the physiologic cardiac function. To map the myocardial fiber organization of a whole heart, a fresh heart was extracted from a euthanized mouse (2 months old, male) and placed under the PSOCT system within 1 hour. All experimental procedures in this study were approved by the Institutional Animal Care and Use Committee (IACUC) of the University of Washington and conducted in accordance with the ARRIVE guidelines. The telecentric scanning lens objective lens LSM03 (Thorlabs Inc, USA) was used to provide a FOV of 8 mm x 8 mm with 500 x 500 pixels. The total imaging time is 3.3 s. The excised whole mouse heart was mounted on a rotational stage using a thin needle. The mouse heart was mechanically rotated from 0° to 360° with an increment of ~30° step for whole heart imaging. A single-plane en-face image (50 µm below the surface) was used to display macro-level local optical axis.

4.2.4 Healthy and infarcted rat heart imaging

Male Sprague-Dawley rat (approximately 250-300 g, 8 weeks of age) were acquired for imaging of ex vivo heart tissue. All animal procedures were approved by the University of Washington Institutional Animal Care and Use Committee (IACUC, protocol #2225-04) and performed in accordance with US NIH Policy on Humane Care and Use of Laboratory Animals. To compare healthy and infarct myocardial tissue, one animal was randomly chosen as the healthy sample and another chosen to undergo a thoracotomy surgery for ischemia/reperfusion of the left anterior descending coronary artery to create a myocardial infarction.

For this surgery, rats were anesthetized with an intraperitoneal (IP) injection of 68.2 mg/kg ketamine and 4.4 mg/kg xylazine. A second dose of full-strength ketamine/xylazine followed by additional ketamine boosts (20 mg/kg, administered as needed) were used to maintain a surgical plane of anesthesia. During the procedure, the rats were intubated, mechanically ventilated, and maintained on a water-circulating head pad. Core body temperature was monitored at regular intervals and maintained at 37 °C. To induce myocardial infarction, the heart was exposed, and the left anterior descending coronary artery was ligated and occluded for 60 min, followed by reperfusion and aseptic chest closure. Sustained release buprenorphine (1 mg/kg) was administered following the surgery to provide analgesia for at least 2 days. Rats were closely monitored for 48 hours to provide post-operative care to ensure and maintain animal health and comfort as outlined in the IACUC protocol.

At 4 weeks post-infarct, rats were euthanized with a chemical overdose of pentobarbital/phenytoin solution (Beuthanasia; 1.5 mL IP injection). Once the animals achieved deep anesthesia while the heart was still beating, the chest was opened, and 50 U Heparin was intravenously infused via the inferior vena cava and allowed to circulate for 1–2 min to prevent thrombosis in the coronary vessels. Intravenous infusion with supersaturated potassium chloride (KCl) was then used to arrest the heart in diastole followed immediately with excision of the heart. The aorta was cannulated followed by retrograde perfusion with a vasodilator buffer (PBS containing 4 mg/L Papaverin and 1 g/L adenosine) followed by 4% paraformaldehyde perfusion for 10 min. Perfusion pressure was maintained at ~100 mm Hg. After perfusion fixation, the hearts were transferred to fresh fixative overnight at 4 °C. After overnight fixation, the cannulated hearts were transferred to PBS buffer and then transferred on ice for PSOCT imaging. The NA (numerical aperture) objective lens LSM03 (Thorlabs Inc, USA) was used to provide a FOV of 6 mm x 6 mm with 500 x 500 pixels. The total imaging time is 3.3 s. Note that as the fixation can alter local stiffness of the heart tissue, the birefringence of the fixed heart, which is related to the mechanical property of heart tissue, should be higher than that of the fresh heart.

Following PSOCT imaging, the rat hearts were sliced into 2 mm-thick sections from the apex for paraffin processing and embedding [5, 6]. 4 μm sections were cut and stained for picrosirius red/fast green to visualize the collagenous/infarcted regions in red and healthy tissue in green.

4.2.5 Human facial skin measurement protocol

Multiple anatomical locations were imaged on the selected regions of facial skin in a healthy volunteer (29 years, female, Asian). The use of OCT to image body skin was approved by the University of Washington institutional review board (IRB00000889). Informed consent was obtained from the volunteer. The selected regions of interest were typical regions in the aesthetic units: c. glabella, d. lateral eyelid, e. cheek f. inferior eyelid and g. skin around the upper lip as shown in Fig. 4.7A. The Relaxed Skin Tension Lines (RSTLs) [92, 93] of these regions were estimated and displayed on the photograph for reference [74, 94]. Two OCT scanning patterns were used for imaging: high-lateral resolution scanning (11 μm) with a field of view (FOV) of 2 mm x 2 mm, and relatively low-lateral resolution scanning (22 μm) with a FOV of 6 mm x 6 mm. For each scanning pattern, the OCT beam sampling density was 500 x 500 pixels, i.e. the fast B-scan axis consists of 500 A-scans and the slow axis consists of 500 B-scans. The total imaging time is 3.3 s. A single-plane en-face image (50 μm below the surface) was used to display local optical axis.

4.3 RESULTS

4.3.1 Validation of the DDG-based PST method with birefringence phantom

We conducted a custom-made birefringent phantom study to validate the proposed DDG-based PST method. The phantom was made of polylactic acid (PLA) 3D printer filament. The PLA exhibits intrinsic homogenous birefringence with its fast optic axis parallel to the filament's long axis. The phantom was consecutively imaged by the PSOCT system while it was mechanically rotated from 0° to 180° with an increment of ~10° step. The results are shown in Fig. 4.3 with a photograph of the sample shown together in Fig. 4.3A. The 0° was defined as the position when PLA long-axis orientation was parallel to the B-scan direction. Figure 4.3B shows the cross-sectional structure image of the phantom when it is 90° to the B-scan direction. Without the birefringent information, it's difficult to determine the axis orientation of the phantom in the structure image. Figure 4.3C shows the corresponding polarization state image, in which the accumulation effect is presented as multiple band-like patterns. In this case, the axis orientation of the phantom is still hard to be appreciated. Figure 4.3D shows the local axis orientation image of the sample by using the DDG-based PST method, in which the accumulation effect is removed, and the relatively homogenous depth-resolved axis orientation is retrieved. These results demonstrate that the DDG-based PST method has the ability to reconstruct the depth-resolved axis orientation image. Figure 4.3E shows cross-sectional local optic axis maps of the phantom sample acquired at different angles, where the images of local axis are relatively uniform at each rotation angle but demonstrate different colors according to the PLA long-axis orientation relative to the B-scan direction. The change trend of the color when the sample was rotated from 0° to 180° is consistent with the colormap in Fig. 4.3G, demonstrating that the calculated local axis can retrieve the relative sample orientation. The mean and standard deviation of the local optic axis orientation in the region enclosed by the white box in Fig. 4.3E were calculated and the curves of these values as a function of the rotation degree are plotted in Fig. 4.3F. In Fig. 4.3F, the orientation value increases linearly as the rotation angle increases, showing that the calculated local axis provides the relative orientation of the sample.

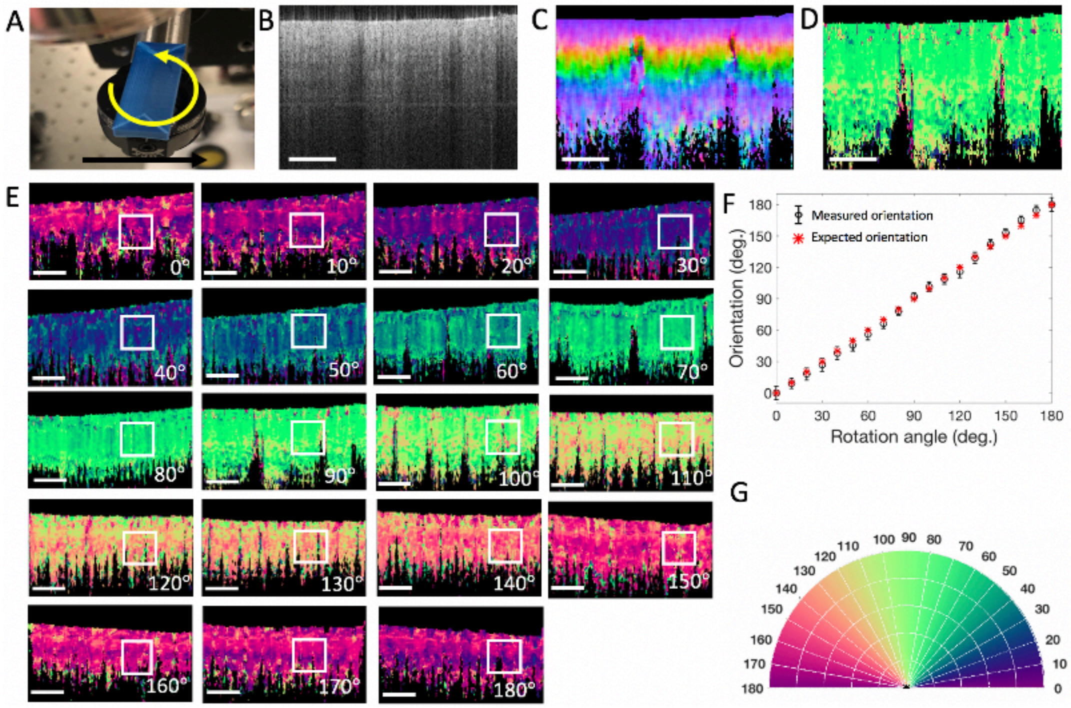

Figure 4.3 PSOCT imaging of a PLA filament with a homogenous optic axis rotated from 0° to 180° with a step size of 10°. (A) The photograph of the filament and an illustration of the sample rotation. The black arrow indicates the B-scan direction. (B) Cross-section structure images of the PLA filament. (C) Cross-section polarization state image of

the PLA filament, demonstrating the accumulation effect in PSOCT imaging. (D) Local axis orientation image of the filament in which the accumulation effect is removed. (E) Local orientation images of the filament rotated from 0° to 180° with the rotating angle as shown. (F) The scatter plots of the local axis as a function of the rotation angle (from 0° to 180° with a step of 10°). The standard deviations are shown calculated from the region of interest (ROI) marked in the white box in A. (G) Colormap used to color-code the orientation images in (D) and (E). The white scale bar is 1 mm.

We next tested the algorithm in a sample with depth-varying optic axis. A phantom specimen was constructed by stacking two pieces of PLA filaments at an angle as shown in Fig. 4.4C. The upper black sample was positioned at ~90 deg, and the lower piece was positioned at about 175 deg. In the structure OCT image (Fig. 4.4A), although two PLA filaments can be differentiated by the scattering signals, the orientation information of the sample is not apparent. Note that the surface of the lower filament is flat, but it appears not leveled in Fig. 4.4A: the surface of the region covered by the black filament is lower than the other region. This is because the refractive index of the black filament is stronger than the air, hence the corresponding optical path is longer, which makes the portion of blue filament covered by the top black filament appear deeper in the cross-sectional OCT image.

The local optical axis (Fig. 4.4B) in the two pieces of filaments appears relatively homogeneous with distinct differences in the axis values between them. Both the areas covered by the upper filament (R2 indicated by the black box in Fig. 4.4B) and the region directly exposed to the probing light (R1) have consistent orientation angles, demonstrating that the proposed method has the ability to derive the local axis orientation from a sample with depth-varying optic axis. 1. In the histogram image (Fig. 4.4D), the dominant orientations of the two filaments are evaluated at ~90° and ~170° respectively, consistent with the directions of the samples shown in Fig. 4.4C. This further demonstrates the algorithm’s ability to extract depth-resolved local axis orientation information.

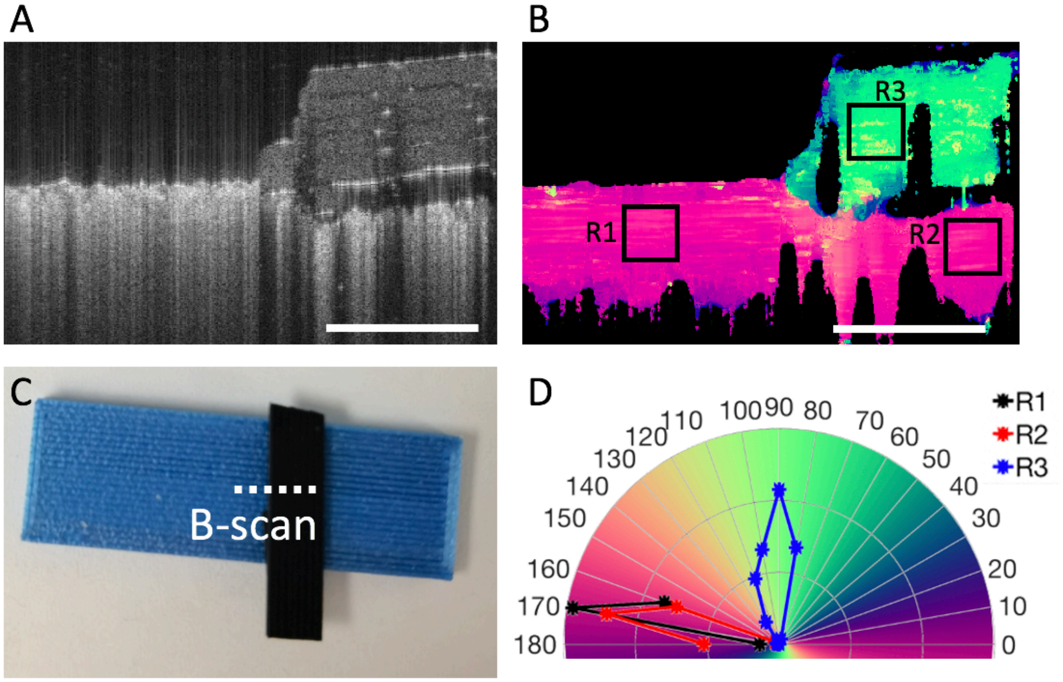

Figure 4.4 PSOCT imaging of two PLA filaments stacked at an angle (~90°). (A) Cross-sectional of the structure images of the two PLA filaments. (B) Local orientation images of the two PLA filaments. (C) The photograph of the filaments. White dash line indicates the direction of the B-scan. (D) The histogram distributions of orientation obtained from the regions: R1, R2 and R3 indicating by the black boxes in (B). The white scale bar is 1 mm.

Collagen Organization Imaging Using DDG-PST Method

Since fibrous collagen shows intrinsic optical anisotropy, axis orientation mapping can be utilized to extract the collagen organization from the tissue with high contrast and provide orientation information of collagen alignment [95-97]. Next, we demonstrate depth-resolved collagen organization imaging of several samples of importance using the proposed method. In all collagen orientation results below, we used the same colormap (Fig. 4.3G) to avoid possible confusion. The 0 deg is defined as the sample orientation when it is parallel to the B-scan direction (i.e., fast scanning direction).

4.3.2 Ex-vivo imaging of healthy mouse heart

To demonstrate the ability of the DDG-based PST method to visualize collagen organization, a whole mouse heart was imaged by the PSOCT system with within 1 hour of extraction. Figure 4.5 shows a 3D rendered PSOCT volume of the whole heart obtained from stitching separate en-face axis orientation images (50 μm below the heart surface) acquired at 12 perspective angles. In this image, streamlines obtained by the local axis orientation values are used to represent the fiber tracts and show the skeleton structures in spatial organization of fiber bundles. The result depicts the myocardial fiber organization of the superficial tissue of the whole mouse heart, where a typical helical-like myocardial fiber structure was reconstructed by the DDG-based PST method, demonstrating the ability of the proposed method to reconstruct myocardial fiber orientations.

Taking advantages of the wide FOV of the current PSOCT system, the relative fiber orientations among different parts of the heart were visualized in a macroscopic view. The myocardial fiber organization of left ventricle (LV) (Fig. 4.5A, 4.5B and 4.5D), right ventricle (RV) (Fig. 4.5A, 4.5C and 4.5D) and the two boundaries between the RV and LV: the anterior interventricular sulcus (AIVS) (white dash line in Fig. 4.5A) and the posterior interventricular sulcus (white dash line in PIVS) (Fig. 4.5D) are presented in an entirety in Fig. 4.5. The results show the potential for this technique to investigate microstructural foundations which may play a role in the interaction mechanisms between different cardiac tissues.

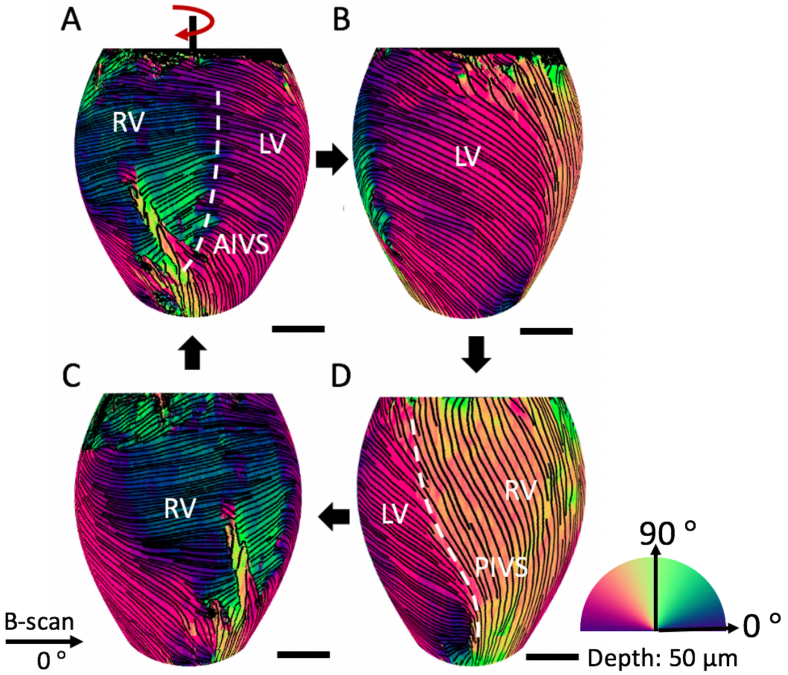

Figure 4.5 Orientation of the myocardial fiber of a whole mouse heart: with the proposed DDG-based PST method, single input PSOCT is capable of providing the orientation information of myocardial fiber within superficial ventricular wall of a whole mouse heart. Results shown are different perspective views of a reconstructed 3D optic axis orientation map at 50 μm below the heart surface of a whole heart (Supplementary Section S3). (A) The front view; (B) The right-side view to show left ventricle; (C) The left-side view to show right ventricle; (D) The back view of the 3D volume-rendered myocardial fiber organizations in the whole heart. The colormap is shown in the lower right corner. The streamlines on the heart represent the orientation of the myofibers. In the lower left corner, the black arrow indicates the B-scan direction, which is defined as the 0°. The scale bar = 1 mm. RV – right ventricle, LV – left ventricle, AIVS – anterior interventricular sulcus, and PIVS – posterior interventricular sulcus.

4.3.3 Ex-vivo imaging of infarcted rat heart

Herein we demonstrate the ability of the DDG-based PST method to image collagen orientation and organization in both healthy cardiac tissue and in tissue 4 weeks following an induced infarct event. Briefly, one animal was randomly chosen as the healthy sample, and another chosen to undergo a thoracotomy surgery for ischemia/reperfusion of the left anterior descending coronary artery to create a myocardial infarction. Following euthanasia, the aortas of both samples were fixated using 4% paraformaldehyde perfusion prior to PSOCT imaging.

Linear gradient changes in the fiber orientation angle along depth was detected in the healthy heart (Fig. 4.6A, 4.6C and 4.6E), consistent with prior histology studies [98, 99]. In the en-face images (50 μm below the surface) (Fig. 4.6A) selected at different depths (from 140 μm to 840 μm relative to tissue surface), the myofiber orientations were highly uniform at each depth and rotated gradually: the mean axis orientation determined from each en-face slice was 159.7° (i.e., -20.3°) ±2.35°, 167.2° (i.e., -12.8°) ±2.30°, 4.19° (±2.49°), 11.7° (±3.45°) and 45.7° (±4.51°), respectively, with relative small standard deviations. This phenomenon is displayed using a polar histogram plot to visualize the dominant orientation direction and relative distribution of the optic axis at each depth (Fig. 4.6E). The preferential collagen distribution demonstrates myofibril uniformity and anticlockwise rotation of the dominant fibers along depth. Depth-resolved reconstruction shows the gradient change of the myofibril direction over depth, consistent with the prior histological observations [98, 99], demonstrating the usefulness of the proposed DDG-based PST method.

However, the infarcted heart exhibited disorganization of the myocardial fibers along the depth within the cardiac wall (Figs. 4.6B, 4.6D and 4.6F). In the en-face axis orientation images selected at different depths (Fig. 4.6B), myofibers in the superficial layer (140 μm relative to the tissue surface) appear uniform, which is similar to the healthy heart (e.g. Fig. 4.6A). With the increase of depth, the fiber orientations show random and discontinuous patterns in the infarcted tissue (Fig. 4.6B), indicating fibril damage due to the infarct occurred relatively deep within the cardiac wall. The cross-sectional image (Fig. 4.6D) shows that the collagen fiber disorder begins around 300 μm from the outer wall. Beneath this depth, a linear gradient change in fiber orientation is no longer observed, demonstrating remodeling of the fiber structure after infarction. The orientation distribution of the fibers at each depth in the infarct tissue is shown in the polar histogram (Fig.

4.6F), where except for the surface layer (140 µm), the distributions of the orientation in the infarct tissue are widely spread in the deeper layers. These results are consistent with histological staining (Fig. 4.6H), where the superficial tissue of the infarcted heart appears normal (similar to the tissue of the healthy heart (Fig. 4.6A)) while random fiber structures appear around 300 µm in depth.

Depth-resolved axis orientation images of healthy and infarcted rat hearts revealed complex myocardial fiber arrangements which differ along the depth of the cardiac wall. The depth-resolved ability of the DDG-based PST method detected physiologic change deep within the cardiac wall. Overall, rodent heart imaging in this work demonstrated that the method can be readily applied to laboratory studies, potentially providing an insight into the physiology and pathology of the biological tissue.

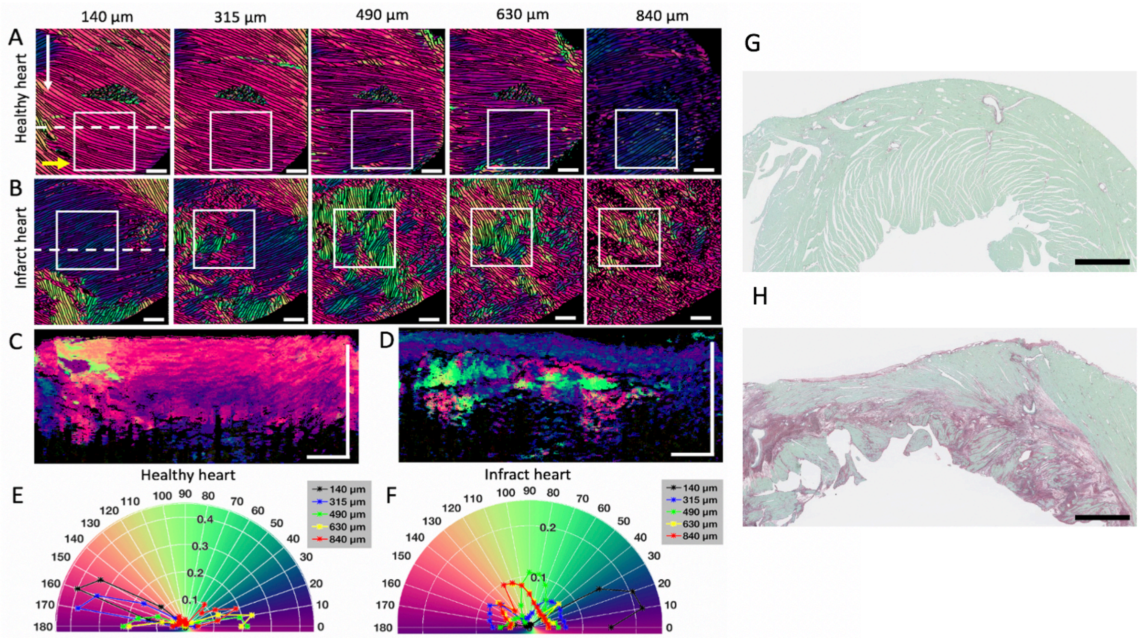

Figure 4.6 Orientation of the myocardial fibers in healthy and infarcted rat hearts: 2ith the proposed DDG-based PST method, single input PSOCT is capable of imaging the depth-resolved myofiber disorganization in infarct rat hearts. Results shown were obtained from healthy and infarcted hearts, respectively. The en-face local axis orientation (OAx) images of (A) the healthy rat heart (B) the infarct heart at different depths as shown from 140 µm to 840 µm. Cross-sectional axis orientation images of (C) the healthy rat heart (D) the infarct heart at the regions indicated by the white dash lines in (A) and (B). (E, F) The polar histogram distributions of orientation obtained from the white boxes in the healthy heart (A) and the infarct heart (B) at five depths relative to the tissue surface (140 µm, 315 µm, 490 µm, 630 µm and 840 µm), respectively. White arrow at the top left points to the apex. The yellow arrow indicates the B-scan direction, which is defined as the 0°. Note that a triangular black tape was used as the guide to align the system scanning during imaging, which appears as an artifact in the middle of images in (A). Histology staining slices of G) the healthy rat heart H) the infarcted rat heart. The slices are at approximately 6 mm from the apex. Slices are stained with picrosirius red/fast green. Collagenous/infarcted regions stain red, and healthy tissue stains green. The scale bar represents 1 mm. The scale bar = 1 mm.

4.3.4 In-vivo imaging of human skin

Relaxed skin tension lines (RSTLs), corresponding to the natural orientation of elastin and collagen fibers, are important for planning and placement of surgical incisions in facial reconstructive surgery and cosmetology. Because the relative angle between RSTLs and incisions plays a role in the formation of scars [74, 75], visualizing fiber orientation in human skin tissue may provide surgeons with additional information to both personalize surgical procedures and monitor long term outcomes. To demonstrate the potential of the DDG-based PST method in surgical applications, we imaged multiple anatomical locations (defined according to aesthetic units shown in Fig. 4.7A) on the face of a healthy adult volunteer (29 years, female, Asian). Two OCT scanning patterns were used for imaging: high-lateral resolution scanning (11 μm) with a field of view (FOV) of 2 mm x 2 mm, and relatively low-lateral resolution scanning (22 μm) with a FOV of 6 mm x 6 mm. RSTLs, defined as the direction of greatest tension on the skin and parallel with collagen bundles [92-94], were estimated and displayed on the photograph (Fig. 4.7A) for reference [74, 94].

Woven mesh-like structures formed by varied arrays of collagen bundles were observed in the en-face axis orientation images (Figs.4.7C-4.7G, produced by depth-averaging a 70μm thick slab with its anterior boundary at 100 μm beneath the skin surface) in each facial region, demonstrating that collagen organization of the skin can be extracted from living tissue using the proposed technique. In general, a single dominant color was found in the en-face image of each facial region, suggesting alignment of collagen fibers which can be measured and visualized using the DDG-based PST method. Polar histograms (Fig. 4.7H-K) which present orientation distribution in the en-face image at each depth show that the preferential direction of the collagen fibers is consistent with the general directions of RSTLs as shown in Fig. 4.7A. We note that the collagen orientation of glabella (Fig. 4.7G) is orthogonal to the direction of traditional RSTLs. While this may be a feature of the particular volunteer, there remains unanswered questions regarding the relationship between collagen fiber alignment and RSTLs.

These results demonstrate the potential for the DDG-based PST method to guide skin incision placement by visualization patient-specific RSTLs in vivo, further investigate collagen fiber orientation in normal and abnormal states of scar formation, and study collagen disorders of the skin such as Ehler's Danlos syndrome and Scleroderma [100, 101].

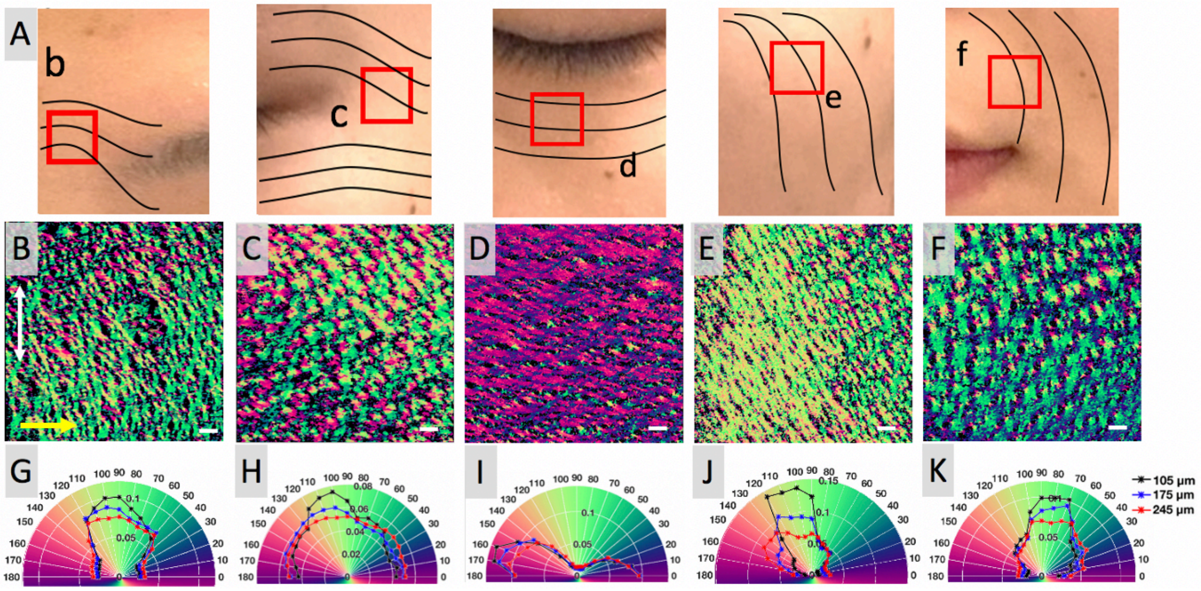

Figure 4.7 Collagen organization within healthy human skin: with the DDG-based PST method, PSOCT reveals macroscopic architecture of collagen organizations at various locations on the human facial skin. (A) Illustration of selected regions (marked as red squares, c-g) on the human facial skin for representative PSOCT imaging of the relaxed skin tension lines (RSTLs), where c-g respectively indicate the facial regions of glabella, lateral eyelid, inferior eyelid, cheek, and upper lip. (B-F), The en-face axis orientation (OAx) PSOCT images (generated by average projection of a 70 μm slab, starting from approximately 105–175 μm depth from the skin surface) acquired from the regions of (B) glabella; (C) Lateral eyelid; (D) Inferior eyelid; (E) cheek; (F) upper lip. (G-K), The corresponding histogram distributions of orientation obtained from the en-face OAx slices measured at (G) glabella; (H) lateral eyelid; (I) inferior eyelid; (J) eye bag; (K) upper lip, respectively, at three different depths (105 μm, 175 μm and 245 μm). White double-headed arrow in (B) shows the direction of the body axis. The yellow arrow indicates the B-scan direction, which is defined as the 0°. The scale bar = 500 μm.

The DDG-based PST method was also used to image depth-resolved features of in vivo facial collagen organization. Two scanning patterns are used to reveal networks of collagen bundles at different FOVs in the cheek across all depths (Fig. 4.8A and 4.8B). The mesh-like structure of collagen organization is clearly presented in the local axis orientation images while crossing networks are faintly perceivable in corresponding structural en-face images (obtained by OCT images). In the axis orientation images (Fig. 4.8A and 4.8B), the collagen fibers in the papillary layer (~105 μm) appear to form a loosened mesh but with an alignment whose orientation is matched with the RSTLs. Multiple arrays of collagen fibers with different orientations are found to form a tight meshwork in the reticular layer (~175 μm and 245 μm).

The polarization state image (Fig. 4.8D) was created using the output polarization states [83] where red, green and blue are used to code the Stokes parameters Q, U and V (respectively) corresponding to the output polarization state in backscattered light. Since the polarization state image reveals comprehensive information (i.e., combining both phase retardation and orientation) of the birefringent sample [83], it can visualize the birefringent component embedded within the tissue with high contrast. The top view of the 3D polarization state image of facial skin (cheek) is provided to visualize the architecture of the collagen fibers as shown in Fig. 4.8D, the colormap of which is the color-coded Poincare sphere in Fig. 4.2B-D. A mesh-like woven organization of the collagen fibers is clearly seen.

These results demonstrate the potential of the proposed method to investigate the depth-resolved 2D projection collagen structure in both macro and micro-scale, potentially connecting how collagen organization maintains the structural integrity of the skin.

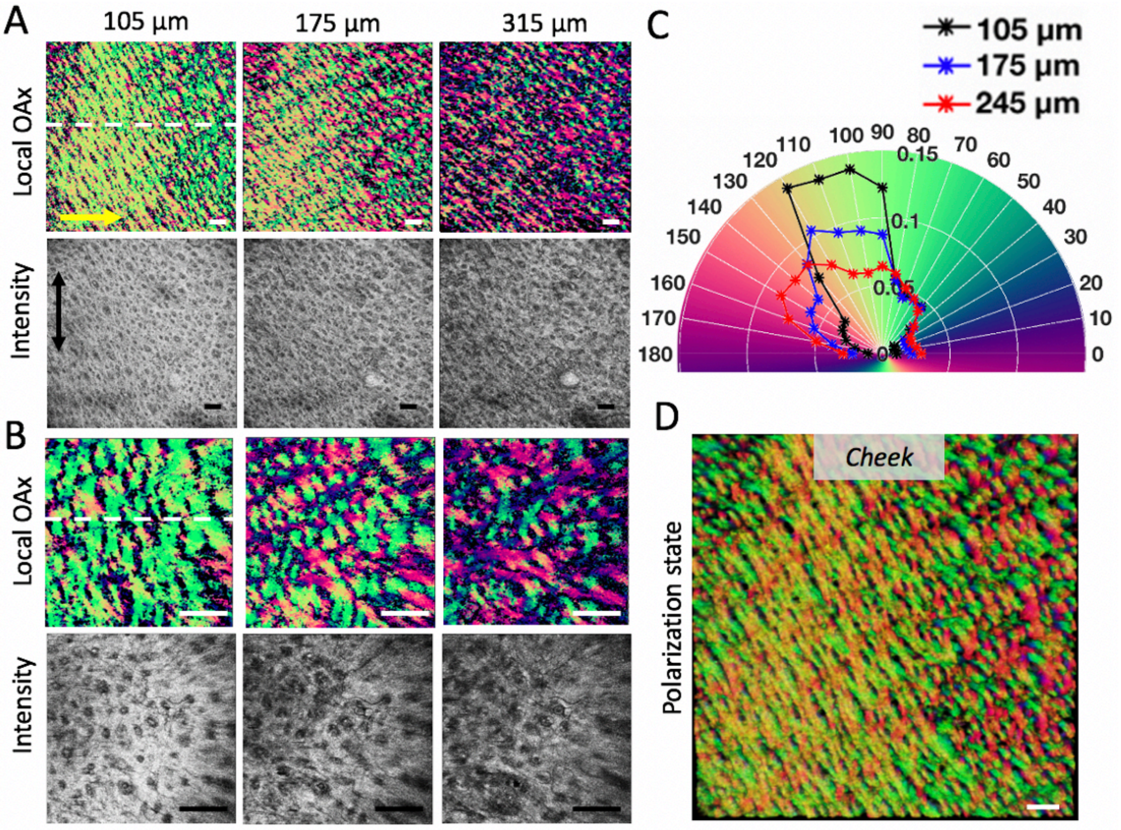

Figure 4.8 Depth-resolved collagen fiber orientations within facial skin are revealed by PSOCT images. Results shown are obtained from a selected region of cheek skin (marked as red square in Fig. 2A). (A,B) The en-face local optical axis orientation (OAx) images and the corresponding en-face OCT intensity images at three different depths (105 µm, 175 µm and 245 µm) using high and low lateral resolution scanning probe, respectively; Black double-headed arrow shows the direction of the body axis. (C) The histogram distributions of orientation obtained from the en-face OAx slices shown in (A) (105 µm, 175 µm and 245 µm, respectively). (D) 3D polarization state image. The scale bar = 500 µm. The yellow arrow indicates the B-scan direction, which is defined as the 0°.

4.4 DISCUSSION

Clinical translation of PSOCT for depth-resolved imaging of fiber orientations for in vivo imaging requires minimal system complexity, cost-effectiveness and flexibility. The DDG-based PST approach introduced here enables depth-resolved birefringent imaging that only requires one single input polarization state, allowing a generalizable single input PSOCT system setup. Differing from previous multiple input Jones matrix-based measurement [19, 69], the DDG-based PST approach analyzes the trajectory of the depth evolution of a single input polarization state in the Stokes space.

4.4.1 Advantage of measuring local axis orientation in 3D Stoke space

Due to the asymmetric property of the imaging system, the optic axis to be measured becomes a 3D vector in the Stokes space rather than a scalar constrained within the QU-plane [64]. Hence, computing the 3D local axis orientation in the Stokes space would provide a higher accuracy.

To show that it is necessary to obtain the local axis orientation in 3D Stokes space which can deliver better performance in the imaging, we performed a comparison study. In the comparison, we evaluated the performances delivered by the previous algorithm that derive the local optic axis in QU-plane [18] (Evaluation 1) and by our algorithm (Evaluation 2), respectively. We used the same data set acquired from the facial cheek skin in the evaluations. The Evaluation 1 assumes that the effect of the asymmetry of the system can be ignored, and the 2D measurement of the local axis orientation is sufficient to derive the local optic axis. Under this assumption, the measured local axis orientation is considered to be a scalar constrained within the QU-plane.

The Evaluation 2 assumes that the measured local axis orientation is a 3D vector due to the asymmetrical property of the system, which is proposed in our study. In this case, the 3D optic axis of each layer was computed and used to derive the local optic axis layer by layer until the maximum depth has reached as described in our method. Note that in the final step of our method, there is an operation that sets the V-component of all final local optic axes to zero. This operation is to eliminate the effect induced by the system asymmetry. Different from the Evaluation 1, this operation was only executed at the final step after all the computations of the 3D local optic axes have been completed in 3D space.

The null hypothesis here is that if the effect of asymmetry of the system can be ignored in the evaluation of the local optic axis, then the resulting optic axis delivered by the above two evaluations would be similar.

Figure 4.9 below shows the en-face local phase retardation and local axis orientation images resulted from the two processing methods, respectively. The enface images at two depths (175 μm and 315 μm) are selected to demonstrate the noise and error accumulation effect over depth. The first raw (Figs. 4.9A-D) show the results from the method 1 (based on the 2D measurement in Stokes space), whereas the second raw (Figs. 4.9E-H) show the results from the method 2 (based on the 3D model in the Stokes space described in our paper). By a quick eyeballing, the testing hypothesis as stated above fails. It is also clear that the results delivered by the 3D model have much higher contrast and signal to noise ratio, demonstrating the advantages of the use of the 3D model to derive the optic axis and phase retardation.

Specifically, in the local phase retardation results (Figs. 4.9A, 4.9C, 4.9E and 4.9G), depth-resolved collagen organization can be visualized by both the methods. However, part of the signals generated by the collagen (as indicated by the yellow arrows and boxes) are lost in the 2D model (Fig. 4.9A and 4.9C) but appear clearly in the results from our method (Fig. 4.9E and 4.9G). The low contrast and noisy appearance in the images of the 2D model are largely due to the errors introduced by the consideration of 2D scalar optic axis at each step of the evaluation (and this error accumulates and propagates to the next level when the optic axis and phase retardation are computed at the deeper depths). This observation demonstrates that ignoring the V-component of the measured optic axis can lead to non-negligible information loss.

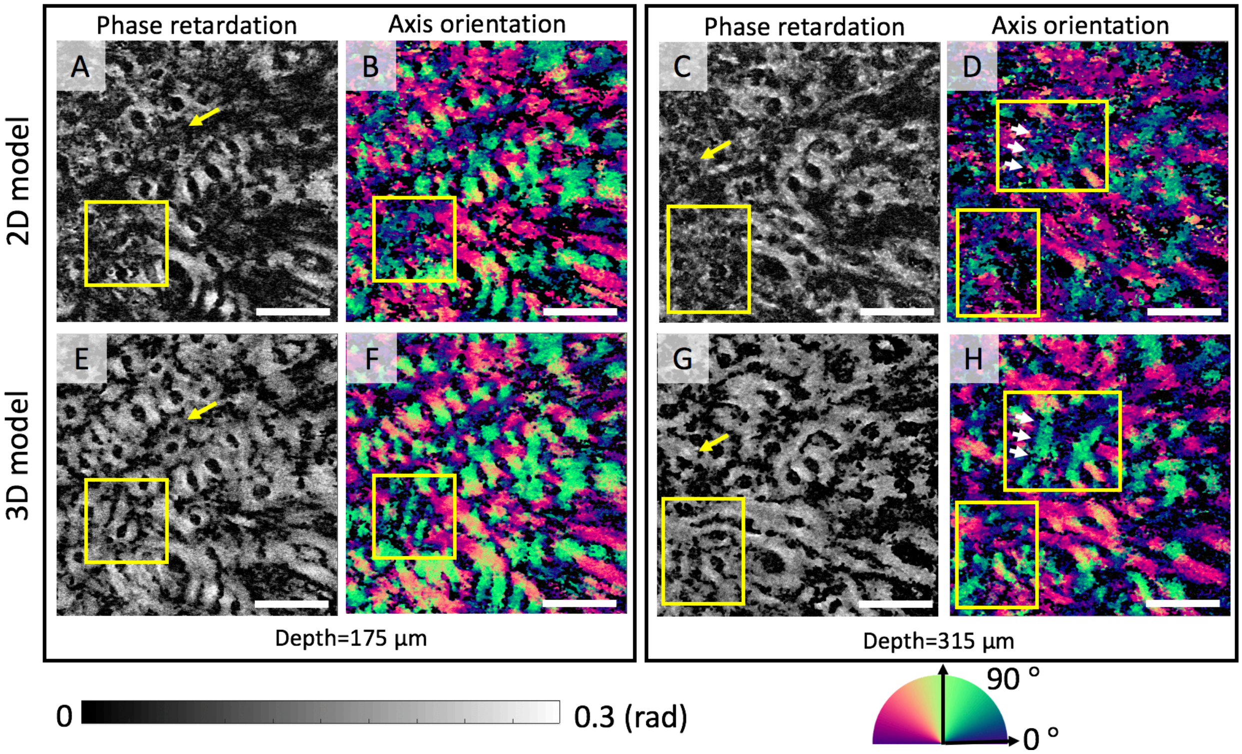

Figure 4.9 En-face local phase retardation and local axis orientation images resulted from the two Evaluations: i.e. 2D and 3D models, respectively. Results shown are obtained from a selected region of in-human facial cheek skin (marked as red square in Fig. 2A in the paper). (A-D) The en-face local phase retardation (A, C) and local axis orientation (B, D) images computed based on the 2D model. (E-H) The en-face local phase retardation (E, G) and local axis orientation (F, H) images computed based on the 3D model. (A, B, E and F) and (C, D, G and H) are the en-face images selected at 175 µm and 315 µm respectively. The scale bar = 500 µm. The color maps to display the phase retardation and optic axis images are shown at the bottom, respectively.

In the local axis orientation results selected at the depth of 175 microns (Fig. 4.9B and 4.9F), the orientation values of the collagen fiber bundles are relatively consistent with its corresponding morphologic direction in both groups of results, demonstrating that both computations can derive the local axis orientation of the sample. However, in the region with phase retardation information loss (as indicated by the yellow boxes), the orientation values of the collagen are inexplainable in Fig. 4.9B while the orientation values in Fig. 4.9F can clearly present the direction of the collagen, indicating that using the 3D model to compute the local axis orientation can provide a higher accuracy. The inaccurate measurement of the local axis orientation of the superficial layer will severely affect the computation of the local axis orientation in the deeper layer because the errors can propagate and accumulate over depth.

Because of accumulation effect, the impact of the dimension reduction on the final result would be more severe in the deeper depths. Figures 4.9D and 4.9H show the en-face local axis orientation images at 315 μm below the skin surface. The collagen organization can still be clearly differentiated in Fig. 4.9H with high contrast and SNR, whereas it is not in Fig. 4.9D. Moreover, the orientation values of a collagen bundle as indicated by the white arrows show an obvious difference in these two images: the mean orientation values of this collagen bundle are ~35° and ~73° in Fig. 4.9D and Fig. 4.9H, respectively. Referring to the morphologic direction of the collagen, the orientation value in Fig. 4.9H is more accurate than that in the Fig. 4.9D. These results demonstrate that the bias of the orientation induced by the dimension reduction will be accumulated over depth. Even the bias is small in the surface layer, it can still generate non-negligible effect to the measurement in the deeper layer.

In summary, it is necessary to compute the local axis orientation in 3D space due to the asymmetry property of the system. Note that in clinical translation, the system asymmetry property is environment dependent, therefore, we believe that our proposed method with a single input facilitates the clinical translation.

4.4.2 Advantage of DDG-based PST method over the method using two input polarization states

The advantage of the DDG-based PST approach over the previous methods that use two input polarization states is that without introducing the additional polarization modulation scheme [66, 70, 102], the requirement of known polarization states incident on the sample can be removed. This is because the DDG-based analysis of the trajectory of the polarization states is not affected by the location of the start point (i.e., the values of the input polarization state). Particularly, for any polarized light (excluding the one parallel to the optic axis of the sample) transmitting through the same region of the sample, its corresponding trajectories of the polarization evolution on the Poincare sphere should share the same set of binormal vectors, which determines the unique local birefringent parameters. This theoretical conclusion also provides a potential ability of the proposed method to simplify the configurations for other PSOCT systems, which is particularly attractive to the efforts that aim for clinical translation.

Another benefit of the proposed method is that it makes it compatible with most PSOCT system designs which utilize a single input polarization state, providing flexibility in system design. Previous studies have shown that different input polarization states have different sensitivities at particular values of optic axis or retardance [103]. Therefore, a general design with flexible selection of the input polarization state [103] is desirable for achieving the optimal sensitivity when imaging different birefringent samples.

4.4.3 Collagen organization imaging using PSOCT

In most cardiac tissue studies, histology remains the gold-standard method to evaluate myofiber architectures. However, this method is destructive and time consuming. The ability to reconstruct 3D collagen architecture from 2D stacks of histological sections is also challenging. Notably, rat heart imaging was performed following paraformaldehyde fixation which has been known to stiffen tissue based on the induction of collagen cross-links. However, the general helical-like arrangement of collagen tissue appeared to be retained in the healthy heart.

In this study, we note that a 22 μm lateral resolution may not be sufficient for detecting slight changes in collagen organization. Also, it is difficult to observe the dynamic of the myocardial fibers of the whole heart during heart beating because there is a time delay induced by the point scanning protocol when imaging different parts of heart. These two issues can be mitigated simultaneously by integrating the full-field microscopy into the PSOCT system. A high-resolution (~1 μm) 3D volumetric collagen organization image can be obtained with a single shot rather than point scanning. However, imaging depth would decrease in this case.

Overall, the depth-resolved PSOCT images of myofibers may be further used to monitor healing response to an infarct event at various times from injury, or in remodeling of grafts in heart, for example. The understanding of these matrices and remodeling could help understanding many important physiological diseases, such as biomechanical origin of arrhythmia etc.

In human facial skin, several aesthetic units were selected to be imaged using PSOCT to show their corresponding collagen organizations. These regions include the thinnest facial skin (eyelid) to the thickest facial skin (glabella) and demonstrate applicability of PSOCT throughout facial skin. These areas are commonly affected by skin cancer, which often requires surgical resection and reconstruction with tissue flaps. Minimizing wound tension and orienting incisions along skin tension lines is clinically critical in optimal scar healing reconstruction of facial defects.

Numerous methods describing skin tension lines exist. One of the earliest methods is Langer's Lines, based on the natural elliptical tendency of circular wounds created in a cadaver [74]. The most commonly employed method in modern surgery are the Relaxed Skin Tension Lines, determined by pinching skin and observing furrows in the living body [75]. No available method has been formulated with objective knowledge of the collagen fiber organizations. The method proposed in this study enables fast, in-vivo, non-invasive, wide field and depth-resolved collagen orientation imaging, providing an additional metric to give insight into collagen organizations which make up RSTLs in each individual living subject.

4.4.4 Limitations

While we have demonstrated that the DDG-based PST method can be used to extract depth-resolved collagen organization using the single input PSOCT system, further improvement is required. We neglected the dichroism (i.e., the anisotropic scattering attenuation of incident light) [86] of the sample in our current treatment. As the attenuation is one of important parameters in some ophthalmologic studies to characterize the features of the diseases [104], further improvement is required if the diattenuation property of the sample is of concern. Previous studies have shown that the attenuation of the sample can twist the circular curve out of its osculating plane, and hence the trajectory of the output polarization states would become a spiral curve rather than a circular curve at the Poincare sphere [89]. One potential solution to evaluate the attenuation property of the sample is to calculate the torsion value of the trajectory curve and then obtain the degree of the curve twisting out of the plane of the curvature. The bigger the absolute value of the torsion is, the stronger the attenuation would be. In addition, multiple scattering in turbid tissue is known to limit polarization imaging depth and contrast when it is not being considered in the model formulation. Optical clearing [105, 106], a technique that can reduce scattering in the skin and is biologically compatible with cosmetic procedures, may be employed together with PSOCT imaging in future studies to increase the probing depth and contrast.

Finally, the simplicity of design in PSOCT and the widespread clinical use of traditional OCT imaging suggest that birefringent information may serve as an additional contrast from which clinicians may pull from to make interventional decisions. OCT has been used clinically for visualizing vascular function in various pathological states [107], as well as to detect changes in light-scattering properties of fibers associated with the healing process of burn wounds [108]. More recent studies have also introduced non-contact measurements of elasticity using optical coherence elastography, where biomechanical anisotropy has been shown to generally agree with collagen fiber orientation [109]. Together, a non-contact OCT imaging modality coupled with polarization sensitive measurements has the potential to provide clinicians with multiple contrast mechanisms in a single scan, providing a wealth of diagnostic information in a readily translatable package.

4.5 CONCLUSION

In summary, we expect that the proposed PSOCT technique will enable superior contrast and diagnostic capabilities compared to conventional OCT because of its ability to reveal micro- and macroscopic structural features. Potential clinical applications of PSOCT described here include early detection of acute myocardial infarction, evaluation of scar formation and the imaging-guided plastic surgery. In addition, the significant simplification of the PSOCT imaging system facilitates the clinical translation of the PSOCT imaging technique, which may provide a new matrix of diagnostic information.

Chapter 5. CHARACTERIZATION OF NATURAL WHITE SPOT LESIONS IN THE ENAMEL USING MULTIPARAMETRIC POLARIZATION SENSITIVE OPTICAL COHERENCE TOMOGRAPHY

5.1 BACKGROUND AND MOTIVATION

White spot lesions (WSLs) in enamel, the clinically detectable areas of demineralization, are the topic of considerable interest because they indicate the initiation of the caries process [110]. Since the initial state of the caires is a dynamic process that can be effectively prevented and reversed by treatments [111], characterizing and understanding the properties of the WSLs would provide a more critical basis to assess the repair potential for caries.

WSLs have been investigated by confocal laser scanning microscopy, polarization microscopy [112] and scanning electron microscopy (SEM) [113, 114]. Although high-resolution images of the WSLs in the enamel can be provided by these approaches, destructive procedures are required to section the sample and hence limit their application in three-dimensional (3D) real-time study. Non-invasive imaging techniques including radiography [115, 116], quantitative light-induced fluorescence [117, 118], DIAGNOdent [119] and near-infrared light transillumination (NILT) [120, 121] have been utilized to image and assess WSLs without destructing the sample but the images are with a relatively low spatial resolution, which limits the diagnostic accuracy.

Optical coherence tomography (OCT) [15], a non-invasive optical imaging modality that utilizing broadband light sources to obtain 3D high-resolution images, is a gap-filling imaging technique for the detection and imaging of the WSLs in enamel [122, 123]. Taking the advantage of the non-invasive, high-resolution imaging modality, several studies have demonstrated the utility of the OCT to provide effective, accurate and reproducible diagnoses for the WSLs [122]. Moreover, based on the intensity signals provided by the OCT, an intensity correction algorithm that compute the optical attenuation coefficient (OAC) of the dental hard tissues is used to detect the WSLs, providing higher contrast and sensitivity.

Additional to the structural imaging based on backscattering intensities, polarization sensitive optical coherence tomography (PSOCT) [20, 67, 83, 124], a functional extension of OCT that providing birefringent contrast of the sample has been applied to characterize the WSLs in enamel [50] because it was shown that demineralization of enamel is accompanied by distinct changes of polarization properties [4, 125]. Degree of polarization uniformity (DOPU), phase retardation and axis orientation are the main PSOCT parameters that describe the birefringent property of the sample [38]. DOPU, representing depolarization, has been proved as one of the promising parameters to contrast the early carious lesions [50].

Although cumulative phase retardation and axis orientation have been utilized to image the oral hard tissues [50], their potential ability to provide the unambiguous contrast for WSLs still has not been demonstrated in the previous study. There are three main reasons: 1) Accumulated rather than local phase retardation and axis orientation are used in the previous studies to investigate the WSLs. The accumulated polarization results leading to a difficulty to interpret the birefringent property of the sample at depth, while the WSLs usually occur at the subsurface of the enamel [126]; 2) It has been proved that the WSLs in the enamel can cause the depolarization of the probing light, that is, they can randomize the state of polarization. This makes it difficult to determine the phase retardation and axis orientation of the demineralization area, because these two parameters must be computed based on the pure output polarization states; 3) In the PSOCT axis orientation measurement only the orientation orthogonal to the propagation direction of the probing light can be detected because the vertical direction (i.e., the propagation direction of the probing light) can be canceled out due to the round-trip PSOCT measurement. However, the anisotropic direction of the enamel, determined by the alignment of the enamel rods, is commonly accepted as perpendicularly oriented to the tooth surface, which is almost parallel to the direction of the probing light beam [127]. This means that the dominant orientation of the enamel is largely canceled out and cannot be detected. Hence, it’s meaningless to focus on the absolute value of the axis orientation of the enamel.

In this study, phase retardation and axis orientation are utilized to characterize the both the artificially and naturally produced WSLs in enamels by addressing the above issues. First of all, a spatial average method is applied to the normalized polarization state image to suppress the unpolarized component, which can lead to difficulty to compute the phase retardation and axis orientation. Secondly, based on the averaged polarization state image, local phase retardation and local axis orientation are retrieved from the cumulative results using the polarization state tracing method [128]. Finally, the local axis orientation is utilized to differentiate the positive and negative birefringence within the enamel. We focused on the area whose axis orientation is almost 90 degree to the other region. The sudden change of the axis orientation of the enamel is not caused by the change of the alignment of the enamel rods but caused by the change of the mineral volume, which can lead to the inversion of the sign of the birefringence. The inversion of the sign of the birefringence is one of the important indicators of the WSLs [129-131]. Cross-validating by the structural, attenuation and DOPU images, comprehensive characterization of the optical properties of the WSLs in both artificial and true enamels has been achieved. We used a wide-field scanning lens (LSM03, Thorlabs) with approximate spot size/lateral resolution of 25 μm.

5.2 MATERIAL AND METHODS

5.2.1 Multiparametric PSOCT system setup

The multiparametric PSOCT system used in this study has been described in the Chapter 4. The system used a 100-kHz MEMS-VCSEL swept laser source (SL1310V1-10048, Thorlabs), providing an output power of 25 mW with a central wavelength of 1310 nm and a spectral tuning range of 100 nm. The output of the light source was sent to a polarization controller and became linearly polarized through a polarization beam splitter (PBS 1), and then split into the reference and sample arms through a beam splitter at a split-ratio of 50:50. The reference arm was installed with a quarter-wave plate (QWP) with its axis aligned at 22.5° with reference to the input polarization state, ensuring that the reflected light was coupled equally into the vertical and horizontal channels. The sample arm was equipped with a QWP aligned at 45° with respect to the input polarization state, resulting in a circularly polarized light incident at the sample surface. The light coming back from both the reference and sample arms were recombined and sent to PBS1 and PBS2, respectively, where the interference light was split into horizontal (Channel 1: PD1) and vertical (Channel 2: PD2) components. Balanced detection was used for both vertical and horizontal channels to collect the interference signals, upon which PSOCT images are reconstructed. The PSOCT system was controlled using a home-developed LabView (National Instruments) platform which provided flexibility to control the scanning patterns based on the application. The axial resolution was approximately 7.5 μm, in air.

5.2.2 *Signal processing and Image representation*

Multiple images reconstructed by different parameters can be provided simultaneously by the above imaging system. These images can be divided into two groups: one group is computed based on the intensity signals, including the structural images and the OAC images. This group is utilized to guide and cross-validate the polarization results. The other group is the polarization-related results: DOPU, local phase retardation and local axis orientation images. The results from this group are for the further investigation of the birefringent property of the WSLs in enamel. The details of the reconstruction of each image are discussed below.

To obtain the structural image, the inverse Fourier transform is applied to the interference signals obtained from both horizontal and vertical channels and results in complex, depth-resolved A-scans with Amplitudes: $A_{x,y}(z)$ and phases $\phi_{x,y}(z)$. Hence, the structural image $I(z)$ can be obtained by:

$$I(z) \propto A_x(z)^2 + A_y(z)^2, \tag{5.1}$$

The OAC image, calculated based on the OCT structural signals $I(z)$, can obtained by the depth-resolved method, which utilized the single-scattering model [132]:

$$\mu(z) \approx \frac{I(z)}{2\Delta \sum_{z+1}^{N} I(z)}, \tag{5.2}$$

where $\mu(z)$ represents the OAC at zth pixel along the depth, Δ is the pixel size, approximately 7.5 µm in this study, and N is the last pixel of each A-line. Here, it is assumed that most of the light had already been completely attenuated at the Nth pixel.

All the polarization related results in this study are computed based on the Stokes parameters, which can be obtained by:

$$S = \begin{pmatrix} I \\ Q \\ U \\ V \end{pmatrix} = \begin{pmatrix} A_H(z)^2 + A_V(z)^2 \\ A_H(z)^2 - A_V(z)^2 \\ 2A_H(z)A_V(z)\cos\left(\phi_H(z) - \phi_V(z)\right) \\ 2A_H(z)A_V(z)\sin\left(\phi_H(z) - \phi_V(z)\right) \end{pmatrix}, \tag{5.3}$$

Then the degree of polarization uniformity DOPU can be derived as [50]:

$$DOPU = \sqrt{Q_m^2 + U_m^2 + V_m^2}, \tag{5.4}$$

where the indices m indicates the averaged Stokes vector elements over the adjacent pixels. We used 6X6 spatial averaged filter in this study.

To obtain the phase retardation and axis orientation results, all the calculations are based on the averaged Stokes parameters because the average operation of the Stokes parameters can suppress the noise induced by the unpolarized light, which can largely affect the computation of the local polarization parameters. In the Poincare sphere's representation, the averaged Stokes parameters are normalized to the Poincare sphere's surface for the derivation of the local phase retardation and local axis orientation. The trajectory of the Stokes vectors in an A-scan at the Poincare sphere is considered as a spatial curve. Discrete differential geometry (DDG) is applied to this curve to provide the TNB vectors. Based on the TNB vectors of this curve, the local phase retardation δ_n and local axis orientation $\overrightarrow{A_n}$ can be obtained by [128]:

$$\delta_n = \frac{1}{2} arccos \frac{\overrightarrow{N_{n-1}} \cdot \overrightarrow{N_n}}{|\overrightarrow{N_{n-1}}||\overrightarrow{N_n}|}. \tag{5.5}$$

$$\overrightarrow{A_n} = \boldsymbol{R}_{\mathbf{n-1}}\left(-\delta_{n-1};\ \overrightarrow{A_{n-1}}\right)\boldsymbol{R}_{\mathbf{n-2}}\left(-\delta_{n-2};\ \overrightarrow{A_{n-2}}\right) \ldots \boldsymbol{R}_{\mathbf{1}}\left(-\delta_1;\ \overrightarrow{A_1}\right)\vec{B}_n, \tag{5.6}$$

where T_n, B_n are the tangent and binormal vector of the spatial curve, $\boldsymbol{R}_{\mathbf{n}}(-\delta_n;\ \overrightarrow{A_n})$ is the 3D rotation matrix determined by $\overrightarrow{A_n}$ and $-\delta_n$.

5.2.3 Tooth sample preparation

In order to confirm the practicality of PSOCT in dental application, we selected an ex-vivo tooth sample with ICDAS score of 2. The tooth was dis-infected with 0.5% sodium hypochlorite and stored prior to the selection. We then identified the white-spot lesion on the tooth and mark the location for PSOCT scan (Fig 4.). The PSOCT scan was performed with the buccal surface facing the OCT beam. After PSOCT scan, we determined a plane of sectioning that is parallel to the occlusal surface and also includes both white-spot lesion and healthy enamel for the validation of PSOCT. We use a typical dental model trimmer for the sectioning of the tooth. When the sectioning plane touches the white spot lesion, we hand-sanded the tooth with 500-grit and progressively to 1000-grit sand paper to achieve a uniform and smooth surface, ready for PSOCT scan. The second PSOCT scan was performed with the sectioning plane facing the laser beam.

For validation, we exposed the sectioned tooth with a disclosing agent (FP-SCHEIN-193, Henry Schein Inc., p/n: 1024453) for a period of 15 seconds. The WSLs can be stained as green color by the agent while the healthy enamel will not be stained. Then the tooth was cleaned, air-dry observed under the microscope (AMScope, 0.5X objective lens, 30mm WF10X/20 eyepiece). The LED illumination was set to max, and white/black balance was applied. The results of the stained WSL were then used to compare with the second PSOCT results.

5.3 RESULTS

Artificially and naturally produced enamel white spot lesions were scanned using the developed multiparametric PSOCT device. Here, we demonstrate the multi-functional visualization of the enamel with WSLs.

5.3.1 Artificially produced subsurface white spot lesions in bovine enamel

To compare the differences of the optical properties between the sound enamel and the artificially produced WSLs, a bovine enamel block with artificially produced WSLs in the left half was imaged by the multi-parametric PSOCT system. Figures 5.1A-F show the cross-sectional scattering intensity, attenuation, DOPU, polarization state, local phase retardation and local axis orientation images of the bovine enamel block. Compared with the sound enamel, artificially produced WSLs show distinct features in all these parameters. In the intensity image (Fig. 5.1A), the WSLs are visualized as a bright scattering region with a thickness of ~250 μm (as indicated by the white arrows) in the left half. The scattering signals of the WSLs are much stronger than the normal enamel and hence attenuate the signals scattered back from the deeper layers where the dentin (indicating as yellow arrows) is hard to be seen. The attenuation correction result (Fig. 5.1B) further confirmed this observation and provide a high contrast image to differentiate the WSLs from the sound enamel. The multiple scattering of the WSLs also can induce depolarization as shown in Fig. 5.1C, where the DOPU values are lower than 1 (mean DOPU: ~0.72) in the left half of the bovine enamel. However, unlike the scattering and attenuation images, it is difficult to differentiate the subsurface WSLs and the sound enamel below in the DOPU image. These observations have been studied in the previous works [50].

Figure 5.1D shows the spatial averaged polarization state image, in which the output polarization states change sequentially rather than randomly over depth in the WSLs. This is because the depolarization is not severe (DOUP>0.5) in the WSLs in this sample and hence we suspect that these WSLs are in the early stage. In this case, it's possible to compute the local phase retardation (Fig. 5.1E) and the local axis orientation (Fig. 5.1F) based on the spatial averaged output polarization state image (Fig. 5.1D). An increase in the local phase retardation (white arrows in Fig. 5.1E) and a 90° alternation in axis orientation is observed in the subsurface of the left part of the enamel block. Compared with the DOPU, the local phase retardation and local axis orientation can differentiate the sound enamel below the WSLs by removing the accumulation effect of the polarization and providing the local values.

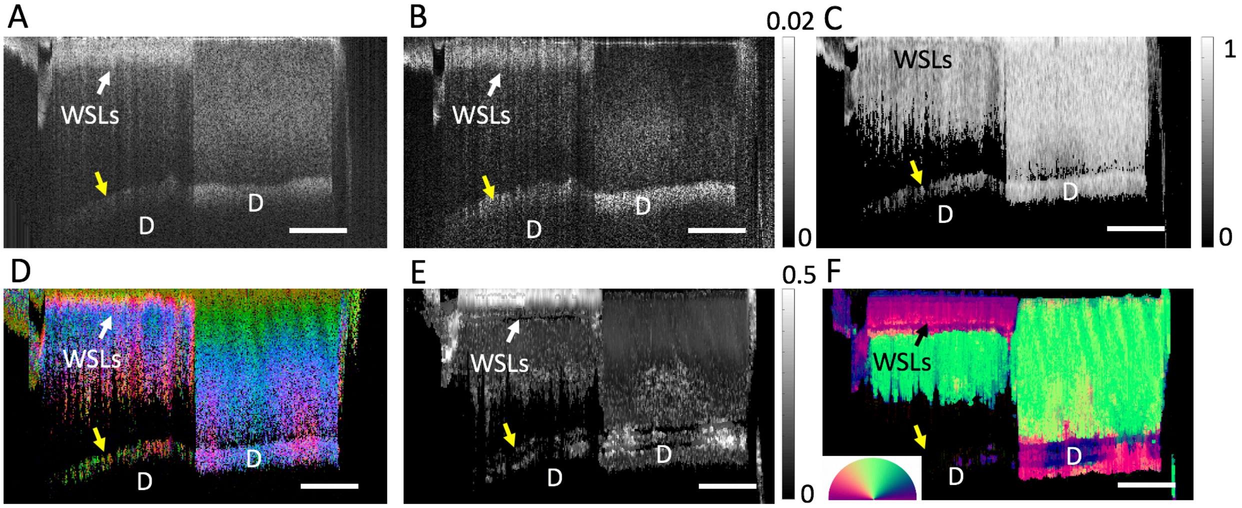

Figure 5.1 Multi-parametric cross-sectional images of the bovine enamel block with artificially produced WSLs in the right half: A) intensity, B) attenuation, C) DOPU, D) polarization state, E) local phase retardation, F) local axis orientation images. WSLs: white spot lesions; D: dentin. The scale bar = 1 mm.

To interpret the 90° alternation in axis orientation of the WSLs, we visualized the trajectories of the output polarization states in A-scans (i.e., the pixels along the depth direction as indicated by the black dash lines in Fig. 5.2B) of the sound enamel (black points) and the WSLs (blue points) respectively at the Poincare sphere in Fig. 5.2A.

For the light scattered back from the sound enamel, the output polarization states rotated clockwise (as indicated by the blue arrow) about a constant axis and formed a circular curve as the depth increase (as indicated by the blue dots). Since the rotation axis (defined by the right-hand rule) of the output polarization states represents the optic axis of the sample [65], the relatively uniform orientation of the rotation axis in the A-scan reveals the homogamous alignment of the enamel rods along with the depth. The local phase retardation which is represented as the rotation angle is relatively small between the adjacent output polarization states, indicating that the phase retardation of the sound enamel is relatively low.

The output polarization states scattered back from the WSLs (indicated by the black dots) rotated about the same axis but in an opposite direction as shown in the black arrow, making the orientation of the WSLs appear 90° relative to the sound enamel. The rotation angle in this A-line is also larger than that in the enamel, indicating that the WSLs have a larger local phase retardation than the enamel. As the depth increase, the output polarization states backtracked (indicated by the red dots) and rotated clockwise about the axis again (indicated by the red arrow) by a smaller rotation angle, revealing that the hard tissues below the WSLs are sound enamel. There are two factors can cause this alteration in axis orientation: 1) the alignment of the sample rotates physically 90° in the cartesian coordinate system; 2) The refractive index in the sample change and reverse the birefringent sign. In this case, the fast and slow axis of the sample switch and cause the 90 ° alteration. According to the previous studies that using polarization microscopy to investigate the WSLs [129-131], the reversion of the birefringent sign (i.e., the second factor), is response for the 90° alteration of the axis orientation in the WSLs.

Since the reversion of the birefringent sign can induce a sharp change of the axis orientation value, the local axis orientation can give an obvious contrast for the WSLs with high sensitivity. Figures 5.2C and 5.2D show the en-face axis orientation images selected at two certain depths (150 μm and 400 μm respectively below the surface) of the whole enamel block. At the subsurface layer of the enamel block (Fig. 5.2C), the WSLs and the sound enamel can be clearly differentiated by different colors. At the deeper layer of the enamel block, uniform colors were found on both sides of the enamel block, indicating that the local axis orientation can contrast the sound enamel below the WSLs while the DOPU image failed to do so. Since the WSLs in the bovine enamel are artificially produced with the same procedures, they present as a very typical and similar condition, which makes it easy to be recognized by each parameter provided by the PSOCT system.

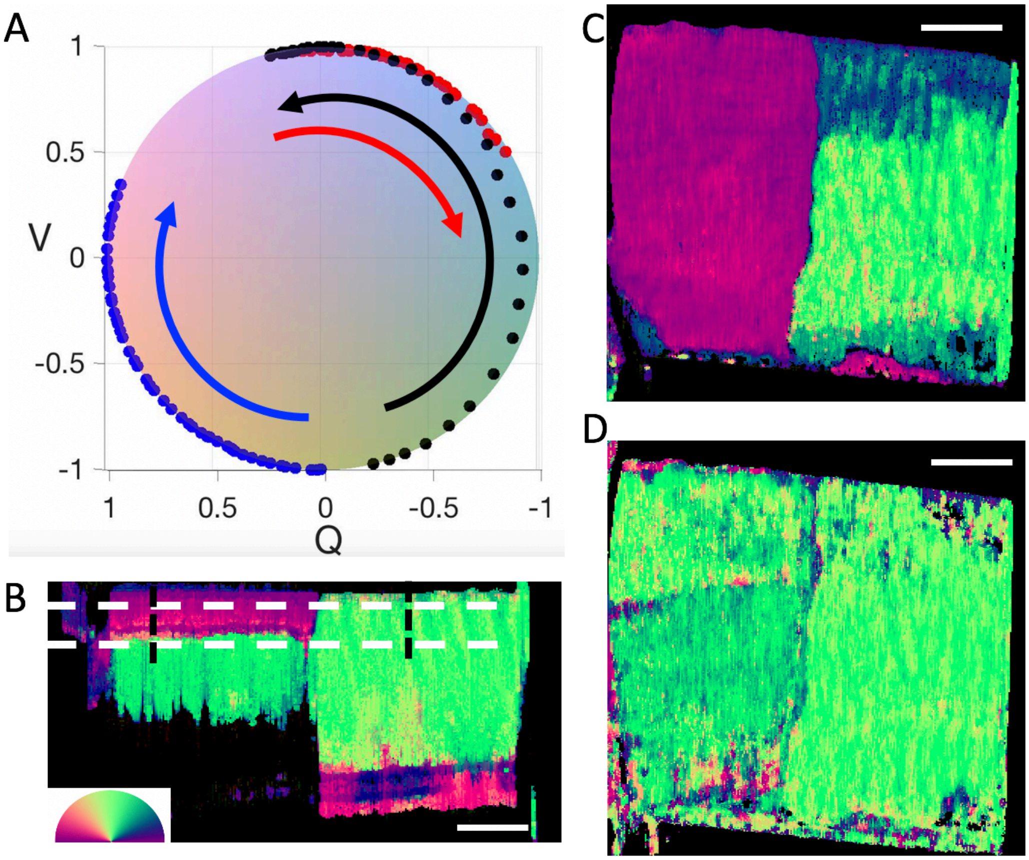

Figure 5.2 Local axis orientation results of the bovine enamel with artificially produced WSLs. A) The trajectories of the output polarization states in two A-scans indicated by black dash lines in B), scattering back from the sound enamel (blue and red dots) and the WSLs (black dots) respectively. C) and D) The en-face local axis orientation images of the bovine enamel at depth of 150 µm and 400 µm below the surface respectively. The scale bar = 1 mm.

5.3.2 Naturally produced WSLs in human enamel

The in vitro human enamel with naturally produced WSLs, which have a more complicated condition than the artificially produced WSLs, are also studied using the multi-parametric PSOCT system. Figure 5.3A-F show the cross-sectional scattering intensity, attenuation, DOPU, polarization state, local phase retardation and local axis orientation images of the human enamel. Three obvious lesion spots (as indicated by the white boxes) are identified in all figures. Compared with the sound enamel (indicated by the yellow arrows), these WSLs appear as strong intensity signals, high attenuation, high depolarization (low DOPU values), higher phase retardation and almost 90° (purple) relative to the orientation of the sound enamel (green). While the intensity (Fig. 5.3A), attenuation (Fig. 5.3B) and local axis orientation images (Fig. 5.3F) provide the location information of the WSLs, the DOPU (Fig. 5.3C) and local phase retardation (Fig. 5.3E) images can help to contrast the severity of the WSLs. In comparison to the lesions in region 1 and region 3 (mean DOPU=0.56 and 0.61 respectively), the lesions in region 2 show a higher degree of depolarization (i.e., the lower DOPU value ~0.34) and higher local phase retardation, indicating that the severity of the lesions in region 2 is higher than that of the lesions in region 1 and 3.

In the subsurface layer above region 3 indicated by the red arrow, increase scattering and slight depolarization are observed, indicating that early-stage lesions may exist in this region. However, the relatively low contrast makes it difficult to differentiate this part of the WSLs from the sound enamel. The contrast of these suspected WSLs is also faintly perceptible in corresponding phase retardation and attenuation images. In Fig. 5.3F, compared with the orientation in sound enamel, an obvious alteration of the local axis (i.e., green to purple) is observed in the subsurface of the enamel above region 3. The change in the orientation is almost 90°, indicating that the sign of the birefringence reversed in this region. These WSLs which are suspected at the early stage and appear as low contrast in the attenuation, DOPU and local phase retardation can be differentiated from the sound enamel by clear boundaries and high contrast in the local axis orientation image.

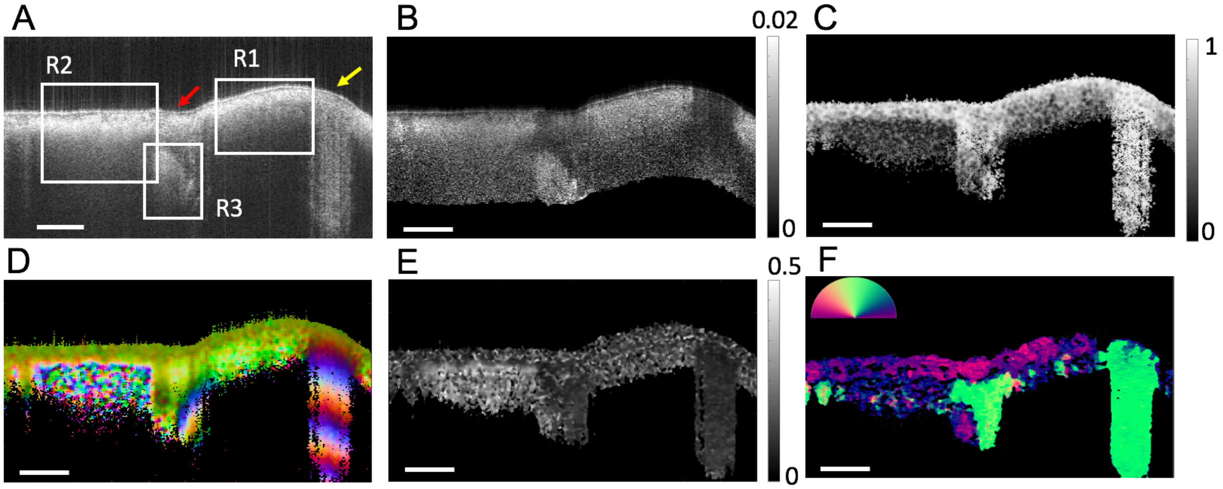

Figure 5.3 Multi-parametric cross-sectional images of the in vitro human enamel with naturally produced WSLs: A) intensity, B) attenuation, C) DOPU, D) polarization state, E) local phase retardation, F) local axis orientation images. The areas of the WSLs spots are indicated by the white boxes in A). Yellow arrow indicates the sound enamel. Red arrow indicates the suspected WSLs that may in the early stage. The scale bar = 500 μm.

To further demonstrate that different parameters of the multi-functional PSOCT can characterize the WSLs from different perspectives, the enface attenuation, DOPU, local phase retardation and local axis orientation images of the human enamel selected at a certain depth (210 μm below the surface of the enamel) are presented in Fig. 5.4. The contours of the lesions can be visualized as bright/purple signals in intensity (Fig. 5.4A), attenuation (Fig. 5.4B) and local axis orientation (Fig. 5.4E) images with relatively high consistency. However, the local axis orientation image shows extra areas of the WSLs (indicating by the arrows), indicating that the local axis orientation may provide higher sensitivity for the detection of the early-stage WSLs. This observation will be discussed in the discussion section below. Different from the previous three parameters that can locate the WSLs, the DOPU (Fig. 5.4C) and local phase retardation (Fig. 5.4D) images provide the information of the severity of the lesions. While the lesions in regions 1 and 2 (indicated by the white boxes) show similar values in the structural and local axis orientation image, they can be differentiated clearly in both the local phase retardation and DOPU images, indicating that the degree of the lesions in region 2 is higher than that in region 1.

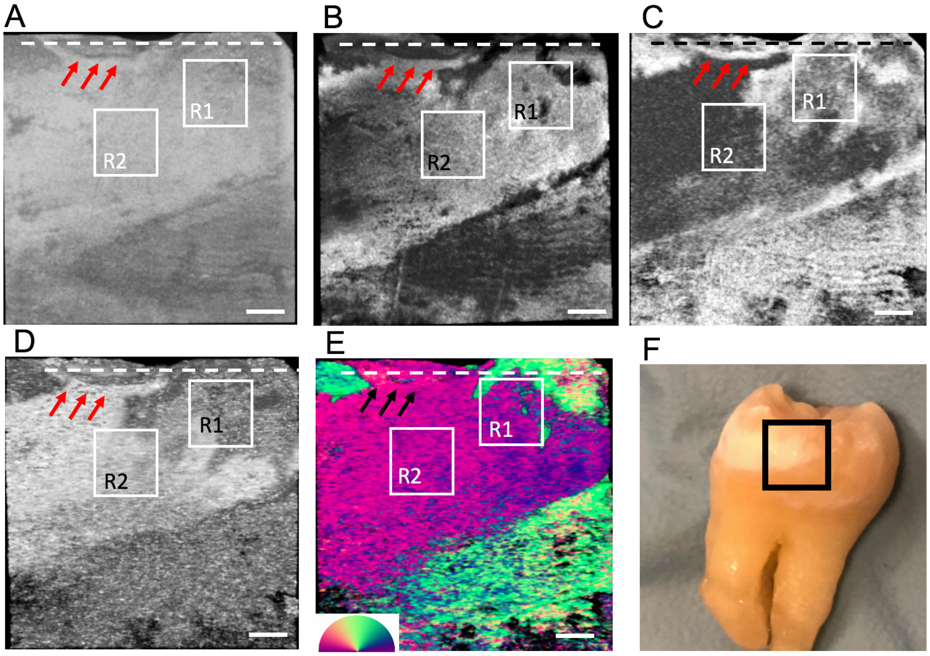

Figure 5.4 Multi-parametric en-face images of an extracted human enamel with naturally produced WSLs at depth of 210 μm below the surface: A) intensity, B) attenuation, C) DOPU, D) local phase retardation, E) local axis orientation images. F) Photograph of the extracted human tooth. The black box indicates the PSOCT imaging region. Arrows indicates the suspected WSLs that may in the early stage. The scale bar = 500 μm.

5.3.3 Validation of the PSOCT results using staining agent

To validate the PSOCT results, the human tooth is sectioned and stained by a disclosing agent, which can visualize the WSLs as green color. Figure 5.5 show the photograph of the stained sectioned enamel, the en-face intensity and local axis orientation images respectively. In the photograph of the stained sectioned enamel, the contour of the WSLs is visualized as the green color. The WSLs appear in the superficial layer of the enamel while the enamel in the deeper layer of the enamel is healthy and presented as its original color. In the intensity image (Fig. 5.5B), the WSLs appear as higher intensity signals which are consistent with the stained region in Fig. 5.5A, demonstrating that WSLs can introduce multiple scattering. In the local axis orientation image (Fig. 5.5C), there is an obvious difference between the healthy enamel and the WSLs. The local axis orientation of the healthy enamel reveals the direction of the enamel rods, which is almost orthogonal to the surface of the enamel. This observation is consistent with previous histological studies. However, the orientation value of the WSLs is almost orthogonal to the deeper healthy enamel right below the WSLs, indicating the sign of the birefringence has been reversed. The contour of the WSLs in Fig. 5.5C is consistent with the stained results, demonstrating that local axis orientation can be used to visualize the WSLs.

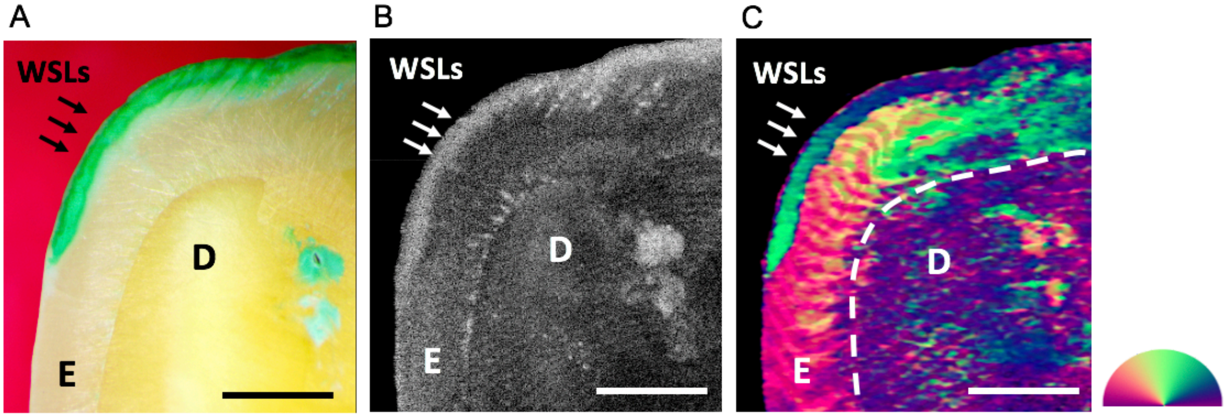

Figure 5.5 Validation of the PSOCT results. A) Photograph of the stained sectioned enamel. En-face B) intensity and C) local axis orientation images of the sectioned enamel at the surface layer. E: enamel; D: Dentin. The scale bar = 1 mm.

5.4 DISCUSSION

Due to the porous nature of the enamel, the total birefringence of the enamel can be considered as a sum of two parts: 1) the negative intrinsic birefringence of the mineral material; 2) the positive birefringence of the space between enamel crystals that is filled by non-mineral medium [133-135]. During the demineralization process, the space between the enamel crystals becomes larger [135]. When the size of the space (i.e., the pore volume) increases to a threshold, the positive birefringence dominates and reverses the sign of the total birefringence of the enamel from negative to positive. Hence, a polarization-related technique that can differentiate the sign of the birefringence enables the detection for the enamel with high pore volume, which is highly related to the demineralization.

In this study, a sharp alteration (~90°) of the orientation has been detected in the WSLs, demonstrating that the local axis orientation mapping has the ability to contrast the WSLs. Here we want to discuss the potential ability of the local axis orientation to contrast the early-stage WSLs with higher sensitivity. As shown in the en-face images in Fig. 5.4, the local axis orientation image shows extra areas of the WSLs compared with the other images. Cross-sectional images in this area (as indicated by the dashed line in Fig. 5.4) were selected to present in Fig. 5.6. The scattering signals (Fig. 5.6A), attenuation (Fig. 5.6B), DOPU (Fig. 5.6C) and local phase retardation (Fig. 5.6E) of the subsurface layer (depth <225 μm below the surface indicated by the red arrows) in the white boxes are very similar with the signals in the sound enamel (indicated by the white arrows). However, in the polarization state image (Fig. 5.6D), the color change trend in the region indicated by the red arrows over depth (i.e., yellow, orange, purple, green) and that in the sound enamel (i.e., yellow, green, purple, orange) are just reverse, revealing the different birefringent properties between these two regions. This difference is revealed in the local axis orientation image (Fig. 5.6F), in which the subsurface layer in the white boxes shows a 90° orientation relative to the sound enamel (indicated by the white arrows, providing a high contrast. Note that, the region right below this subsurface layer (depth >225 μm) shows significant signals of the WSLs in all the cross-sectional images (Fig. 5.6). Since this subsurface layer is very close to the WSLs below, it’s reasonable to suspect the subsurface layer is the early-stage WSLs, where the pore volumes are larger than the sound enamel but smaller than the severe WSLs. Based on this observation, we think the local axis orientation may provide a potential ability to detect the early-stage WSLs with higher sensitivity while other parameters show only slight changes.

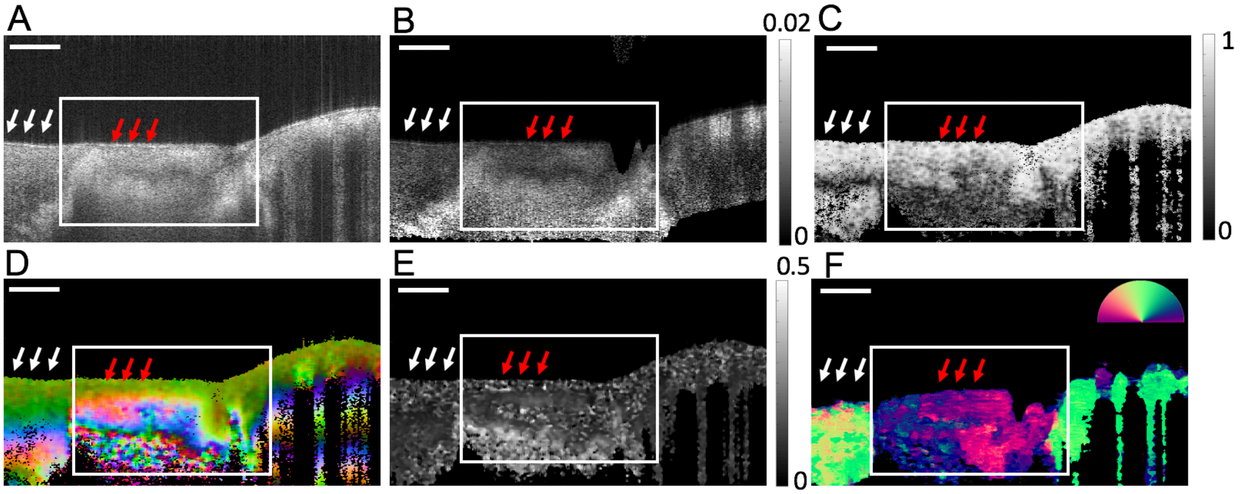

Figure 5.6 Multi-parametric cross-sectional images of the extracted human enamel with naturally produced WSLs: A) intensity, B) attenuation, C) DOPU, D) polarization state, E) local phase retardation, F) local axis orientation images. The area of the WSLs is indicated by the white boxes in A). White arrows indicate the sound enamel. Red arrows indicate the suspected WSLs that may in the early stage. The scale bar = 500 μm.

While we have demonstrated the usefulness of the multiparametric PSOCT for the comprehensive characterization of the WSLs in the enamel, further improvement is required to develop a matric that intergrades all the features of the WSLs. Because each parameter has its own drawback when imaging the WSLs in enamel, the integrated results can help to improve the accuracy of the detection. For example, the contrast of the scattering image is relatively low compared with other parameters. The DOPU is not suitable for the detection of the early-stage WSLs, in which the depolarization is not severe. Except for the WSLs, the local axis orientation can also be affected by the intrinsic difference of the alignment of the enamel rod at different sites of the enamel (e.g., the edge and the center of the enamel). Hence, a multidimensional space can be utilized to screen and score the WSLs.

5.5 CONCLUSION

In conclusion, we have demonstrated the usefulness of the multiparametric PSOCT for the comprehensive characterization of the WSLs in the enamel. The imaging of the artificially produced WSLs in bovine enamel block and the naturally produced WSLs in human enamel suggest that this method enables the differentiation of the WSLs from the sound enamel. Moreover, comprehensive information such as the location, depth, severity of the WSLs can be provided simultaneously based on the multiparameter images. The local axis orientation and local phase retardation images are first provided to characterize the WSLs from a unique angle. We believe that the proposed multiparametric PSOCT imaging would have useful and practical applications in the investigations of WSLs in the enamel both pre-clinically and clinically.

Chapter 6. SUMMARY AND FUTURE WORK

In this dissertation, the development and applications of PSOCT with a single input polarization state are comprehensively presented. From the system setup to algorithms, from mapping the morphology of the birefringent biological tissues to the detection of the changes in the PSOCT parameters related to pathologic activities, the techniques proposed in this research provide a unique perspective in the clinical study of biological tissue functions and disease mechanisms.

In chapter 2, we first visualize the polarization state by using the Stokes parameter-based color encoding method and utilized the polarization state as the imaging parameter to contrast the birefringent components of the sample. Because the change in polarization state includes the comprehensive information (i.e., the phase retardation and axis orientation) of the sample, this parameter can provide the birefringent images with higher contrast and sensitivity.

In chapters 3 and 4, we propose a PSOCT-based polarization state transmission model that leverages the Poincare sphere to describe the evolving polarization state of an incident beam as it travels through a birefringent sample with depth-varying optic axes and phase retardation in a round-trip measurement. Based on this transmission model, we describe two PST methods to derive the local axis orientation and local phase retardation with only one single input polarization state. Without the requirement of multiple input polarization states, this method can simplify the imaging system setup and mitigate motion artifact, being aimed for clinical translation.

In chapter 4, depth-resolved collagen organization imaging is achieved by using the proposed PST method. Local axis orientation mappings of the collagen fibers in the rodent hearts and healthy human facial skin are obtained. Myocardial fiber orientation of the rodent hearts is detected and visualized. Fiber disorganization is detected within an infarcted rodent heart. For the in vivo study, we demonstrate depth-resolved collagen organization imaging in healthy human skin to reveal the facial skin tension lines.

In chapter 5, we have demonstrated the usefulness of the multiparametric PSOCT for the comprehensive characterization of the WSLs in the enamel. The imaging of the artificially produced WSLs in bovine enamel block and the naturally produced WSLs in human enamel suggest that this method enables the differentiation of the WSLs from the sound enamel. Moreover, comprehensive information such as the location, depth, severity of the WSLs can be provided simultaneously based on the multiparameter images. The local axis orientation and local phase retardation images are first provided to characterize the WSLs from a unique angle.

The above new development has significantly enhanced the capability of PSOCT. Several further improvements are worth exploring. First is the development of the single input fiber-based PSOCT system based on the PST method. A single input fiber-based system is more flexible and can facilitate a lot of applications, especially in endoscopic imaging. One of the challenges for the fiber-based PSOCT system is to stabilize the polarization state of the light when the detected signals travels through the optical fibers. Polarization maintaining (PM) fibers are utilized to fabricate the PSOCT system in the previous studies. Although the two polarization modes of the incident light (fast axis and slow axis) can be preserved in the PM fiber during their propagation, the phase delay between them is difficult to control since multiple factors, e.g., fiber length, environmental temperature, and strain variations, can cause unpredictable changes in phase. Any disturbance in the PM fiber can still induce a change in the output polarization state. Hence, there is need to fabricate a fiber-based PSOCT that immune to the environmental disturbance. Secondly, the application of the depth-resolved PSOCT in ophthalmology such as the detection of the trabecular meshwork (TM) warrants further investigation. The TM is a drainage of the aqueous humor of the anterior eye chamber and controls intraocular pressure. If drainage from the TM is blocked, the pressure in the eye, i.e., the intraocular pressure, increases, resulting in angle-closure glaucoma. Hence, the position of the TM can be used as a landmark for screening patients for the risk of angle-closure glaucoma. There is a clinical demand for the differentiation of the trabecular meshwork (TM) from other tissues in the anterior eye.

BIBLIOGRAPHY

[1] L. Zheleznyak, A. Barbot, A. Ghosh, G. Yoon, J. Vis., 16 (2016) 1-1.

[2] K. Kinosita, S. Kawato, A. Ikegami, Adv. Biophys., 17 (1984) 147-203.

[3] I. Ahmad, J. Biomed. Opt. (2017) 100901.

[4] A.C.T. Ko, L.-P.i. Choo-Smith, M. Hewko, M.G. Sowa, C.C.S. Dong, B. Cleghorn, Opt. Express, 14 (2006) 203-215.

[5] X.-C. Yao, A. Foust, D.M. Rector, B. Barrowes, J.S. George, Biophys. J., 88 (2005) 4170-4177.

[6] D.M. Jameson, J.A. Ross, Chem. Rev., 110 (2010) 2685-2708.

[7] M.A. Rizzo, D.W. Piston, Biophys. J., 88 (2005) L14-L16.

[8] C.S. Joseph, R. Patel, V.A. Neel, R.H. Giles, A.N. Yaroslavsky, J. Biophoton., 7 (2014) 295-303.

[9] L. Trifonyuk, A. Sdobnov, W. Baranowski, V. Ushenko, O. Olar, A. Dubolazov, L. Pidkamin, M. Sidor, O. Vanchuliak, A. Motrich, M. Gorsky, I. Meglinski, Lasers Med Sci., 35 (2020) 877-891.

[10] M.-R. Antonelli, A. Pierangelo, T. Novikova, P. Validire, A. Benali, B. Gayet, A. De Martino, Opt. Express, 18 (2010) 10200-10208.

[11] J.L. Oudar, R.W. Smith, Y.R. Shen, Appl. Opt. Lett., 34 (1979) 758-760.

[12] E.Y.S. Yew, C.J.R. Sheppard, Opt. Commun., 275 (2007) 453-457.

[13] R. Kumar, K.M. Grønhaug, E.I. Romijn, A. Finnøy, C.L. Davies, J.O. Drogset, M.B. Lilledahl, J. Biophotonics, 8 (2015) 730-739.

[14] W.T. Tang, E.Y.S. Yew, C.J.R. Sheppard, Opt. Lett., 34 (2009) 2147-2149.

[15] P.H. Tomlins, R.K. Wang, J. Phys. D Appl. Phys., 38 (2005) 2519-2535.

[16] J.F. de Boer, C.K. Hitzenberger, Y. Yasuno, Biomed. Opt. Express, 8 (2017) 1838-1873.

[17] C. Fan, G. Yao, Opt. lett., 37 (2012) 1415-1417.

[18] C. Fan, G.J.J.o.B.O. Yao, J. Biomed. Opt., 17 (2012) 110501.

[19] M. Villiger, E.Z. Zhang, S.K. Nadkarni, W.-Y. Oh, B.J. Vakoc, B.E. Bouma, Opt. Express, 21 (2013) 16353-16369.

[20] S. Makita, M. Yamanari, Y. Yasuno, Opt. Express, 18 (2010) 854-876.

[21] Ahhyun S. Nam, Jeena M. Easow, Isabel Chico-Calero, Martin Villiger, Jonathan Welt, Gregory H. Borschel, Jonathan M. Winograd, Mark A. Randolph, R.W. Redmond, B.J. Vakoc, Scientific Reports, 8 (2018) 14004.

[22] Q. Li, D. Sampson, M. Villiger, Opt. Lett., 45 (2020) 4919-4922.

[23] J.F. de Boer, B. Cense, B.H. Park, M.C. Pierce, G.J. Tearney, B.E. Bouma, Optics Letters, 28 (2003) 2067-2069.

[24] N. Nassif, B. Cense, B. Hyle Park, S.H. Yun, T.C. Chen, B.E. Bouma, G.J. Tearney, J.F. de Boer, Opt. Lett., 29 (2004) 480-482.

[25] W. Drexler, J.G. Fujimoto, Prog. Retinal Eye Res., 27 (2008) 45-88.

[26] R.K. Wang, S. Kirkpatrick, M. Hinds, Appl. Phys. Lett., 90 (2007) 164105.

[27] R.K. Wang, A.L. Nuttall, J. Biomed. Opt., 15 (2010) 056005.

[28] H. Spahr, C. Pfäffle, S. Burhan, L. Kutzner, F. Hilge, G. Hüttmann, D. Hillmann, Sci. Rep., 9 (2019) 11748.

[29] T. Akkin, D. Landowne, A. Sivaprakasam, J. Membr. Biol., 231 (2009) 35-46.

[30] Y.J. Yeh, A.J. Black, D. Landowne, T. Akkin, Neurophotonics, 2 (2015) 035001.

[31] T. Akkin, C. Joo, J.F.D. Boer, Biophys. J., 93 (2007) 1347-1353.

[32] P. Tang, Y. Li, A. Rakymzhan, Z. Xie, R.K. Wang, Biomed. Opt. Express, 11 (2020) 699-710.

[33] U. Morgner, W. Drexler, F.X. Kärtner, X.D. Li, C. Pitris, E.P. Ippen, J.G. Fujimoto, Opt. Lett., 25 (2000) 111-113.

[34] N. Bosschaart, D. Faber, T. van Leeuwen, M. Aalders, J. Biomed. Opt. (2011) 100504.

[35] C.P. Fleming, J. Eckert, E.F. Halpern, J.A. Gardecki, G.J. Tearney, Biomed. Opt. Express, 4 (2013) 1269-1284.

[36] C. Sun, B. Standish, V. Yang, J. Biomed. Opt., 16 (2011) 043001.

[37] M. Kirby, I. Pelivanov, S. Song, L. Ambrozinski, S.J. Yoon, L. Gao, D. Li, T. Shen, R. Wang, M. O'Donnell, J. Biomed. Opt., 22 (2017) 121720.

[38] C.-L. Chen, R.K. Wang, Biomed. Opt. Express, 8 (2017) 1056-1082.

[39] L. An, J. Qin, R.K. Wang, Opt. Express, 18 (2010) 8220-8228.

[40] W.J. Choi, Y. Li, R.K. Wang, IEEE T MED IMAGING, 38 (2019) 1427-1437.

[41] Z. Chen, T.E. Milner, D. Dave, J.S. Nelson, Opt. Lett., 22 (1997) 64-66.

[42] U. Dirnagl, B. Kaplan, M. Jacewicz, W. Pulsinelli, J. Cereb. Blood Flow

Metab., 9 (1989) 589-596.

[43] D. Chen, W. Yuan, H.-C. Park, X. Li, Biomed. Opt. Express, 11 (2020) 4316-4325.

[44] V. Demidov, A. Maeda, M. Sugita, V. Madge, S. Sadanand, C. Flueraru, I.A. Vitkin, Sci. Rep., 8 (2018) 38.

[45] W. Wei, Y. Li, Z. Xie, A. Deegan, K.R. Wang, IEEE Trans. Med. Imaging, 38 (2019) 1295-1303.

[46] J.A. Filosa, V.M. Blanco, Experimental Physiology., 92 (2007) 641-646.

[47] D.K. Kasaragod, Z. Lu, J. Jacobs, S.J. Matcher, Biomed. Opt. Express, 3 (2012) 378-387.

[48] S.K. Nadkarni, M.C. Pierce, B.H. Park, J.F. de Boer, P. Whittaker, B.E. Bouma, J.E. Bressner, E. Halpern, S.L. Houser, G.J. Tearney, J. Am. Coll. Cardiol., 49 (2007) 1474-1481.

[49] P. Gong, L. Chin, S. Es'haghian, Y.M. Liew, F. Wood, D. Sampson, R. McLaughlin, J. Biomed. Opt. (2014) 126014.

[50] J. Golde, F. Tetschke, J. Walther, T. Rosenauer, F. Hempel, C. Hannig, E. Koch, L. Kirsten, J. Biomed. Opt., 23 (2018) 071203.

[51] B. Baumann, S.O. Baumann, T. Konegger, M. Pircher, E. Götzinger, F. Schlanitz, C. Schütze, H. Sattmann, M. Litschauer, U. Schmidt-Erfurth, C.K. Hitzenberger, Biomed. Opt. Express, 3 (2012) 1670-1683.

[52] G. Yao, L.V. Wang, Opt. Lett., 24 (1999) 537-539.

[53] Q. Li, K. Karnowski, P.B. Noble, A. Cairncross, A. James, M. Villiger, D.D. Sampson, Biomed. Opt. Express, 9 (2018) 5437-5455.

[54] J.F. de Boer, T.E. Milner, M.J.C. van Gemert, J.S. Nelson, Opt. Lett., 22 (1997) 934-936.

[55] S. Sakai, M. Yamanari, Y. Lim, N. Nakagawa, Y. Yasuno, Biomed. Opt. Express, 2 (2011) 2623-2631.

[56] C.K. Hitzenberger, E. Götzinger, M. Sticker, M. Pircher, A.F. Fercher, Opt. Express, 9 (2001) 780-790.

[57] C. Fan, G. Yao, Biomed. Opt. Express, 4 (2013) 460-465.

[58] S. Guo, J. Zhang, L. Wang, J.S. Nelson, Z. Chen, Opt. Lett., 29 (2004) 2025-2027.

[59] S.P. Morgan, I.M. Stockford, Opt. Lett., 28 (2003) 114-116.

[60] T.-H. Tsai, X. Yuan, D.J. Brady, Opt. Express, 23 (2015) 11912-11926.

[61] T. York, S.B. Powell, S. Gao, L. Kahan, T. Charanya, D. Saha, N.W. Roberts, T.W. Cronin, J. Marshall, S. Achilefu, S.P. Lake, B. Raman, V. Gruev, Proc. IEEE, 102 (2014) 1450-1469.

[62] P. Whittaker, D.R. Boughner, R.A. Kloner, Am. J. Pathol., 134 (1989) 879-893.

[63] K.S. Park, W.J. Choi, S. Song, J. Xu, R.K. Wang, Lasers Surg Med, 50 (2017) 213-221.

[64] B. Park, M. Pierce, B. Cense, J. Boer, Opt. lett., 30 (2005) 2587-2589.

[65] B.H. Park, M.C. Pierce, B. Cense, J.F. de Boer, Opt. Express, 11 (2003) 782-793.

[66] C. Saxer, J. Boer, B. Park, Y. Zhao, Z. Chen, J. Nelson, Opt. lett., 25 (2000) 1355-1357.

[67] B. Baumann, W. Choi, B. Potsaid, D. Huang, J.S. Duker, J.G. Fujimoto, Opt. Express, 20 (2012) 10229-10241.

[68] J. Walther, Q. Li, M. Villiger, C.S. Farah, E. Koch, K. Karnowski, D.D. Sampson, Biomed. Opt. Express, 10 (2019) 1942-1956.

[69] S. Rivet, M. Marques, A. Bradu, A. Podoleanu, Opt. Express, 25 (2017) 14533.

[70] M.K. Al-Qaisi, T. Akkin, Opt. Express, 16 (2008) 13032-13041.

[71] J.F. de Boer, T.E. Milner, J.S. Nelson, Opt. Lett., 24 (1999) 300-302.

[72] J. Boer, T. Milner, J. Biomed. Opt., 7 (2002) 359-371.

[73] G.D.D. Lullo, S. Sweeney, J. Kr rkko , L. Ala Kokko, J.S.S. Antonio, J. Biol. Chem., 277 (2002) 4223 - 4231.

[74] A.K. Langer, Br. J. Plast. Surg., 31 (1978) 3-8.

[75] A.F. Borges, Plast. Reconstr. Surg., 73 (1984) 144-150.

[76] D.D.J. Streeter, H.M. Spotnitz, D.P. Patel, J.J. Ross, E.E. Sonnenblick, Circ. Res., 24 (1969) 339-347.

[77] W.J. Karlon, J.W. Covell, A.D. McCulloch, J.J. Hunter, J.H. Omens, Anat. Rec., 252 (1998) 612-625.

[78] B. Yang, B. Brazile, N.-J. Jan, Y. Hua, J. Wei, I. Sigal, J. of Biomedical Optics (2018) 106001.

[79] N.-J. Jan, K. Lathrop, I.A. Sigal, Invest. Ophthalmol. Visual Sci., 58 (2017) 735-744.

[80] P.C. Stoller, B.M. Kim, A.M. Rubenchik, K.M. Reiser, D.S. L.B., J. Biomed. Opt., 7 (2002) 205-214.

[81] T. Yasui, Y. Tohno, T. Araki, J. Biol. Chem., 9 (2004) 259-264.

[82] T. Yasui, Y. Takahashi, S. Fukushima, Y. Ogura, T. Yamashita, T. Kuwahara, T. Hirao, T. Araki, Opt. Express, 17 (2009) 912-923.

[83] P. Tang, J. Xu, R.K. Wang, Appl. Phys. Lett., 113 (2018) 231101.

[84] E. Li, S. Makita, Y.-J. Hong, D. Kasaragod, Y. Yasuno, Biomed. Opt. Express, 8 (2017) 1290-1305.

[85] V.V. Tuchin, L.V. Wang, D.A. Zimnyakov, Optical polarization in biomedical applications, Springer-Verlag, Berlin, Heidelberg, N.Y., 2006.

[86] V.V. Tuchin, J. Biomed. Opt., 21 (2016) 071114-071111-071137.

[87] S. Hu, M. Lundgren, A.J. Niemi, Phys. Rev. E 83 (2011) 061908.

[88] A. Nam, Department of Mechanical Engineering, Massachusetts Institute of Technology2017.

[89] J. Park, N.J. Kemp, H.N. Zaatari, H.G. Rylander Iii, T.E. Milner, J. Opt. Soc. Am., 23 (2006) 679-690.

[90] N.J. Kemp, J. Park, H.N. Zaatari, H.G. Rylander, T.E. Milner, J. Opt. Soc. Am. A, 22 (2005) 552-560.

[91] N. Ortega-Quijano, T. Marvdashti, A.K. Ellerbee Bowden, Opt. Lett., 41 (2016) 2350-2353.

[92] G. Piérard, Lapière, C. , Am. J. Dermatopathol., 9 (1987) 219-224.

[93] A.F. Borges, Dermatologic Clinics, 7 (1989) 169-178.

[94] A. Alhamdi, Iraqi J. M. S., 13 (2015) 103-107.

[95] B.d.C. Vidal, M.L.S. Mello, Acta Histochem., 112 (2010) 53-61.

[96] M. Zaffar, A. Pradhan, Appl. Opt., 59 (2020) 1237-1248.

[97] S.K. de Visser, J.C. Bowden, E. Wentrup-Byrne, L. Rintoul, T. Bostrom, J.M. Pope, K.I. Momot, Osteoarthr. Cartil., 16 (2008) 689-697.

[98] R. Ariga, E. Tunnicliffe, S. Manohar, M. Mahmod, B. Raman, S. Piechnik, J. Francis, M. Robson, S. Neubauer, H. Watkins, J. Am. Coll. Cardiol., 73 (2019) 2494-2502.

[99] Y. Wang, K. Zhang, N.B. Wasala, X. Yao, D. Duan, G. Yao, Biomed. Opt. Express, 5 (2014) 2843-2855.

[100] J.R. Mao, J. Bristow, J Clin Invest., 107 (2001) 1063-1069.

[101] T. Krieg, J.S. Perlish, R. Fleischmajer, O. Braun-Falco, Arch. Dermatol. Res., 277 (1985) 373-376.

[102] W.Y. Oh, S.H. Yun, B.J. Vakoc, M. Shishkov, A.E. Desjardins, B.H. Park, J.F. de Boer, G.J. Tearney, B.E. Bouma, Opt. Express, 16 (2008) 1096-1103.

[103] K.L. Lurie, T.J. Moritz, A.K. Ellerbee, Biomed. Opt. Express, 3 (2012) 2273-2287.

[104] V. Louis-Dorr, K. Naoun, P. Allé, A.-M. Benoit, A. Raspiller, Appl. Opt., 43 (2004) 1515-1521.

[105] D. Chen, N. Zeng, Y. Wang, H. He, V. Tuchin, H. Ma, J. Biomed. Opt. (2016) 081209.

[106] D. Chen, N. Zeng, Q. Xie, H. He, V.V. Tuchin, H. Ma, Biomed. Opt. Express, 8 (2017) 3559-3570.

[107] A.J. Deegan, F. Talebi-Liasi, S. Song, Y. Li, J. Xu, S. Men, M.M. Shinohara, M.E. Flowers, S.J. Lee, R.K. Wang, Lasers Surg. Med., 50 (2018) 183-193.

[108] J. Lu, A.J. Deegan, Y. Cheng, T. Liu, Y. Zheng, S.P. Mandell, R.K. Wang, Lasers Surg. Med., n/a (2021).

[109] J.J. Pitre, M.A. Kirby, D.S. Li, T.T. Shen, R.K. Wang, M. O'Donnell, I. Pelivanov, Sci. Rep., 10 (2020) 12983.

[110] S. Pathak, K. Roopa, P. Parameswarappa, N. E, J. Pediatr. Dent., 3 (2015) 1-7.

[111] J.D.B.J.C.D. Featherstone, Community Dent. Oral Epidemiol., 27 (1999) 31-40.

[112] A. Banerjee, M. Sherriff, E.A.M. Kidd, T.F. Watson, Br. Dent. J., 187 (1999) 206-210.

[113] K. Yoshihara, N. Nagaoka, A. Nakamura, T. Hara, S. Hayakawa, Y. Yoshida, B. Van Meerbeek, Sci. Rep., 10 (2020) 4387.

[114] W. Sukontapatipark, M.A. El-Agroudi, N.J. Selliseth, K. Thunold, K.A. Selvig, Eur J Orthod., 23 (2001) 475-484.

[115] T.T.Y. Huang, A.S. Jones, L.H. He, M.A. Darendeliler, M.V. Swain, J. Dent., 35 (2007) 737-743.

[116] K. Kamburoğlu, H. Kurt, E. Kolsuz, B. Öztaş, I. Tatar, H.H. Çelik, J. Digit. Imaging, 24 (2011) 804-813.

[117] H.E. Kim, B.-I. Kim, Photodiagn. Photodyn. Ther., 12 (2015) 378-384.

[118] M. Ando, G.J. Eckert, G.K. Stookey, D.T. Zero, Caries Res., 38 (2004) 39-44.

[119] D. Sardana, J. Zhang, M. Ekambaram, Y. Yang, C.P. McGrath, C.K.Y. Yiu, J. Dent., 82 (2019) 1-10.

[120] M. Abdelaziz, I. Krejci, D. Fried, J. Dent., 91 (2019) 103222.

[121] M. Melo, A. Pascual, I. Camps, F. Ata-Ali, J. Ata-Ali, Sci. Rep., 9 (2019) 14224.

[122] Y. Shimada, M.F. Burrow, K. Araki, Y. Zhou, K. Hosaka, A. Sadr, M. Yoshiyama, T. Miyazaki, Y. Sumi, J. Tagami, Scientific Reports, 10 (2020) 15754.

[123] A.M.A. Maia, A.Z. de Freitas, S. de L. Campello, A.S.L. Gomes, L. Karlsson, J. Biophoton., 9 (2016) 596-602.

[124] C. Fan, Y. Wang, R.K. Wang, Opt. Express, 15 (2007) 7950-7961.

[125] R.C.G. DE MEDEIROS, J.D. SOARES, F.B. DE SOUSA, J. Microsc., 246 (2012) 177-189.

[126] M. Khoroushi, M. Kachuie, Contemp Clin Dent., 8 (2017) 11-19.

[127] C.P. Fernandes, O. Chevitarese, J. Prosthet. Dent., 65 (1991) 793-800.

[128] P. Tang, R. Wang, Biomed. Opt. Express, 11 (2020) 6852-6863.

[129] H.S.M. Crabb, K.V. Mortimer, Nature, 209 (1966) 611-612.

[130] C.S. de Mattos Brito, K.R.S. Meira, F.B. de Sousa, Microsc. Res. Tech., 81 (2018) 181-190.

[131] K. Bansal, K. Gauba, A. Tewari, A. Sahni, J. Indian. Soc. Pedod. Prev. Dent., 28 (2010) 264-270.

[132] K.A. Vermeer, J. Mo, J.J.A. Weda, H.G. Lemij, J.F. de Boer, Biomed. Opt. Express, 5 (2014) 322-337.

[133] H.M. Theuns, R.P. Shellis, A. Groeneveld, J.W.E. van Dijk, D.F.G. Poole, Caries Res., 27 (1993) 9-14.

[134] Shellis R.P., Hallsworth A.S., Kirkham J., R. C., Eur. J. Oral Sci., 110 (2002) 392-395.

[135] G. Gustafson, Acta Odontol. Scand., 15 (1957) 13-55.